AN ABSTRACT OF THE DISSERTATION OF

Harish Reddy Gadey for the degree of Doctor of Philosophy in Nuclear Engineering presented on March 12, 2021.

Title: Development of a Radioxenon Detection System using Stilbene and Strontium Iodide

Abstract approved:

_____

Abi T. Farsoni

The Comprehensive Nuclear-Test-Ban Treaty (CTBT) prohibits the testing of nuclear weapons on the face of the earth. The detection of atmospheric radioxenon (^{131m}Xe, $^{133m/133}$Xe, and ^{135}Xe) plays an important role in the identification of sub-surface clandestine nuclear weapon explosions. Since the radioxenon identified above decay via two radiation in coincidence, it allows the discrimination of background single events which leads to achieving a very low minimum detectable concentration (MDC) of below 1 mBq/m^3. Some of the significant drawbacks of the systems on the International Monitoring System (IMS) network include memory effect in the electron detection cell, environmentally susceptible electronics, bulky detection systems, poor energy resolution, and high cost.

The Stilbene-SrI_2(Eu) detection system aims to improve some of these shortcomings by incorporating the use of digital pulse processing, small form factor SiPMs compared to PMTs, and better detection elements in terms of energy resolution and memory effect. The Stilbene and SrI_2(Eu) detectors operate in coincidence and these events are

identified in real-time using a Field Programmable Gate Array (FPGA). Geant4 and DETECT2000 optical photon transport simulations were performed to study the distribution of the photons on the SiPMs. The four radioxenons of interest were irradiated in the Oregon State University TRIGA reactor and injected in the gas cell for evaluating the detector performance. The unique signatures from all the four radioxenon were uniquely identified. This detection system also yielded a memory effect of about 0.069 ± 0.015% which is almost a 70 times improvement compared to conventional plastic scintillators. This was followed by performing the background measurements and MDC calculations. A background coincidence count rate of 0.0174 ± 0.0003 counts per second was recorded with a background rejection rate of about 98.89 ± 0.02%. The MDC of ^{131m}Xe, ^{133m}Xe, ^{133}Xe, and ^{135}Xe was determined to be 0.15 ± 0.02, 0.12 ± 0.02, 0.30 ± 0.03, and 0.74 ± 0.08 mBq/m^3 respectively. These values meet the requirements of the CTBTO of achieving an MDC below 1 mBq/m^3 for all radioxenon of interest. The performance of the Stilbene-SrI_2(Eu) detection system also compares well with the state-of-the-art detectors on the IMS network.

Development of a Radioxenon Detection System using Stilbene and Strontium Iodide

by
Harish Reddy Gadey

A DISSERTATION

submitted to

Oregon State University

in partial fulfillment of
the requirements for the
degree of

Doctor of Philosophy

Presented March 12, 2021
Commencement June 2021

Doctor of Philosophy dissertation of Harish Reddy Gadey presented on March 12, 2021

APPROVED:

Major Professor, representing Nuclear Engineering

Head of the School of Nuclear Science and Engineering

Dean of the Graduate School

I understand that my dissertation will become part of the permanent collection of Oregon State University libraries. My signature below authorizes release of my dissertation to any reader upon request.

Harish Reddy Gadey, Author

ACKNOWLEDGEMENTS

I would like to take this opportunity to express my gratitude to my advisor, Dr. Abi. T. Farsoni for giving me this opportunity to learn and grow under his guidance. I believe some of the skills I have gained under you will help me in the long run. I would also like to thank my committee members Dr. Yang, Dr. Palmer, Dr. Krane, and Dr. Sinha for taking time out of their schedule to provide critical feedback and attending my prelims and defense.

Friends, and colleagues have played a critical part during the past few years. Dr. Steven A. Czyz, you have helped me on more occasions than you or I can recollect. I hope some of those deep conversations in detection science have truly helped the both of us. Dr. Lily Ranjbar, the support you have provided me over the past few years has been truly amazing. Dr. Eric M. Becker, you have been instrumental in helping me understand the basics of VHDL, I have learnt a lot from you in the initial 2 years of my grad school. Dr. Abdulsalam M Alhawsawi, the fun conversations we had in the IEEE NSS 2017 will be remembered for a long time. I would also like to thank Mitch Mannino for the talks we have had over the past year and for willing to share the DPP8 with me for my experiments.

I would like to also thank Dr. G.M. Brahmanandhan and Dr. Ganesan Vaidyanathan, my undergraduate professors, for motivating/ encouraging me to pursue graduate school. My high school computer science teacher Mohini Arora deserves a special mention for inculcating the importance of programming from a young age.

At last, but certainly not the least, my parents who have supported me over the past number of years and for enduring with me the ups and downs in life. Rijuta Kapoor, you have been a great support mechanism these past 3 years. Things I have achieved at OSU and beyond would not have been possible with you. Finally, I would like to thank my friends at Corvallis for being there for me these past 5 years.

TABLE OF CONTENTS

Page

TABLE OF CONTENTS (Continued)

Page

TABLE OF CONTENTS (Continued)

Page

TABLE OF CONTENTS (Continued)

Page

TABLE OF CONTENTS (Continued)

Page

TABLE OF CONTENTS (Continued)

Page

LIST OF FIGURES

Figure Page

LIST OF FIGURES (Continued)

Figure Page

LIST OF FIGURES (Continued)

Figure Page

LIST OF FIGURES (Continued)

Figure Page

LIST OF FIGURES (Continued)

Figure Page

LIST OF FIGURES (Continued)

Figure Page

LIST OF FIGURES (Continued)

Figure Page

LIST OF FIGURES (Continued)

Figure Page

LIST OF FIGURES (Continued)

Figure Page

LIST OF FIGURES (Continued)

Figure Page

LIST OF TABLES

DEDICATION

Dedicated to the never-ending passion and desire of scientists and researchers of the past, present, and the future in a quest to explore the unknown.

DEVELOPMENT OF A RADIOXENON DETECTION SYSTEM USING STILBENE AND STRONTIUM IODIDE

1. INTRODUCTION

1.1 Detecting Nuclear Weapon Explosions

The world has witnessed two nuclear weapon explosions in the year 1945 at Hiroshima and Nagasaki. This played a major role in ending the second world war. There have been over two thousand nuclear weapon tests carried out in the world post the second world war. To limit the number of nuclear weapon tests and restrict further development of these weapons of mass destruction, the United Nations General Assembly has adopted the Comprehensive Nuclear-Test-Ban Treaty (CTBT) in 1996 [1]. This treaty prohibits the testing of nuclear weapons by any nation, under any circumstance, anywhere on the earth, including surface, underwater, underground, and atmospheric testing. As of this writing, a total of 184 and 168 nations have signed and ratified this treaty respectively. Although all the necessary nations have not signed this treaty to enter force, the Vienna based Comprehensive Nuclear-Test-Ban Treaty Organization (CTBTO) has been tasked with setting up the verification regime to detect undeclared/ clandestine nuclear weapon explosions. This verification regime consists of a total of 321 International Monitoring Stations (IMS) spread all across the world employing four monitoring technologies: seismic, infrasound, hydroacoustic, and radionuclide signatures [2]. Using signatures from the four above mentioned technologies, it can be determined if the event was nuclear in nature. Eighty of the 321 stations are radionuclide based and additionally, forty of these stations are/ will be retrofitted to carry out noble gas detection. Fig. 1 shows the IMS stations all across the world [3].

The noble gas detectors at the IMS stations are responsible for detecting four radioxenon isotopes: ^{131m}Xe, ^{133m}Xe, ^{133}Xe, and ^{135}Xe [4]. These radionuclides are not only produced in nuclear weapon explosions but are also released by nuclear reactors and medical isotope production facilities. It is interesting to note that only the presence

of these radioxenon isotopes is not a sign of a nuclear weapon explosion but the detection of these isotopes in certain ratios is indicative of a nuclear weapon test [5-14]. This stems from the fact that uranium and plutonium (two of the most common fissile elements) have various thermal and fast fission neutron cross-sections which lead to the production of these isotopes in fixed ratios which is orders of magnitude different during reactor operations and nuclear weapon explosions.

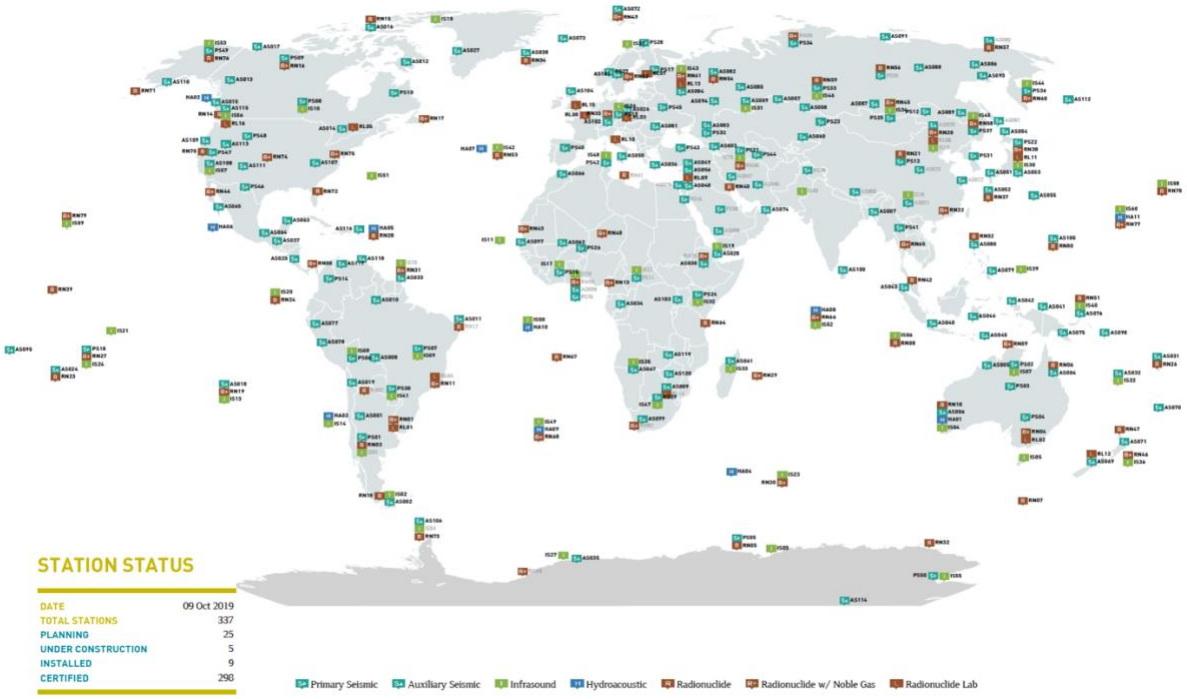

Fig. 1. Locations of IMS stations all across the world

1.2 State of the art and Drawbacks

In the current radioxenon detection systems, there are primarily two units: the gas processing unit and the radiation detection unit. The gas processing unit is responsible for sampling the air in the atmosphere and extracting pure xenon samples which will be used in the detection system to determine the activity of each radioxenon isotope of interest. The CTBTO requires that each noble gas detection system on the IMS network have a Minimum Detectable Concentration (MDC) of below 1 mBq/m^3. These systems are also responsible for having a counting time of fewer than 24 hours and must report data to the International Data Center (IDC) once a day. Also, the noble gas detectors are expected to detect a nuclear weapon explosion of at least 1-kt with an accuracy of

90% within 14-days of the event [15-16]. Two prominent detection strategies were employed by the international community to detect radioxenon: coincidence-based detection and high-resolution spectral analysis. These state-of-the-art systems suffer from several drawbacks including memory effect, susceptibility to electric and magnetic fields, poor energy resolution, high maintenance cost, and complex gain matching amongst others. Despite these shortcomings, these detectors are also very expensive costing about $500,000 just for the detectors and 7% annual maintenance (SAUNA detection system). The entire SAUNA detection system, which includes the gas processing unit costs about one million dollars [17-24].

Several radioxenon detectors were designed at Oregon State University in the radiation detection group to overcome some of these shortcomings. This was accomplished by the choice of material used for detecting various radiation coupled with custom electronics/ pulse processing and detector configuration/ geometry [25-39]. These detection systems have seen varying degrees of success in overcoming the shortcomings listed above. The Stilbene-Strontium Iodide (Stilbene-SrI_2) detection system uses a cylindrical stilbene gas cell in the capacity of an electron detector and a gas cell in conjunction with two strontium iodide detectors for photon detection. The stilbene cell is surrounded by two D-shaped strontium iodide detectors. Since all the detection media are scintillators, silicon photomultipliers (SiPMs) are used for light collection from both the detection media. Two SensL J-Series SiPM arrays were used for each of the SrI_2 detectors while a single array was coupled to the Stilbene gas cell for sensing photons [40]. The anode signals from the SrI_2 SiPM arrays were then read by two of the eight channels of the Digital Pulse Processor-8 (DPP8). The signal from the Stilbene SiPM was read by one of the channels in the DPP8 [35]. The 8-channel DPP is responsible for identifying coincidence events in real-time and transferring the pulse data to the MATLAB user interface for amplitude determination and plotting. Some of the previous detector designs suffer from electron backscatter, memory effect, complex gain matching, and poor photon solid angle. This detection system employs a Stilbene gas cell which has a near-unity intrinsic efficiency for detecting electrons and since Stilbene is a hydrocarbon (low Z), it offers no electron backscatter. The

crystalline nature of the stilbene gas cell also ensures that xenon gas molecules do not diffuse through the walls of the scintillator thereby offering a near-zero memory effect. The use of two SrI_2 detectors play an important role in maintaining a relatively high photon detection efficiency. This directly results in improving the MDC of the system. This system retains several positive aspects of previously designed detectors while attempting to overcome some of their shortcomings.

1.3 Objectives

This dissertation covers the detector design of the Stilbene-SrI_2(Eu) detection system, the process of choosing the detection media and light readout mechanisms, the pulse processing/ readout electronics, particle/ optical photon transport and distributions, calibration and characterization of the detection system. Emphasis has been laid on the results obtained from the radioxenon measurements, the Regions of Interest (ROI) methodology, experimental and simulation-based efficiency measurements, followed by MDC and memory effect calculations. Some of the key aspects covered in this dissertation are detailed below:

- Detector design and material selection.
- Detector readout and pulse processing.
- Monte Carlo N-Particle and Geant4 simulations.
- Detector calibration and characterization.
- Regions of Interest (ROI) methodology and implications.
- Radioxenon measurements and efficiency calculations.
- Memory effect and MDC calculations.
- Potential improvements for future designs.

2. LITERATURE REVIEW

2.1 Identifying Nuclear Weapon Explosions With Noble Gases

In the event of a nuclear weapon explosion, several radioactive elements are generated in the process. Identifying nuclear weapon explosions on the surface of the earth, underwater, or in the atmosphere is relatively easy because of the huge mushroom cloud and the elevated levels of radioactivity in the neighboring region. Such events can also be easily identified using state-of-the-art satellite imaging technology. However, detecting underground nuclear weapon tests is relatively hard because of the absence of the aforementioned signatures. Satellite imaging is also not always effective to positively identify such events. Therefore, the international community has relied on a combination of seismic, infrasound, hydroacoustic, and radionuclide signatures to identify subsurface nuclear weapon explosions [2]. It is worth pointing out that, out of these technologies, only radionuclide signatures provide the definite confirmation that an event was nuclear in nature.

2.1.1 Importance of Radioxenon

As mentioned previously, in the event of a subsurface nuclear weapon explosion, a large number of radionuclides are produced in the blast chamber. Most of these radionuclides are trapped underground and don't contribute to providing any evidence/ signatures about the nuclear weapon explosion. Noble gases like xenon are important because of four key reasons: their inert chemical nature, relatively high yield, ideal half-life, and coincidence decay mechanism. This section covers each of these points in detail and highlights the importance of xenon in the underground nuclear weapon detection community [41-45]. Literature has identified multiple successful long range noble gas detection in the past [46-58].

2.1.1.1 Inert Chemical Nature – Noble gas

Most of the radionuclides produced in an explosion end up forming chemical compounds with elements in the blast chamber rendering them incapable to escape the

underground environment. On the contrary, noble gases like xenon and krypton are also produced in the explosion but because of their stable outer shell electron configuration, these elements don't readily participate in forming chemical bonds even under extreme temperatures and pressures. Within a couple of hours after the explosion, these noble gases start escaping the blast chamber and dilute downstream (undergoing atmospheric transport) with time. Previous research in this area has also shown that this venting process is periodic and is highly dependent on the temperature and pressure changes that occur during the night and day in the region.

2.1.1.2 High Independent and Cumulative Yield

Xenon radioisotopes have one of the highest independent and cumulative fission yields. These xenon isotopes of interest have a cumulative yield of upwards of 6%. This ensures that huge quantities of xenon isotopes are released from the blast chamber following a nuclear weapon explosion. Although these xenon isotopes dilute by orders of magnitude as they travel thousands of kilometers, having a large source term enables the detection of these xenon isotopes even at several far off IMS stations. It is worth pointing out that in the decay of ^{133m}Xe it releases a conversion electron and an X-ray to decay into ^{133}Xe which has a relatively long half-life. Fig. 2 shows the double hump fission yield curve and points to the high yield of xenon radioisotopes [59]. Table 1 shows the cumulative fission yields for the radioxenon of interest from thermal and fast fission of ^{235}U and ^{239}Pu respectively [60].

Table 1. Thermal and fast fission yields of ^{235}U and ^{239}Pu

Isotope	^{235}U- Thermal	^{235}U- Fast	^{239}Pu-Thermal	^{239}Pu-Fast
^{131m}Xe	0.0313 ± 0.003	0.0365 ± 0.0031	0.041 ± 0.004	0.0444 ± 0.0044
^{133m}Xe	0.189 ± 0.015	0.190 ± 0.015	0.216 ± 0.016	0.223 ± 0.021
^{133}Xe	6.60 ± 0.11	6.61 ± 0.13	6.99 ± 0.13	7.03 ± 0.33
^{135}Xe	6.61 ± 0.22	6.32 ± 0.18	7.36 ± 0.24	7.50 ± 0.23

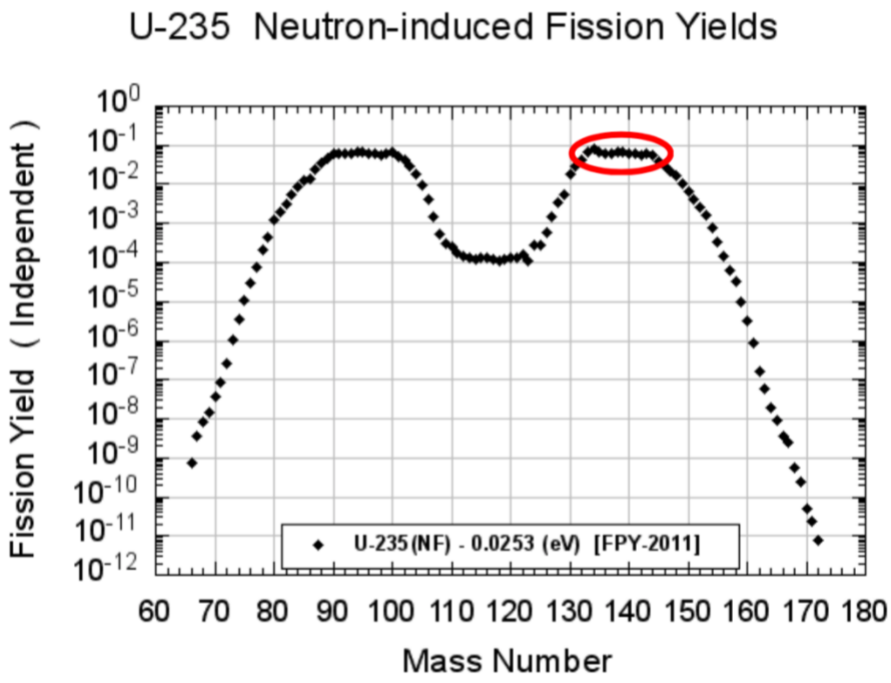

Fig. 2. Thermal fission yield curve for ^{235}U. High independent fission yield xenon radionuclides are identified in red

2.1.1.3 Ideal Half-lives

The four radioxenon isotopes of interest, namely, ^{131m}Xe, ^{133m}Xe, ^{133}Xe, and ^{135}Xe have half-lives in the range of a couple of hours, like in the case of ^{135}Xe to a couple of days for ^{131m}Xe. These radiological characteristics are very important because it ensures that the half-lives are neither too short that the radionuclides decay below detection limits before reaching the IMS station and neither too long that they linger in the atmosphere for too long, saturate the atmosphere (thereby elevating background) and provide no effective temporal data. It is worth pointing out that other noble gases that are also produced in large quantities in a nuclear weapon explosion (argon/ krypton isotopes) but because of their short half-life, they have not received considerable attention from the international community [61-67].

2.1.1.4 Coincidence Decay Scheme

Coincidence based decay of the radioxenon isotopes of interest is one of the most important features which enables low activity measurements. This means in the process of decay; xenon isotopes release an electron and a photon at virtually the same time. Most of the radioxenon detection systems that are used in the IMS stations and those developed by research groups around the world involve the use of an independent electron and photon detector. The phenomenon of coincidence decay is relatively rare in nature which permits the elimination of a large portion of background events (singles). Table 2 illustrates the decay energies and branching ratios of ^{131m}Xe, ^{133m}Xe, ^{133}Xe, and ^{135}Xe [15].

Table 2. Coincidence decay properties of the radioxenon of interest

Isotope	Decay energy (keV)	Branching ratio (%)
^{131m}Xe ($t_{1/2}$ = 11.93 days)		
X-rays: XKα_2	29.46	15.4
X-rays: XKα_1	29.78	28.6
X-rays: K'β_1	33.60	10.2
X-rays: K'β_2	34.61	1.85
Gamma rays	163.93	1.95
Conversion electrons	129.4	61
Coincident decays	X-ray and 129 keV e^-	56.1
^{133}Xe ($t_{1/2}$ = 5.35 days)		
X-rays: XKα_2	30.62	14.1
X-rays: XKα_1	30.97	26.2
X-rays: K'β_1	35.00	9.4
X-rays: K'β_2	36.01	1.7
Gamma rays	80.99	37
Conversion electrons	45	55.1
Betas (max energy)	346	100
Coincident decays	X-ray + 45 keV e^- + 346 keV beta	48.9
	81 keV gamma + 346 beta	37.2
^{133m}Xe ($t_{1/2}$ = 2.19 days)		
X-rays: XKα_2	29.46	16.1
X-rays: XKα_1	29.78	29.8
X-rays: K'β_1	33.60	10.6
X-rays: K'β_2	34.61	1.9
Gamma rays	233.2	10

Conversion electrons	198.7	64
Coincident decays	X-ray and 199 keV e^-	58.4
^{135}Xe ($t_{1/2}$ = 0.38 days)		
X-rays: $XK\alpha_2$	30.62	1.45
X-rays: $XK\alpha_1$	30.97	2.69
X-rays: $K'\beta_1$	35.00	0.97
X-rays: $K'\beta_2$	36.01	0.185
Gamma rays	249.8	90
	608.2	2.9
Conversion electrons	214	5.7
Betas (max energy)	910	100
Coincident decays	X-ray + 214 keV e^- + 910 keV beta	5.7
	249.8 keV gamma + 910 keV beta	90

2.1.2 Nuclear Reactors vs Weapons – The Difference

Radioactive isotopes of xenon are released in the atmosphere even during reactor operations and in the process of producing medical isotopes at medical radioisotope facilities. Multiple avenues generate radioxenon of interest, therefore, it is the ratio between these isotopes that is key to the identification of its origin and not the absolute concentration of each radioisotope. The isotopic ratios between $^{135}Xe/^{133}Xe$ and $^{133m}Xe/^{133}Xe$ are very different for a reactor release and a nuclear weapon explosion enabling the discrimination between these two events [7,68]. Fig. 3 shows the typical plot of the discrimination between data from reactor operations and nuclear weapon tests [69]. On the left-hand side of the image, releases from reactor operations are plotted and on the right-hand side of the image, data from nuclear weapon tests are shown. A theoretical discrimination line was developed between these two classifications of events (dashed line). As can be observed from the image, the ratios between the two releases are orders of magnitude different which enables the successful discrimination between the events. The reader is reminded that the x and y axis in Fig. 3 are in log scale. Although releases from medical isotope production facilities are not plotted in this figure, their releases are often located around the dashed line making it hard to determine the nature of the release. Literature has pointed out that irradiation of fresh low enriched or high enriched uranium fuel can often release signatures similar to a nuclear weapon explosion. Therefore, in the past decade, considerable research in

radiation measurements and atmospheric transport models have focused on accurately recording background near medical isotope production facilities and developing advanced models to better predict the source of the release.

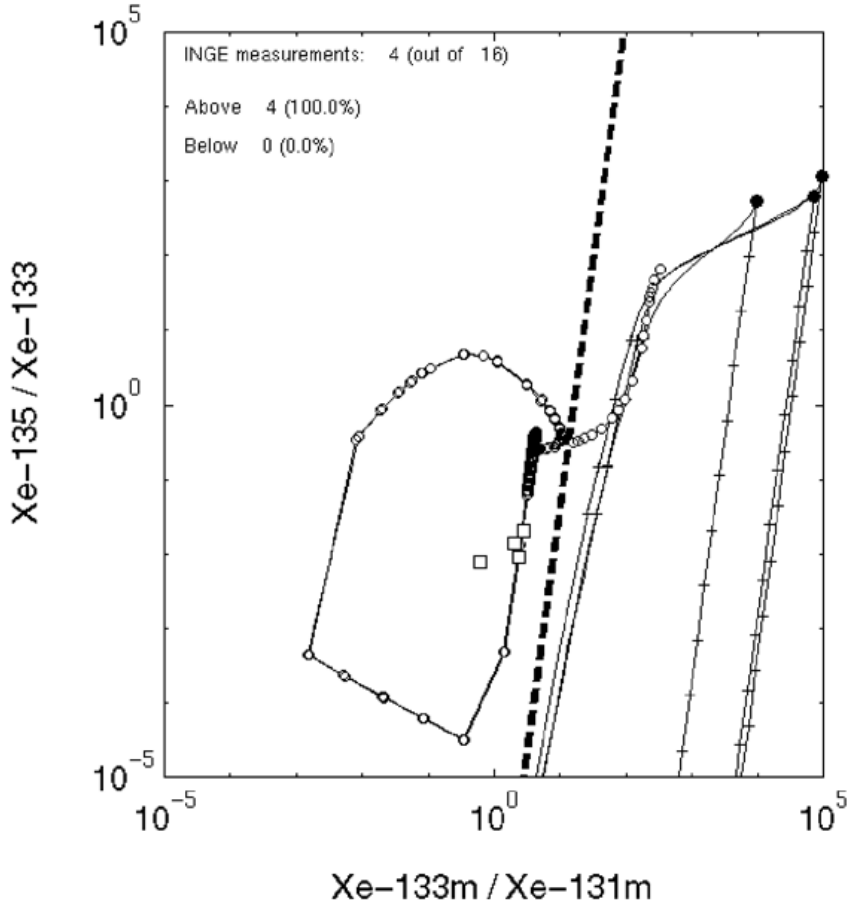

Fig. 3. Radioxenon releases plotted from reactor operations and nuclear weapon explosions along with a discrimination line between the two events

2.1.3 Other Noble Gases

Literature has indicated that other xenon isotopes are also produced in a nuclear weapon explosion (^{125}Xe or ^{127}Xe). These xenon isotopes are generated in low quantities or are used indirectly for quality assurance and quality control for comparison of detection systems developed by various groups around the world (^{127}Xe). ^{125}Xe for example has multiple coincidence decay paths but because of its relatively short half-life (~16.9 hours) and no delayed production the concentration of ^{125}Xe is expected to fall below detection levels [70-71].

Observing the fission yield curve, it can be seen that other noble gases are produced in considerable quantities like krypton. The three most important parameters while looking for other candidates for identifying the nuclear weapon explosions are the yield, the half-life, and the decay scheme of the isotope. While krypton isotopes are produced in large quantities, these isotopes either have a very short or very large half-life. Kr-85m is of interest because of its coincidence decay scheme and its production in significant quantities. The drawback of using ^{85m}Kr is its relatively short half-life of about 4.4 hours. Taking into account the fission yield and the time it takes for gases to vent from an underground blast chamber, undergo dilution/ atmospheric transport, and eventually reach the IMS station, there is very little activity left in the gas sample to be detected by these systems. This is not taking into account the gas sampling and processing times which often run for a couple of hours. Other gases like ^{85}Kr and ^{37}Ar have also been explored, these are some of the other noble gases that are produced in a nuclear weapon explosion. The drawback of these radionuclides is that ^{85}Kr has an atmospheric background of about 1.5Bq/m^3 and a long half-life which makes any additional release from a nuclear weapon explosion hard to detect. While on the other hand ^{37}Ar releases a 2.8 keV auger electron which is comparatively hard to measure because of the thresholds of the detection system [61-67].

2.1.4 Underground Release Patterns

Clandestine nuclear weapon explosions are generally carried out by nations to prevent international attention and to test their technology which can be used for offensive purposes. When an explosion happens, the rock and soil around the area tend to expand because of the immense heat and pressure. Most of the radioactive gases are trapped in the expanded rock. Gradually as temperature reduces, the rock also shrinks and is forced to expel the radioactive gas that is trapped in its volume. This is precisely the reason why it takes some time for gases to reach the surface of the earth after a nuclear weapon explosion. Temporal trends have also been observed during day and night times where elevated radioactive gas activity has been observed during the night. This can again be attributed to the temperature changes during night and day and the process of thermal expansion and contraction that leads to more releases during the night. Fig.

4a shows the downwind radioxenon activity as a function of time from a subsurface nuclear weapon explosion. Fig. 4b shows the temporal changes in ^{133}Xe release from an underground weapon explosion [72]. The similarity in both plots is the spikes that are observed as a function of time. Recent studies have concluded that factors like atmospheric pressure also play a crucial role in the amount of gas that is vented post an underground weapon explosion [42,59,73].

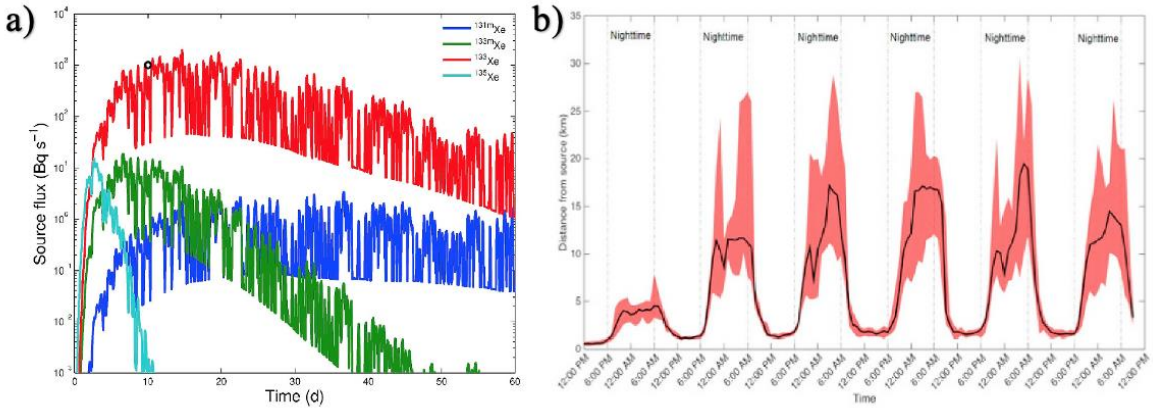

Fig. 4. a) Simulated release of the four radioxenon isotopes of interests from a 2.3 kt weapon explosion at a depth of 323 m and a permeability of 3.9 darcys; b) downwind simulation of ^{133}Xe for six days, black curve is the median value while the red shaded area is the 10th and 90th percentile of the release

2.1.5 Radioactive Decays of Interest

Several radiations are released in the process of radioxenon decay. Some of the most prominent are gamma and X-rays from a photon standpoint, and conversion electrons (CE) and beta particles from an electron standpoint. We shall be going over each of these decay paths and identify the differences and their significance for radioxenon detection.

X-rays are low energy photons that are produced due to orbital electron transitions or interaction of an external charged particle with the nucleus. When an inner orbital electron is knocked off its orbit, the outer orbital electrons undergo a drop in energy to fill the vacancy that was created in the inner orbital. Such an electron transition leads to a release of a photon with energy equivalent to the difference between the orbitals where the electron has transitioned from and its current orbital. Such X-rays are called

characteristic X-rays, these photons are also useful in identifying the element because each element has a unique signature of X-rays released because of the differences in energy levels. The second form of X-rays is termed bremsstrahlung radiation. This is a German term that means stopping radiation, these radiations are produced from the negative acceleration (deceleration) of the electron as it approaches the nucleus. These X-rays don't have fixed energy because the energy released in this mechanism is dependent on the initial energy of the electron, approximately 99% of the electron's energy is dissipated as heat and the remaining 1% of the electron energy contributes to the production of X-rays. It must be brought to the reader's attention that this radiation is not of much importance from a radioxenon detection standpoint. Fig. 5 shows the characteristic X-rays (K_α and K_β) from a molybdenum target riding on top of the bremsstrahlung spectrum [74].

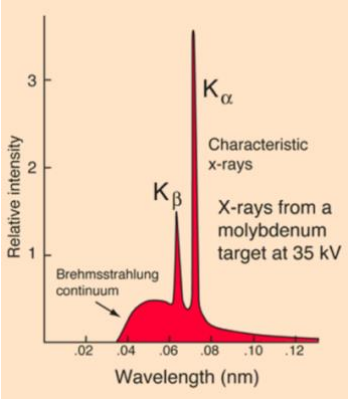

Fig. 5. Characteristic X-rays and the bremsstrahlung spectrum from a molybdenum target

The next photon radiation of interest is gamma photons. After a radionuclide has undergone a decay or transition, gamma photon release is one of the forms of de-exciting the nucleus. It is worth pointing out that there is no change in the atomic or mass number of nuclides in this process. The term *gamma* is however used to highlight the difference in the origin of the photon (X-ray: outside the nucleus; gamma: inside the nucleus). During the process of gamma transition, not all energy is released in the form of a photon, a small amount of recoil energy is also absorbed by the nucleus. Gamma transitions that are released from a radionuclide are discrete in nature.

Beta is the next form of decay that shall be discussed. This is of profound interest from a radioxenon detection standpoint because two of the four isotopes of interest decay via this mechanism (^{133}Xe and ^{135}Xe). This form of decay is very prominent in neutron-rich atoms. The general equation for beta decay is provided in equation 1.

$$ {}^{1}_{0}n \rightarrow {}^{1}_{1}p + {}^{0}_{-1}\beta + {}^{0}_{0}v + \mathrm{Q}_{\beta} \qquad (1) $$

It must be pointed out that for this work, we are only concerned about β^- decays, these are the events that release an electron in conjunction with an anti-neutrino. In such events, the energy that is released is shared between the electron, anti-neutrino, and the residual nucleus. These events generally result in an increase in atomic number (proton) but retain the mass number (proton + neutron). Among the particles/ nuclides that are released in beta decay, the only particle that is readily detected is the electron. It must be highlighted that since there is an energy sharing in place between the three resultants of beta decay, each electron will start with a different energy. The remaining energy is shared between the anti-neutrino and the daughter radionuclide. Fig. 6 shows a beta minus decay spectra of ^{64}Cu. The energy with the highest energy probability is about one third the maximum beta energy [75].

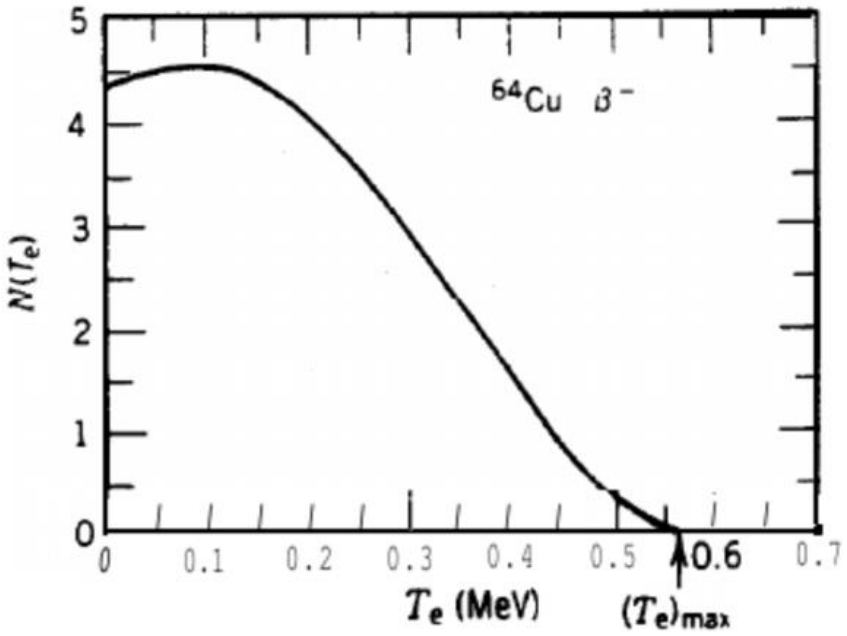

Fig. 6. Cu-64 β^- decay spectrum

It is also worth pointing out that since electrons are produced close to the nucleus, a considerable percentage of electrons end up with zero energy because they are unable to overcome the Coulomb forces of the nucleus. This is exactly the opposite scenario for a positron, the particle experiences an increase in energy because of repulsion between the nucleus and the charged particle.

Conversion electron is the last radiation of interest in our work. When a nucleus is in a state of zero spin, emission of a gamma photon followed by maintaining a state of zero spin is not feasible, since it violates the law of angular momentum. Therefore, to facilitate such an energy transfer, the nucleus directly transfers its energy to the electron. This energy transfer usually happens to the K or L shell electron. What follows is the ejection of the electron from its orbital and the transition of an electron from a high energy orbit to a low energy orbit accompanied by the release of an X-ray with energy equivalent to the difference between the two energy levels. Sometimes when this energy transfer happens to an outer orbital electron, this results in the release of a high energy electron and a low energy photon. These electrons that are released in such a process are called conversion electrons. Emission of a gamma photon is sometimes slow between states that have low energy difference or a large difference in spin, in such cases, internal conversion provides a faster alternative. A prominent example is the transition of ^{137}Cs to ^{137}Ba where about 10% of the times a conversion electron is accompanied by the release of an X-ray photon (Fig. 7) [76].

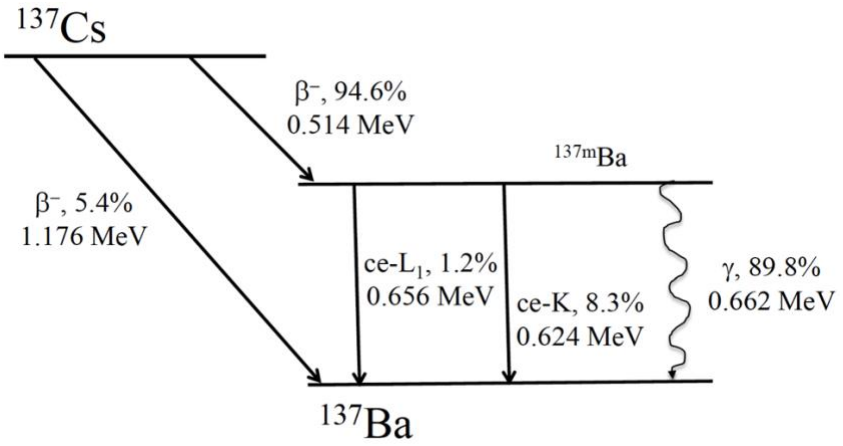

Fig. 7. Decay scheme of ^{137}Cs to ^{137}Ba

2.1.6 Coincidence Based Decay

For the detection of radioxenon, most of the research groups around the world have resorted to using coincidence-based detection systems. These detection systems look for a trigger between the electron and photon detector within a set time frame (coincidence detection window). If a coincidence event is detected, it records the signals and if no coincidence signal is received before the window elapses the system classifies the event as a stray background/ singles event. Out of the four major radioxenon detection systems, three of them operate on the concept of coincidence-based detection while the other system operates on high-resolution gamma spectroscopy. The Automated Radio-xenon Sampler/Analyzer (ARSA), Swedish Automatic Unit for Noble gas Acquisition (SAUNA), and the Russian Analyzer for Xenon Radioisotopes (ARIX) operate on coincidence-based detection while the French Système de Prélèvement Automatique en Ligne Avec l'Analyse du Xénon (SPALAX™) uses an HPGe detector in its system. It must however be pointed out that the new versions SPALAX detection system features a PIPSBox electron detection media in conjunction with an HPGe for photon detection. Although the high-resolution based detection systems offer excellent photon energy resolution, no electron data is recorded. This drawback is especially pronounced while trying to differentiate between the counts from ^{131m}Xe and ^{133m}Xe since both of them release a low-energy photon in coincidence with a conversion electron. One proposed solution is to use the relative half-lives in ascertaining the counts coming from the two metastable isotopes but since the CTBTO requires the detection systems to report data once every 24-hours, this method is not practically feasible. Another challenge faced by the radioxenon detection systems is that of radon. Radon isotopes decay into ^{214}Pb and ^{214}Bi which release photons at 242, 79.3 keV that interfere with the ^{135}Xe and ^{133}Xe gamma photons. Several methods have been suggested to deal with this issue, but the most prominent method is to inject a sample of radon in the detection system and observe the ratio of counts in various regions and subtract these counts from the actual xenon measurement. An alternative solution to this problem is improving the detector energy resolution to ensure that there is adequate separation between the energies of interest so that the peaks can be appropriately resolved [77-79].

2.2 Detection Media and Hardware

For radiation detection, there are essentially three areas that are of utmost importance: detection media, pulse processing electronics, and algorithms, software. For radioxenon detection, since there is no complex image reconstruction, we shall be focusing our attention on only the detector elements and the pulse processing electronics. We shall initially be going over the process of scintillation detection with focus on cerium bromide, strontium iodide, and stilbene detectors. This will be followed by a brief section on silicon photomultipliers (SiPMs), the Field-programmable Gate Array (FPGA), and digital electronics for radiation detection.

2.2.1 Process of Scintillation

Radiation detectors can be broadly classified into three detection technologies: gas detection, scintillation detection, and solid-state detection. For most purposes involving high-resolution gamma spectroscopy, scintillation, or solid-state detectors are the choices of technology. Gas-filled detection systems are mostly used for counting purposes where the exact energy deposition in the media is not of interest (especially in high radiation areas). In its most simple form, the process of scintillation detection is as follows: ionizing radiation deposits its energy in the scintillation medium and this energy is converted into visible or UV photons, these photons are then sensed by a light collection device like a photomultiplier tube (PMT) or a silicon photomultiplier (SiPM). Analyzing, quantifying the signal from the photon detection devices can estimate the energy deposited by the ionizing radiation in the detection media. Some of the ideal properties of an ideal scintillator include [80]:

- Converting all the energy of the radiation into detectable photons.
- Refractive index similar to that of glass (~1.5) to prevent internal reflection.
- Scintillation material should be able to be produced in large quantities.
- Number of detectable photons generated shall be proportional to the energy deposited in the crystal.
- Scintillation medium shall be transparent to its own light (no self-absorption)

- Decay time of the scintillator should be short in order to detect radiation in high count areas without pileup.

It must be brought to the reader's attention that no single scintillation medium meets all the above-mentioned criteria. Therefore, the material shall be chosen to take into account all these factors in an effort to maximize the traits we expect to see and the specific application of the scintillator.

Scintillators can be broadly classified as either organic or inorganic scintillators. Organic scintillators are generally low atomic number hydrocarbon-based chains that act as an excellent medium for charged particle detection. Mostly these are low density, relatively inexpensive, and fast scintillators (<10 ns decay time) [80-83]. Since organic scintillators are made of low atomic number elements, there is no electron backscatter experienced as opposed to high atomic number elements. From a radioxenon detection standpoint, organic scintillators are more prone to memory effect, a phenomenon where gases tend to diffuse through the walls of the scintillator and reside at these locations until they decay. This results in significant background elevation and is often undesirable. A notable exception to this is Stilbene, it is a hydrocarbon, bearing a crystalline structure; therefore, it is not susceptible to memory effect. Stilbene has also been extensively used for neutron-gamma pulse shape discrimination [84-88].

The second class of scintillation detectors is inorganic scintillators. These are generally high density, high atomic number, crystalline structure detection media. These materials make for excellent high-resolution photon detection media [89-92]. The high atomic number (Z) and density often translate to higher stopping power and higher light yield. Accompanying the higher light yield is relatively better energy resolution compared to plastic scintillators. In an inorganic scintillator, the excitation and de-excitation of electrons cause the release of detectable photons. The electrons in an inorganic scintillator are either in the valence band or the conduction band. The energy state between the two bands is called the forbidden band, and electrons are generally not found in this energy level. When ionizing radiation interacts with the scintillator,

the electron in the valence band is elevated to the conduction band. When the electron is in the conduction band, it is free to mobilize across the crystal, and in the process of de-excitation back to the valence band, the electron ends up releasing a photon. These photons are sometimes high energy (short wavelength) and are not readily detectable, therefore generally scintillators are not used in their pure state but are rather infused with impurities. This is generally done to enhance the number of photons that are emitted in the visible photon range. These impurities that are added are called activators; they create special activation sites in the lattices which results in the modified energy band structure of the pure scintillators. This results in the creation of energy bands even in the forbidden band gap. Fig. 8 shows an example of the energy band structure of a doped crystal [93].

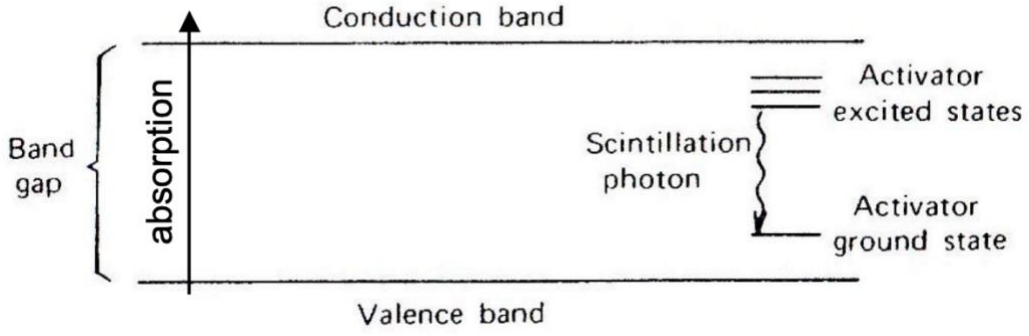

Fig. 8. Energy band structure of an activated inorganic crystal

The next important fact about scintillation detectors is the concept of fluorescence and phosphorescence. The emission of prompt photons right after the ionizing radiation has deposited energy in the scintillation medium is called fluorescence. Phosphorescence on the other hand is the emission of photons, often with lesser energy (higher wavelengths). Phosphorescence is also accompanied by a significant time delay (as the molecule might undergo intersystem crossing to a triplet state) The energy level diagrams of fluorescence and phosphorescence are shown in Fig. 9 [94]. The third mechanism of scintillation is delayed fluorescence. In this process, the emission spectra remain the same as fluorescence but are characterized by a much longer emission time. From a radiation detection standpoint, we are often interested in fluorescence because

this is the mechanism that enables the release of optical photons with the least amount of time delay. A drawback about delayed emission of photons is that these photons are hard to discriminate against background noise and are therefore not accounted for in the energy measurement process. It is worth mentioning that since we are focusing on performing spectroscopy, which means we are interested in the individual energy deposition of each photon as opposed to current mode operation where we are interested in the sum over a certain time frame, any delays in the light output from the scintillator increases the probability of a portion of the energy deposited in the scintillator not being accounted for by the system.

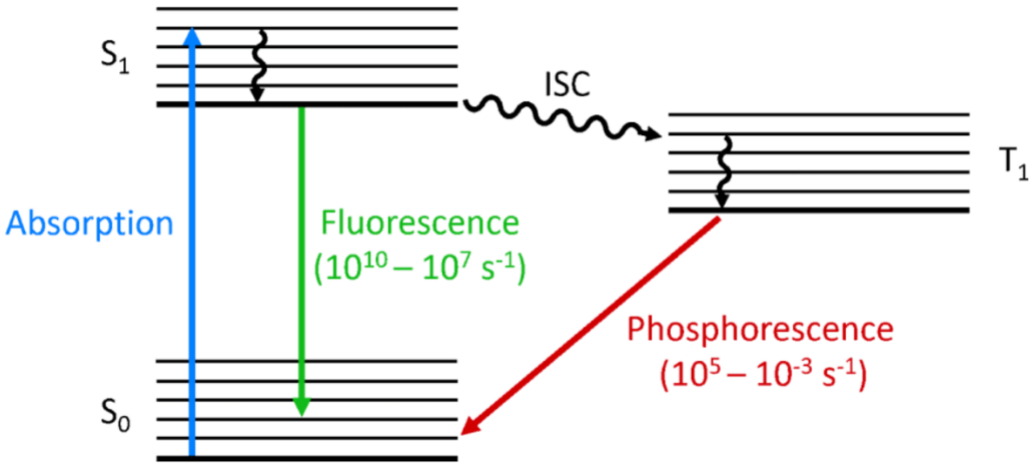

Fig. 9. Timescale of de-excitation via fluorescence and phosphorescence

The decay time is a quantity of importance for a scintillator. This is the amount of time for a scintillator emission to reach from its maximum to 1/e or about 36.7% of its maximum emission. The variation of scintillation intensity with time bears an exponentially decaying correlation. Therefore, for example, if a scintillator has a decay time of 2 μs, the amount of time we are required to integrate the pulse to estimate full energy deposition is about 5 to 6 times its decay time. When ionizing radiation deposits its energy in the scintillator, many events take place, first is the elevation of electrons from the valence band to the conduction band. If the scintillator has a short decay time, the majority of the photons are de-excited by fluorescence. This is often a desirable quality in a scintillator since we can use this in a situation with large count rates. Simultaneously in the scintillator, there are other processes taking place like absorption

and re-emission. These processes generally cause a delay in the scintillation light being emitted by the scintillator. Several scintillators have two decay components, a scintillator that emits a majority of the energy absorbed by the ionizing radiation in the process of fluorescence is an ideal candidate for radiation detection. Some of the most common examples of multiple decay components include NaI(Tl), SrI_2(Eu) which have two primary decay components. Fig. 10 shows an example of the effect of having multiple decay components [95]. It must however be pointed that a scintillator can have more than two decay components as well.

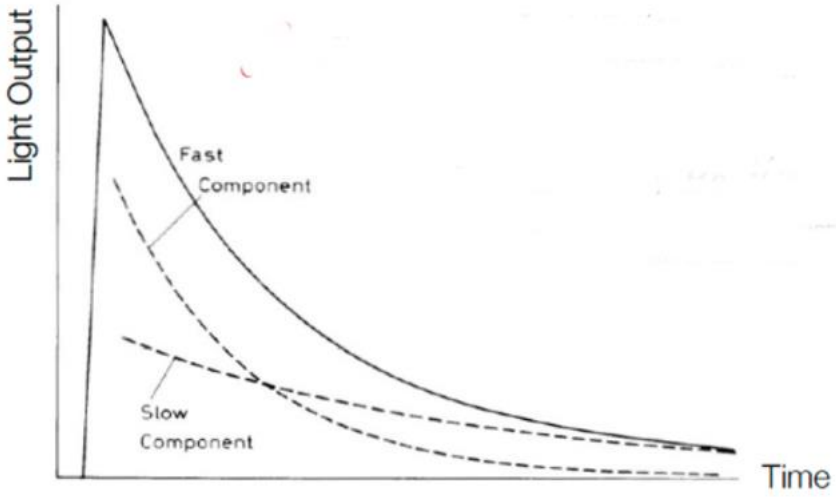

Fig. 10. Plot illustrating the various decay components of scintillators

2.2.2 Gamma Ray Spectroscopy

Gamma-ray spectroscopy is the process of measuring the energy deposition of a photon in a detection medium. This is particularly important when we are in an environment with several radiation sources and need to identify each source individually. Situations where gamma spectroscopy is important include, border security, homeland security, oil well logging, industrial measurements amongst others. Counters are useful in identifying the presence of radioactivity in the vicinity, but this system doesn't provide any information regarding the specific radionuclide that is responsible for the emissions. This is where spectroscopy plays a crucial part. The basic working principle of spectroscopy is that each radionuclide emits a unique signature of photons or electrons. If we are successfully able to match these emissions with a pre-recorded

sample measurement, we can be assured about the radionuclide. For example, ^{137}Cs emits a 662 keV gamma photon and a 31 keV X-ray. If both these signatures are detected in an unmarked sample, there is a very high probability that ^{137}Cs is responsible for these emissions. In the field of gamma-ray spectroscopy, the resolution of the detector is very important. By definition, the term resolution means the ability to differentiate between two lines in a histogram with high confidence. If we have a high-resolution detector like HPGe, then two energy peaks that are very close to each other can be identified with a high level of confidence. As an example, Fig. 11 shows the spectra collected from NaI and HPGe using the following sources: ^{137}Cs, ^{133}Ba, and ^{60}Co. ^{137}Cs has a peak at 662 keV, and ^{60}Co has two peaks at 1.17 and 1.33 MeV [96]. ^{133}Ba has multiple peaks between 200 and 390 keV. As seen in the spectrum, the HPGe peaks are very well resolved, and each peak is clearly identified. On the other hand, the spectrum from NaI shows that the peaks weren't successfully resolved and there is a significant overlap between the peaks leading to a single broad peak.

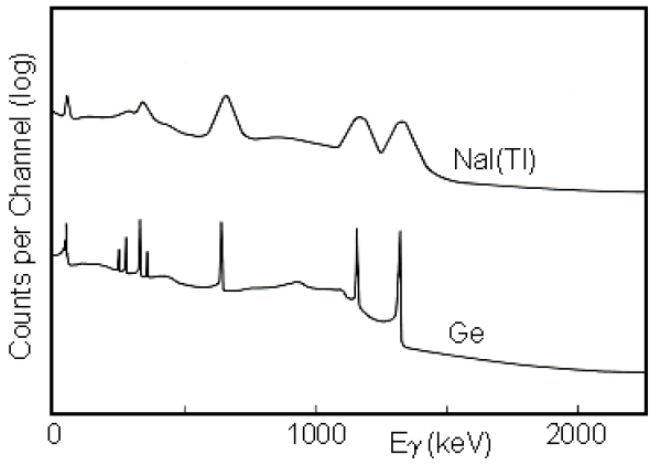

Fig. 11. Spectral differences in resolution observed in an NaI(Tl) and Ge detector using ^{60}Co, ^{133}Ba, and ^{137}Cs. NOTE: The spectrum is represented in log scale

Some other interesting features to note in the spectrum are that the number of counts in the germanium detector is significantly less compared to the NaI detector. This is because the detection efficiency of Ge is lower than that of NaI. This is important

because in some applications, we are required to have both high resolution as well as high density and/or atomic number for the detection medium. The remainder of this section shall go over the physics behind photon interaction with matter. Generally speaking, three main interaction mechanisms result in energy transfer or the creation of new particles: photoelectric effect, Compton scattering, and pair production. The photoelectric effect is the interaction where a photon deposits its entire energy to an inner orbital electron and the photon ceases to exist. These kinds of interactions are generally preferred because this helps in identifying the radionuclide responsible for emitting the photon. The second type of interaction that shall be discussed is Compton scatter. This is more prominent in low Z or high energy photons. In this interaction, the photon partially deposits its energy to an orbital electron. The photon doesn't cease to exist, but it has relatively less energy compared to the initial photon energy. These kinds of interactions are not preferred because this process doesn't yield any information regarding the initial photon energy which can be used to ascertain the radionuclide responsible for the emission. The third type of interaction, although less prominent for this project is pair production. This is an interaction where a photon with a minimum energy of 1.022 MeV interacts with the nucleus of the detection material and creates an electron-positron pair. As these charged particles traverse through the detection medium, they deposit their energy and when the positron has very low energy, it annihilates itself with a nearby electron releasing two 511 keV photons in opposite directions. These interaction types are highly dependent on the atomic number of the detection medium and the energy of the incoming photon. Fig. 12 shows a plot of the regions where each of these interaction mechanisms are prominent as a function of the incoming photon energy and the atomic number of the detection medium [97].

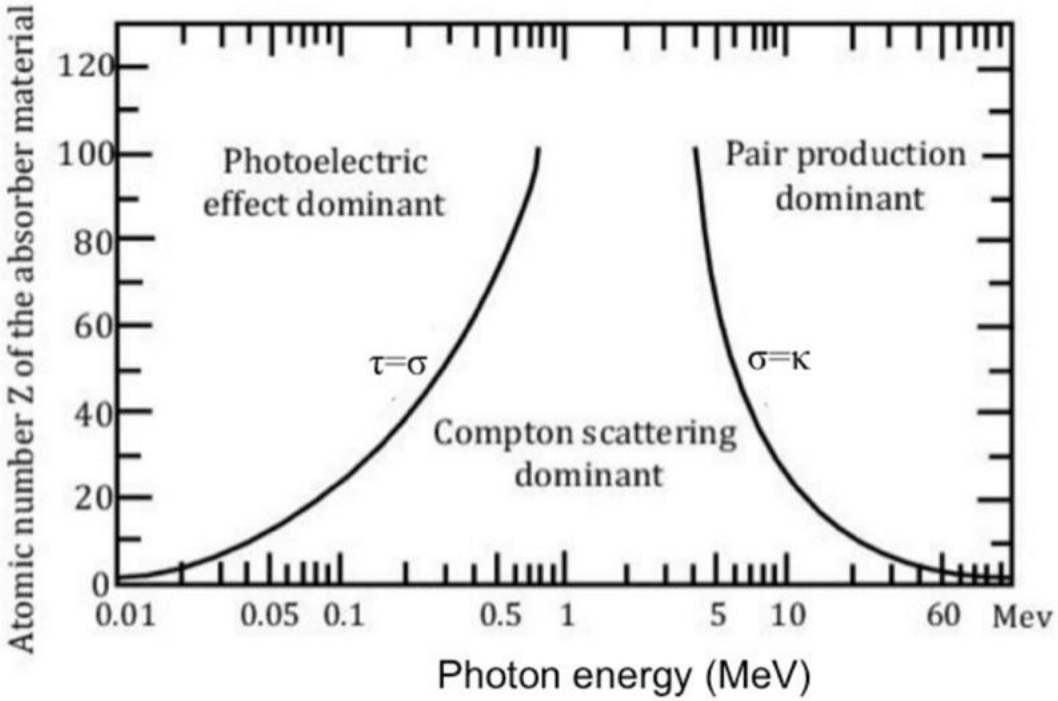

Fig. 12. Curve describing the prominent interaction mechanism as a function of photon energy and target atomic number (Z)

2.2.3 Photon Detector

For this study, it was decided to opt for a well-type/ thru-hole detector design to attain high photon detection efficiency. Keeping that in mind, initially it was decided to use CsHfCl (CHC), a scintillator that was grown in the past 5 years. This is one of the first inorganic halide-based scintillators which is non-hygroscopic. In terms of resolution and efficiency, it was better than NaI, but its non-hygroscopic nature was the key factor in initially choosing this material. The high cost and non-availability of machining experts led to the exploration of new scintillator materials. The next option explored was lanthanum bromide. This material is most preferred for scintillation detection with some research groups reporting a 662 keV peak resolution of about 2.00% FHWM. Some drawbacks of this crystal are the inherent radioactivity in the form of ^{138}La, a radioisotope of lanthanum that can't be separated in the crystal growth process. This drawback can be overcome to a certain extent for our application since the radioxenon isotopes of interest for this project decay via coincidence. Therefore, the decay of ^{138}La wouldn't be recorded by the system since these are single events. The challenge faced

with $LaBr_3$ was that it was incredibly hard to machine and maintain structural integrity. Therefore, SrI_2 was explored for this project but challenges concerning structural integrity again forced the exploration of new scintillation materials. Table 3 shows some of the properties of the prominent scintillators that were explored for this work [98-103].

Table 3. Scintillation properties of some of the scintillators explored for this work

Scintillator	$LaBr_3$	SrI_2(Eu)	Enhanced CsI(Tl)	$CeBr_3$
Light Yield (#/MeV)	73,000	~90,000	~85,000	68,000
Decay time (ns)	25	1000-5000	1000	20
Effective Z	44	49	54	46
Density (g/cc)	5.08	4.55	4.51	5.2
Resolution (%)	2.2	2.9	4.5-5	4.0
Hygroscopic	Yes	Yes	Slightly	Yes
Emission peak (nm)	385	435	550	370

Cerium bromide ($CeBr_3$) is one of the relatively new scintillation materials that has been explored since the early 2000s. Its high density, light yield, effective Z number, and resolution make it one of the preferred scintillator materials for spectroscopy applications. Upon contacting crystal growers, it was confirmed that $CeBr_3$ is relatively easy to machine. This scintillator has been explored in the past for several applications but never for radioxenon detection, which makes it one of the ideal candidates for this research.

2.2.4 Electron Detector

For this work, several options were available to serve in the capacity of an electron detector. In the past, research groups have resorted to using plastic scintillators and PIPSBox for detecting electrons. In this project, it was decided to employ an electron detector that has a near 4π solid angle for electron detection. Therefore, the best option available was the use of a well-type detection system which can be accomplished by a low Z, easy to machine material. A small hole shall be machined on top of the scintillator to accommodate the gas line for injecting the radioactive gas sample. A plastic scintillator stands out as one of the best options available for an electron detector. It must however be pointed out that plastic detection media have been used by a number of research groups around the world for the purpose of electron detection for a number of years and have identified a couple of drawbacks. Memory effect and relatively poor electron energy resolution are the primary reasons to explore other options. Therefore, for this work, it was decided to employ stilbene in the capacity of an electron detection media and a gas cell. Stilbene offers a near-zero memory effect and provides better electron energy resolution when compared to plastic scintillators.

2.2.5 Stilbene Cell for Electron Detection

In this section, we shall be going in-depth and exploring the reasons for choosing stilbene as a detection medium. Memory effect is one of the main drawbacks that has haunted the plastic detection cells on the IMS network. This is a phenomenon where residual gas from a previous measurement is left behind in the gas cell. When a noble gas is injected for measurements, the electrons are detected by the plastic scintillator and allow the passage of photons without significant attenuation. In a plastic scintillator, these gases diffuse through the plastic cell wall and reside at these locations. During the next round of measurement, these gas molecules that have diffused in the gas wall will continue to decay thereby increasing the background count rate at these locations. This is especially problematic if the radionuclide being measured is the same radionuclide that is adding to the background from a previous measurement. From a pulse processing perspective, there is no viable solution since the background

signal would be identical to the source signal. One alternative thought out by researchers is to use the principle of redundancy, where 2-4 similar gas cells with similar performance are employed. The idea here is to wait a certain amount of time for the radionuclide to decay before using the same gas cell again for measurements. This method is not practical in the long run because the CTBTO requires IMS data to be available at the IDC once every 24 hours. Stilbene on the other hand features the same elemental composition as its plastic counterpart but has a more crystalline structure. This has a couple of implications, elementally its cross-section for photon detection is similar to that of hydrocarbon-based plastic scintillators but structurally it behaves more like an inorganic crystal. This means that because of its structure, stilbene is more immune to the diffusion of gases in its walls, thereby offering about two orders of magnitude reduction in the memory effect. From a material handling perspective, stilbene is brittle in nature therefore must be handled with caution. Previous studies have also pointed out that stilbene offers about 15% better conversion electron energy resolution (129 and 199 keV) compared to conventional plastic scintillators [32].

The stilbene cell used for this work was manufactured by Inrad Optics [104]. The gas cell has a width of 18.7 mm, a wall thickness of 1.8 mm, and a total height of 21.7 mm. This detector consists of a hollow cylindrical body along with two end caps attached on the top and bottom to enclose the geometry. The end caps are 2 mm thick. The top end cap has been machined to accommodate a circular tube that acts in the capacity of a gas injection line. The bottom end cap also features a thin fused silica region to provide optical coupling to the photon detection device. The volume of the gas cell was calculated to be around 3.17 cm^3 with a solid angle of approximately 3.9π. For radioxenon measurements, it is essential to ensure that the 30 keV photons are not extensively attenuated because three of the four radioxenon of interest release this radiation in coincidence with a conversion electron or beta particle. Using MCNP simulations, it was determined that the 1.8 mm thickness of the stilbene cell walls results in an attenuation of approximately 5.4%. Fig. 13 shows the sketch of the stilbene cell from Inrad Optics.

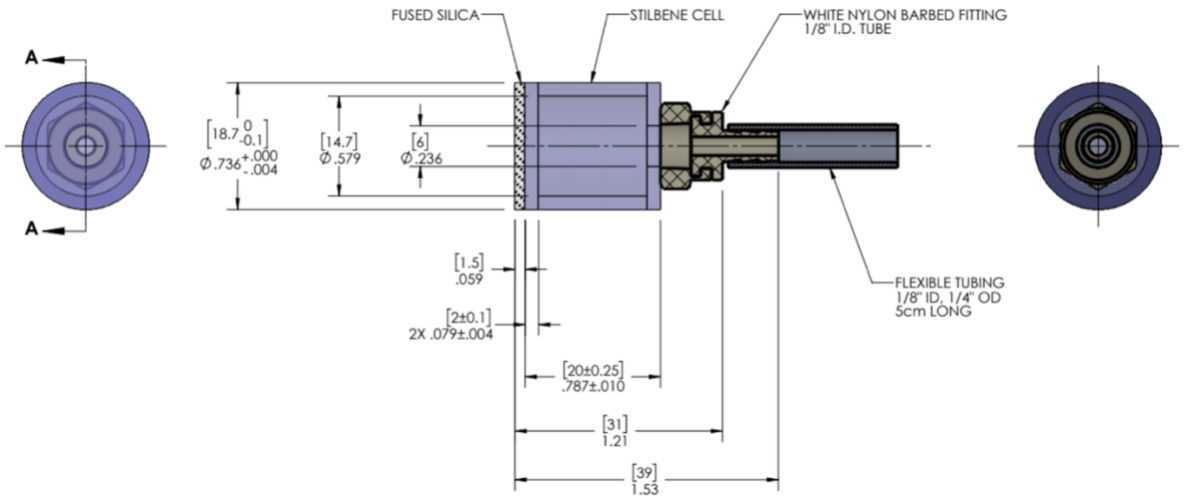

Fig. 13. Bottom, cross section, and top view of the stilbene gas cell designed by Inrad Optics. NOTE: The actual dimensions of the wall thickness and the height of the gas cell varied by 0.2 and 1.7 mm respectively during fabrication

2.2.6 Cerium Bromide

Cerium bromide is an inorganic scintillator that was grown and developed over the past two decades. This material has one of the highest scintillation light yields and offers respectable energy resolution. Several groups around the world have reported a scintillation yield between the high 60,000s and low 70,000s [105-111]. This is next only to SrI_2 which emits about 90,000 photons per MeV. Preliminary results indicated that the energy resolution was about 3.4% FWHM for the 662 keV peak, this is about half the resolution obtained by a NaI detector (Fig. 14a). The emission spectra of this scintillator indicate that at about 370 nm it reaches its emission peak (Fig. 14b). This is not ideal since most of the photon detection devices peak at about 420 nm, but it is worth mentioning that using the SensL J-series SiPMs, a considerable amount of the emission spectra can be successfully converted into electric charge. It is anticipated that the emission peak mainly originates from the 5d to 4f transition. One of the advantages of using $CeBr_3$ is its quick decay time. Initial studies indicate that $CeBr_3$ has a decay time of about 17 ns which is one of the fastest in the world of inorganic scintillators. Some larger scintillators have shown a decay time of about 20 ns (Fig. 14c). This scintillator also emits about 4000 photons per ns per MeV making it an excellent candidate for timing application, especially in the medical diagnostics field.

The next important factor to consider is linearity. Measurements were carried out in a wide energy range from 100 keV to over 1 MeV using several photon sources like ^{137}Ce, ^{22}Na, and ^{57}Co. Results indicated that this is relatively a very linear scintillator with non-proportionality of about 5%. Although $LaBr_3$ has a better energy resolution, for low activity measurements, it is always recommended to materials with low intrinsic activity. Keeping that in mind it has been observed that $CeBr_3$ has almost an order of magnitude lower background count rate compared to $LaBr_3$ (Fig. 14d).

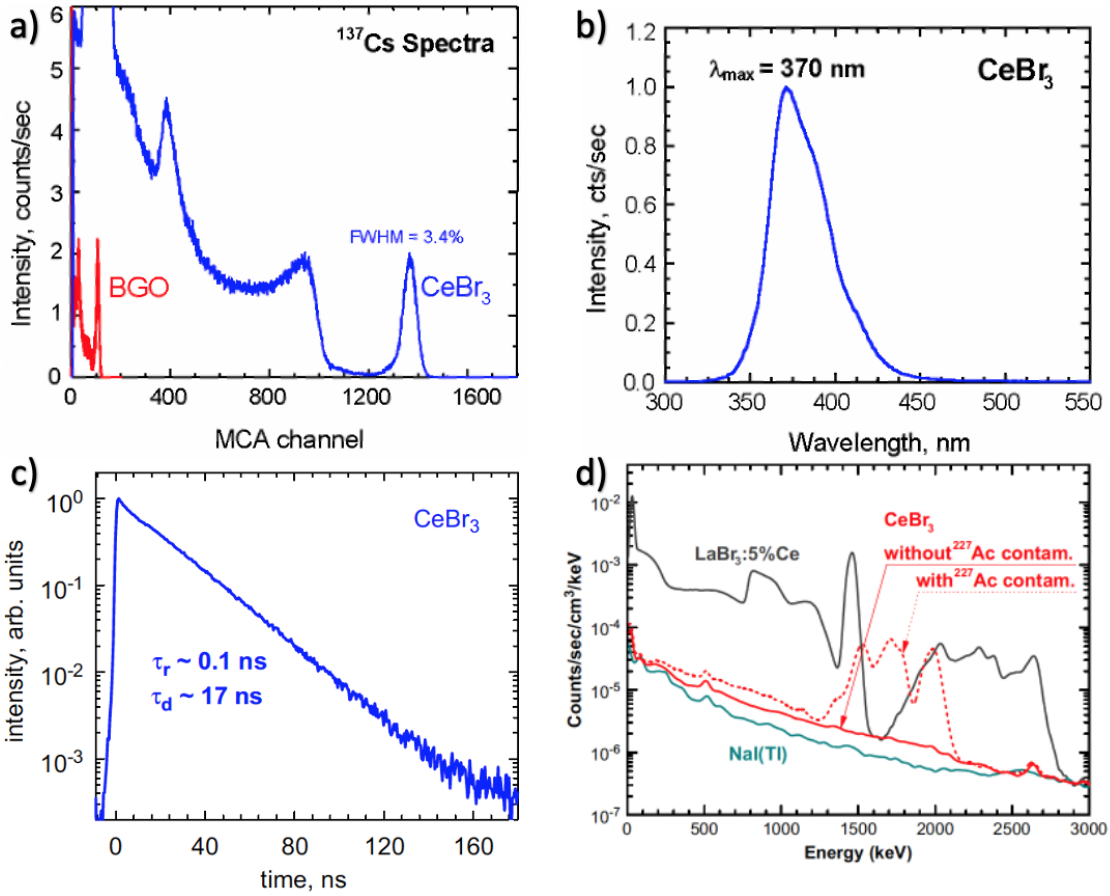

Fig. 14. a) $CeBr_3$ and BGO spectra using ^{137}Cs; b) the emission spectra of $CeBr_3$; c) Decay time of the $CeBr_3$ scintillator; d) Intrinsic activity spectrum of $LaBr_3$:5% Ce, NaI(Tl), and $CeBr_3$ with and without ^{227}Ac contamination

Some of the particular advantages of using $CeBr_3$ include its impressive light yield and energy resolution. It must be brought to the reader's attention that decay time also plays a very crucial role in deciding a scintillator for a particular application. From the

radioxenon detection standpoint, we are required to ensure that there is a minimum coincidence time window between the electron and photon detection media. This is to ensure minimum coincidences between stray events and electron/ photon interactions from the detectors. The decay time of $CeBr_3$ is also a point of significant interest. Not only does it help in reducing background counts but also ensures that the pulse returns to baseline quickly so that saturation doesn't occur even in high-count rate situations. The relatively high effective Z number and density also ensures that the full energy peak efficiency is high.

Talking about the downsides, $CeBr_3$ is a hygroscopic scintillation material, which means this crystal has a high affinity for moisture. Therefore, this crystal needs to be hermetically sealed to ensure no moisture comes in contact with the crystal. This means that the SiPMs are also required to be attached directly to the crystal. These requirements present us with a unique design where the SiPMs are permanently mounted to the crystal with pins protruding out to enable cathode biasing and signal readout. From previous experience, it was realized that SiPMs also are required to be covered from the bottom because some photons can penetrate the SiPM from the underside and cause interactions in the active area of the photon sensing medium. Therefore, for this work, it was decided to backfill the SiPMs with epoxy. This accomplishes two goals, ensure that the integrity of the hermetic seal is maintained at the SiPM edges and guarantee that no optical photons can interact with the SiPMs apart from the ones originating from the scintillator.

2.2.7 Strontium Iodide – Photon Detector

Strontium iodide is a scintillation crystal that is commonly used in the high-resolution spectroscopy community. Although discovered in the 1960s, this scintillator came to be widely known as a viable alternative much recently after extensive work done at Lawrence Livermore National Laboratory (LLNL) [112-120]. This scintillator is one of the brightest with about 85,000 photons per MeV (about twice as bright compared to conventional NaI detectors). The increase in the brightness also has a direct effect on the energy resolution of the scintillator, this scintillator boasts of an energy

resolution between 2-3 percent FWHM for the 662 keV peak which is about twice as better compared to the traditional NaI detector. The Eu^{2+} doping percentage seems to play a crucial role in the brightness of the scintillator, at about 5% doping this scintillator releases a maximum number of optical photons per MeV. In terms of optical photon proportionality, SrI_2(Eu) maintains a proportionality within 2% within the energy range and temperature range in which the detector is generally expected to operate in a lab environment [between 20-30°C] (Fig. 15a). The relative photopeak shift of under 20% has been reported over a temperature range of 20°C to 60°C (Fig. 15b). There have also been some changes observed in the energy resolution as a function of temperature, FWHMs between 2.5% and 3.4% have been reported for temperatures between -30°C and 50°C. In terms of decay time, this scintillator has a decay time between 1 and 5 μs. This is because of overlap in the absorption and emission spectra of the scintillator (Fig. 15c). In other words, the scintillator is not transparent to all the optical photons produced by the scintillator. This relatively long decay time doesn't allow this scintillator to be used in high count rate measurement situations. In the case of radioxenon measurements, since the activities encountered in the field are not very high, SrI_2(Eu) is expected to be successfully used for detecting photons. Another significant advantage of the scintillator is its low intrinsic background when compared to other high-resolution scintillators like $LaBr_3$. There are solid-state detectors like CZT which feature an even better energy resolution of below 2% and higher density but significant challenges with regards to production in large sizes, cost, and the slow electron drift time limit the application of these materials in novel designs.

The use of strontium iodide comes with its own set of challenges and limitations. SrI_2(Eu) is a hygroscopic scintillator, which means this material has an affinity to absorb moisture from the surrounding air which can prove detrimental to the scintillator performance. Therefore, it was required to encapsulate the entire scintillator. There are two practical options for light readout at this point, either permanently mount the SiPMs on the scintillator or place an optical window from which light is read using external SiPMs. It was decided to permanently mount the SiPMs to reduce the overall size of the detector. Most scintillators used in radioxenon detection systems employ

NaI-based photon detectors which are also sensitive to moisture uptake, therefore the problem of using a hygroscopic crystal is not something new but is worth mentioning. $SrI_2(Eu)$ does exhibit substantial absorption and reemission which results in a long decay time. Although the number of photons released in the energy deposition is the same, the pulse amplitudes are relatively small because of the long decay time. This also introduces the problem of trigger walking. This is a scenario where high energy pulses trigger sooner compared to low energy pulses although the threshold is maintained the same.

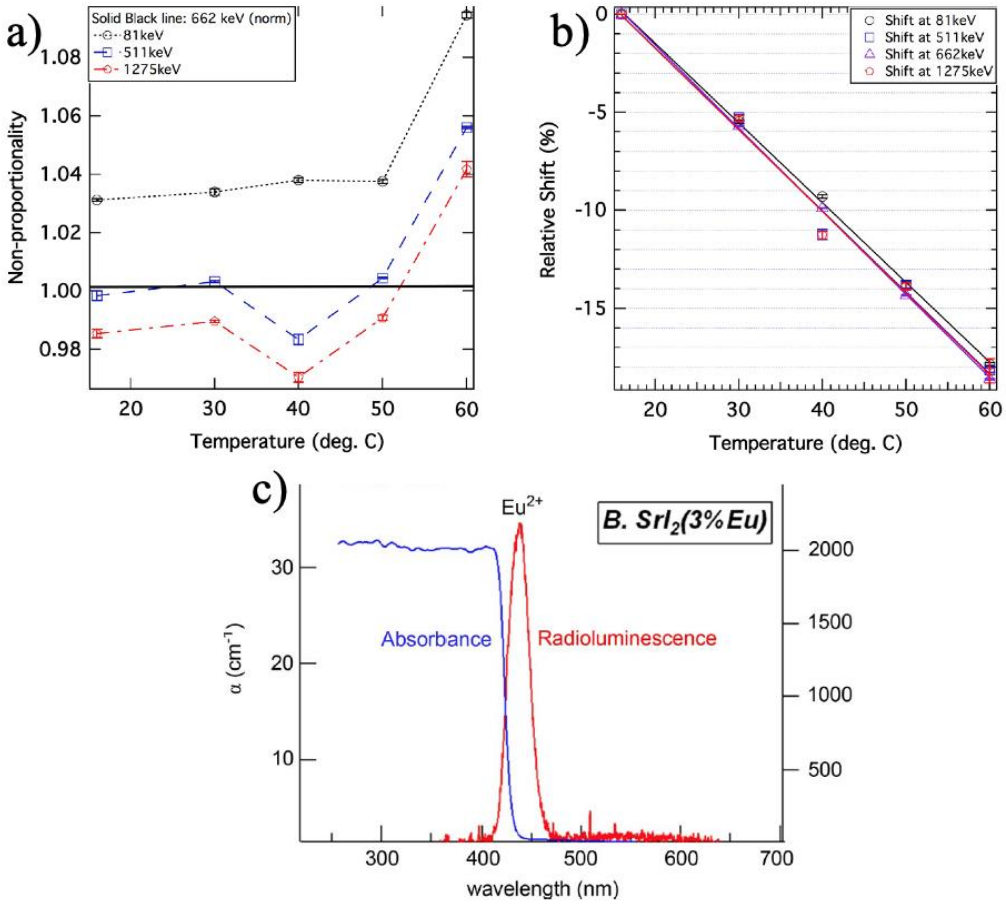

Fig. 15. a) the non-linearity of $SrI_2(Eu)$ as a function of temperature for various energies; b) the relative shift of the peaks as a function of temperature; c) the absorption and emission spectrum of $SrI_2(Eu)$ doped with 3% Eu. NOTE: The significant overlap between the absorption and emission spectra

2.2.8 Silicon Photomultipliers (SiPMs)

Silicon photomultipliers are one of the devices used in radiation detection to detect optical photons from a scintillator. When a radiation photon deposits its energy in the scintillator, optical photons are generated, but these photons can't be directly used to estimate the amount of energy deposited in the scintillator. To sense optical photons, initially photomultiplier tubes (PMTs) were put into use. These are basically vacuum tubes consisting of multiple dynodes (locations of charge multiplication). When optical photons interact with the photocathode at the entrance of the PMT, electrons are created. A differential voltage is applied across each dynode to accelerate the electrons to enable the release of even more electrons from the next dynode. This process continues for about 10 stages before reading the signal from the anode. This conventional process has a couple of drawbacks which are listed below:

- PMTs require high voltage to operate (~750 to 1000V)
- The form factor of PMTs is relatively huge.
- Susceptible to electric and magnetic fields.

Therefore, to remedy some of these shortcomings, silicon photomultipliers were introduced. These are basically semiconductor photon detectors operating in reverse bias past the proportional region but not high enough to damage the sensor. When a photon interacts with the detector, an electron-hole pair is created. This electron is accelerated because of the potential difference and in the process creates more electrons. In that sense, this system operates similar to a Geiger Muller tube where a single ionization is sufficient to create an avalanche. In a typical SiPM, thousands of these tiny cells are combined to detect photons from a scintillator. Each of these cells fire individually and a combined result is representative of the number of photons that have impinged in the SiPM surface from the scintillator. Although SiPMs have many advantages as discussed earlier, these devices have shortcomings of their own. Most notably, SiPMs gain is temperature-dependent which means that with temperature the overvoltage that is required to be maintained above the breakdown voltage changes. At higher temperatures, to obtain the same gain we are required to apply higher voltages. Although SiPMs offer the luxury of independent and modular light collection devices,

when large surfaces are required to be covered, the parallel connectivity tends to increase the capacitance of the circuit which is detrimental for spectroscopy purposes. Another important factor is PMTs have no components (capacitors) that actively change the shape of the pulse, therefore the output from a PMT is more representative of the actual scintillator properties (decay time), while the same can't be said about SiPMs. Graphical representation of the avalanche photo-multiplication in a photodiode is shown in Fig. 16 [121]. A SiPM layout showing multiple avalanche photodiodes (microcells) connected in parallel and the cross-section view of the SiPM are shown in Fig. 17a and Fig. 17b respectively [122, 123].

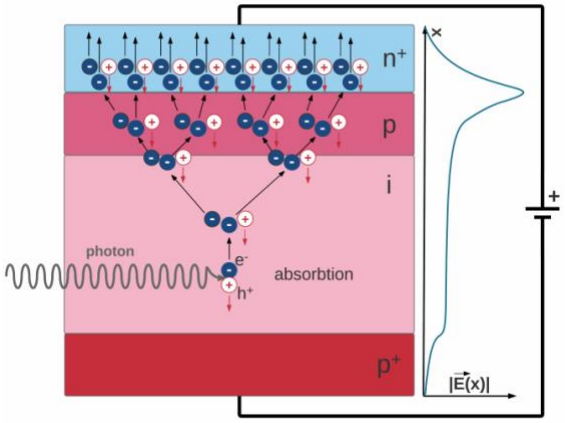

Fig. 16. Avalanche process depicted in a photon detector

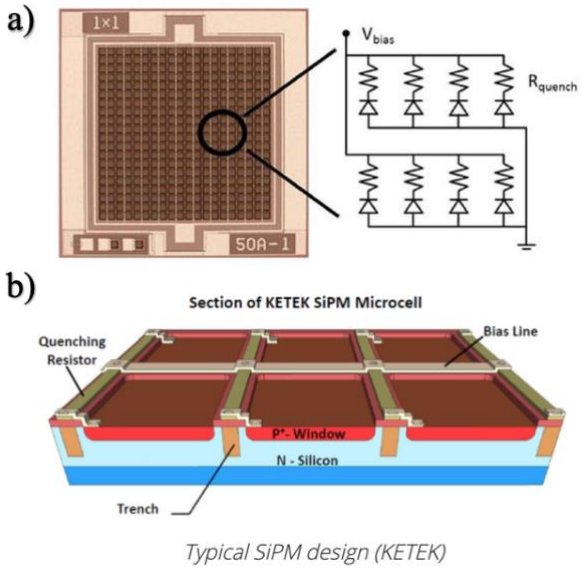

Fig. 17. a) A SiPM showing the microcells connected in parallel; b) cross section view of a SiPM

2.2.9 Field Programmable Gate Arrays (FPGAs)

Field-Programmable Gate Arrays or FPGAs are digital logic blocks that can be used for several different functionalities. In their most basic form, FPGAs are semiconductor devices consisting of a number of configurable logic blocks (CLBs) that can be programmed by the user to perform a particular task [124, 125]. Unlike Application Specific Integrated Circuits (ASICs), FPGAs can be used for many functions. While designing an ASIC, the end goal or application is fixed hence the name, application specific. In other words, an ASIC can perform only a specific task, on the other hand, using an FPGA, the programmer has the independence to use it for several applications, like designing an adder, using the memory blocks for data storage, performing convolution operations, etc.

These devices can be programmed using Hardware Description Languages like Verilog and Very High-Speed Integrated Circuit Hardware Description Language (VHSIC-HDL) commonly called VHDL. Powering off an FPGA will erase all the configurations previously made by the user. Manufactures of these devices have provided options to control the FPGA using commonly used programming languages like Python and MATLAB (Application Programming Interfaces: API). FPGAs communicate with the PC via input/output (I/O) pins. Fig. 18 shows an example of a connection between different logic blocks in an FPGA [126].

Often FPGAs are confused with microcontrollers, although they might end up performing the same function, there are a couple of fundamental differences between the two. Microcontrollers follow a concept of sequential processing, which is similar to most of our programming languages where a set code is compiled and executed line by line. While on the other hand, FPGAs follow a concept of parallel programming, this is because the programming in the case of an FPGA happens at a fundamental hardware level. These devices are well suited for applications where multiple signals are required to be processed simultaneously for example reading data from more than two channels of a detection system and identifying coincidence events.

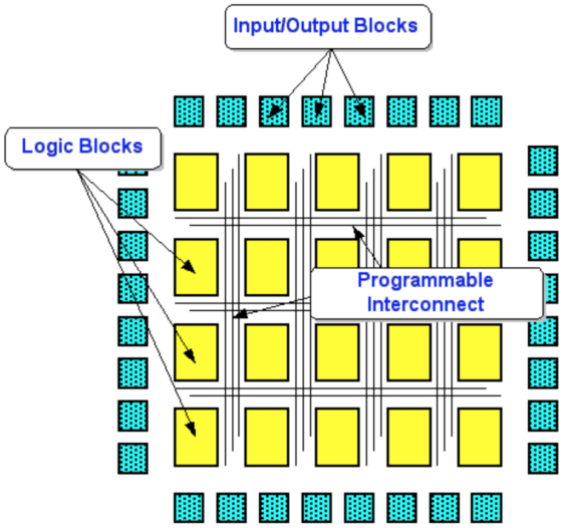

Fig. 18. The CLBs inside an FPGA showing programmable logic between the logic blocks

2.3 MDC Calculations, Pulse Processing, and Photon Transport

In this section, we shall briefly be going over the MDC calculations, the pulse processing techniques/ options, and the basics of the Geant4 optical transport code.

2.3.1 Minimum Detectable Concentration (MDC) and Regions of Interest (ROI)

This sub-section covers the concept of regions of interest and the MDC calculations. These are some of the methods used to quantify the performance of a detection system.

2.3.1.1 Region of Interest (ROI)

When a radioxenon sample is injected into the detector and coincidence counting technique is implemented to detect events from radioxenon, the best option available for plotting the data from the detector is a 2-D heatmap of the various radioxenon signatures. Some regions will be densely populated where there are a greater number of counts and other locations on the plot will be relatively sparsely populated or not at all. For quantitative purposes, only the regions which are densely populated are taken into accounts because these are the regions representative of radioxenon decay. The Region (Energy^2) which shall be considered for this calculation depends on the

resolution of the detector and the type of radiation. For example, if we consider a detector with poor energy resolution, chances are the counts are going to be spread out in a wide range compared to a high-resolution detector where counts are constrained in a narrow region. The ROI for mono-energetic conversion electrons or photons is generally taken to be a fixed multiple of the FWHM (generally twice). As for the beta spectra, the ROI ranges from 0 to β_{max}. Therefore, using high-resolution detection media is in our best interest because that would mean defining a smaller ROI. A smaller ROI directly results in a fewer number of counts featuring inside the ROI, this helps in improving the MDC of the system. Fig. 19 shows the Regions of interest identified for the ARSA detection system from one of the measurements. The electron energies are shown on the x-axis while the photon energies are shown on the y-axis [127].

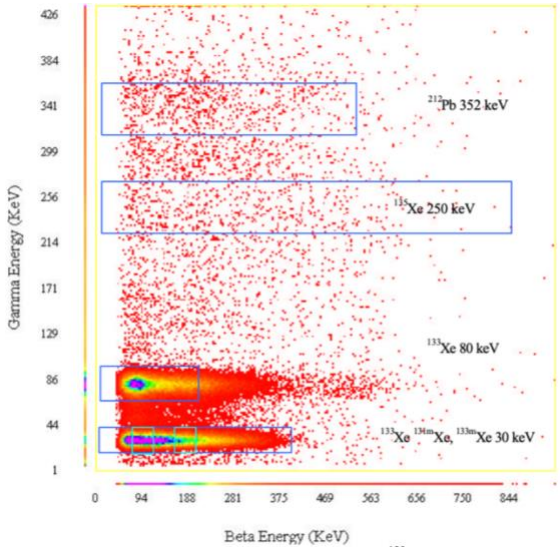

Fig. 19. The regions of interest for the ARSA detector from one of the measurements during the field tests at the Insitut fur Atmosphraische Radiaktivitat (IAR)

2.3.1.2 Minimum Detectable Concentration (MDC)

Several radioxenon detectors have been developed by many groups across the world. Most of these detectors have successfully been able to identify all the signatures from the radioxenon of interest, photon energies at 31, 81, and 250 keV, conversion electrons (45, 129, and 199 keV), and the 346, 910 keV beta spectra. The Minimum Detectable Concentration (MDC) is the measure of how low a detection system can measure

accurately. The lower this number, the more sensitive the detection system is. The CTBTO requires all the detectors deployed on the IMS network to achieve an MDC of at least 1 mBq/m^3 for ^{133}Xe. In recent times it has become common practice for all the radioxenon isotopes to have an MDC below 1mBq/m^3. Detectors like the SAUNA III and Xenon International have proposed even lower MDC values. The general MDC equation takes into account the detection efficiencies, branching ratios, counts in the ROI, half-lives, and the gas processing times to arrive at the MDC value for each radioxenon isotope. The general MDC equation used is presented in eq (2) [128, 129]:

$$MDC\left(\frac{mBq}{m^3 air}\right) = \left[\frac{2.71 + 4.65\sigma_0}{\varepsilon_\beta \varepsilon_\gamma \beta_{BR} \gamma_{BR}}\right]\left[\frac{\lambda^2}{(1 - exp(-\lambda T_c))(-\lambda T_p)(1 - exp(-\lambda T_A))}\right]\left[\frac{T_C * 1000}{V_{air}}\right] \quad (2)$$

Where:

$$\sigma_0 = \sqrt{BckCnt_{total} + \sigma^2_{BckCnt} + InterferenceCnt + \sigma^2_{InterferenceCnt} + MemoryCnt + \sigma^2_{MemoryCnt}} \quad (3)$$

ε_β : Efficiency for detection of β
ε_γ : Efficiency for detection of γ
β_{BR} : Branching ratio of β
γ_{BR} : Branching ratio of γ
λ : Decay constant of isotope of interest [s^{-1}]
T_c : Collection time of xenon sample [s]
T_p : Processing time of gas [s]
T_a: Counts acquisition time [s]
V_{air} : Collected air volume [m^3]

And

$BckCnt_{total}$: summation of the total number of background counts observed in the region of interest.
$InterferenceCnt$: Counts due to interferences from radon daughters and overlapping ~30 keV regions of interest.
$MemoryCnt$: Counts due to memory effect in the gas cell.

Generally speaking, the MDC is divided into three parts: radio physical part dealing with the branching ratios and detector efficiencies, the gas processing part, which is

responsible for the collection, gas processing/ counting times, and the volumetric term which tells us the volume of air that was sampled.

In the past few years, extensive efforts have been put into improving the MDC of the detectors and increasing the frequency of counting xenon samples in quick succession, prominent examples of this include the Xenon International and SAUNA III systems. While calculating the MDC for a detection system it is important to mention the gas processing parameters being used if the detector doesn't have a dedicated gas processing unit.

The following paragraph explores the situation where there are two unique decay paths for a radioxenon of interest. ^{133}Xe emits an 81 keV in coincidence with a 346 keV beta and a 45 keV conversion electron in coincidence with a 31 keV X-ray and a 346 keV beta particle. Therefore, it is necessary to account for both the decay paths while coming up with an MDC value for ^{133}Xe. A weighted average of both the decay paths is shown in eq (4):

$$MDC_{133_{Xe}}\left(\frac{mBq}{m^3\ air}\right) = \sqrt{\frac{1}{\left(MDC_{133_{Xe}}^{81\ keV}\right)^{-2}+\left(MDC_{133_{Xe}}^{30\ keV}\right)^{-2}}} \quad (4)$$

In this work, the gas processing parameters of the ARSA and Xenon International are intended to be used. In the σ_0 term, there are three components, counts because of memory effect, counts from interference, and counts that fall into the ROI from background events. A couple of simplifications are made in the way this equation is put to use (Eq. 2). Since the gas sample used in this work is not collected from the atmosphere, but rather ultra-pure xenon samples, there are no other radionuclides present apart from xenon, therefore it is safe to assume that the interference counts in this case shall be zero. This work proposes the use of a stilbene gas cell, this material is known for its low memory effect, and to ensure that there is no residual xenon in the gas cell, it is decided to allow a large amount of time to pass by before conducting the 48-hour background measurement (T_b). Therefore, using these assumptions discussed above, the simplified equation of σ_0 is shown in eq. 5.

$$\sigma_0 = \sqrt{\frac{T_a}{T_b} BckCnt_{total} + \sigma^2_{BckCnt}} \quad (5)$$

2.3.2 Signal Processing

Processing the signal coming from the detection system is of utmost importance to identify the presence of radiation in any environment. These signals are either released in the form of a current (semiconductor detectors) or optical photon (scintillators). These stimuli are subsequently converted into a current signal by either PMTs or SiPMs. These current signals are then converted into voltage signals for either spectroscopy or counting purposes. Therefore, it is important to understand some of the techniques and methods used in the field of radiation detection. We shall be going over various filters and their functions in understanding their application in radiation detection.

2.3.2.1 Digital Signal Processing

In the past few decades many researchers have moved away from using bulky analog electronics and shapers for determining the amplitude of the peak. They have instead resorted to using digital pulse processing techniques for amplitude identification and histogram plotting. For the implementation of these techniques, the first requirement is the sampling of the analog signal which is performed by the analog to digital converter, most commonly referred to as an ADC. To implement these techniques, we are required to have a digitized signal and a filter, the operation performed is known as a convolution. Mathematically this operation is expressed in eq. 6. Where y[a] is the sample-by-sample filter response, h[k] are the filter coefficients, and x[] are the individual samples of the input function.

$$\text{y[a]} = \sum_{k=0}^{N} h[k] * x[a-k] \quad (6)$$

Intuitively thinking, the convolution operation is a process of sliding the filter with a set number of coefficients over the digitized pulse and observing the filter response

generated by a signal. These operations can be used to smoothen a signal to identify a pulse in-between noise, capture the amplitude of a charge integrated pulse, or identify if a pulse has a threshold greater than a preset amplitude. We shall be going over each of these operations in some detail in the following paragraphs. Fig. 20 shows an example of the implementation of the convolution operation to a data stream [126].

When working with real-world signals, it is often observed that the signal is buried in the noise signal, under such situations it is often required to smoothen the signal to observe a meaningful pulse. The first type of filter in the radiation detection world is called the moving average filter. As the name suggests, this filter averages a set number of signal elements and outputs an averaged value. Care must be taken while implementing this filter and ensuring that the final convoluted filter output for each coefficient is divided by the number of filter elements used. In the second type of filter called the triangular filter, out of a total of N given coefficients, there are N/2 number of positive coefficients (+1) and N/2 number of negative coefficients (-1), the order is decided based on the polarity of the pulse. When there is an ideal baseline at any value, the output of the filter shall always read zero, because it is adding and subtracting a virtually constant baseline. The output however changes when an actual pulse arrives. Triangular filters are excellent for trigger detection, the rising edge of the pulse is integrated while the trailing edge of the filter is still accounting for the baseline. This gives rise to a sharp rise as soon as the pulse is encountered. The third kind of filter we shall be discussing is the trapezoidal filter, this is a special case of triangular filter, where a flat top is introduced with a coefficient value equal to 0. These kinds of filters can be effectively used while just sampling the amplitude of the pulse. On the application front, radiation detectors generally use a charge sensitive preamplifier (CSP) to integrate the charge of the pulse on a capacitor and discharge it in a set time over the resistor [130, 131]. Under such cases, the energy deposition of the pulse is represented by the peak of the voltage signal. Trapezoidal filters can be effectively put to use to sample this peak energy by using a flat-top time equal to the rising edge of the pulse from the CSP.

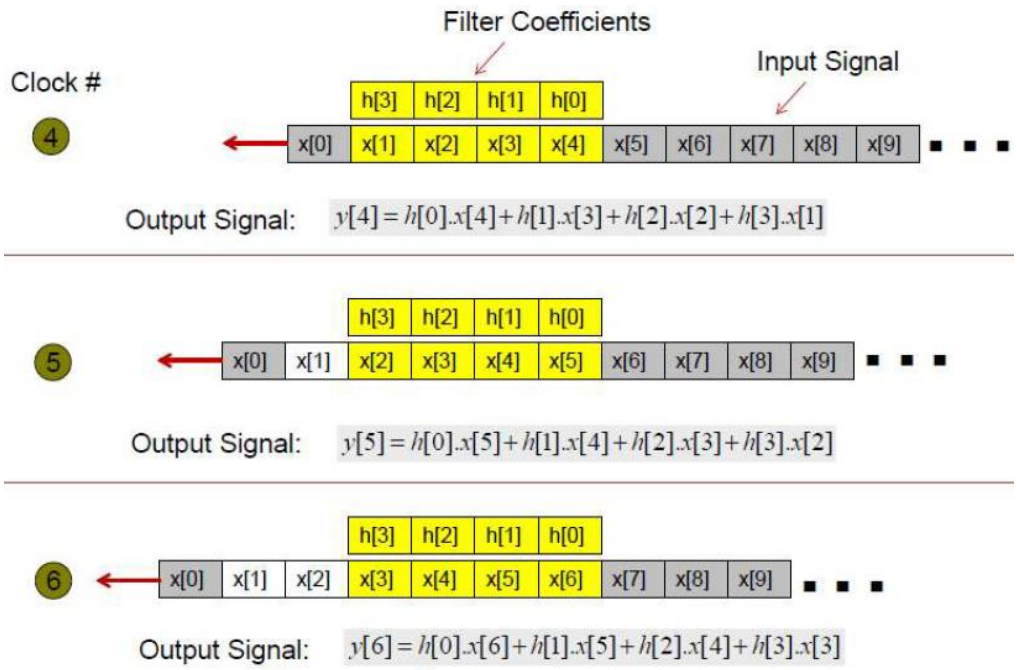

Fig. 20. Convolution operation performed on a data set using a filter

2.3.2.2 Coincidence Identification

In this work, an 8-channel digital pulse processor will be used for coincidence identification. There are two methods of coincidence identification, either this can be performed using list mode operation or coincidence identification. In list mode identification, all the pulses are recorded along with the timestamps. Post-processing scripts are then run to identify the coincidence events. As it can be imagined, this is a data and algorithm intensive process that requires extensive post-processing. The other option is to identify coincidence events in real-time using hardware (FPGA). In this work, a Xilinx Kintex-7 FPGA is used to identify the coincidence events between the three channels of the detector [132]. A coincidence timing window is set by the user, which means the electron and the photon channels are required to trigger within the set time of each other for the counts to be valid. Once a coincidence event is identified the pulse data is transferred to the PC MATLAB user interface via the USB port. Alternatively, the data can also be processed in the FPGA and only the histogram can be displayed on the PC but that would mean, no actual pulse data would be available

to the user. This data might prove to be important for optimizing the filter parameters at a later stage.

2.3.3 Optical Photon Transport Simulations

When radiation interacts with a scintillator material, several photons are generated based on the scintillation yield and the energy of the ionizing radiation. These optical photons are generally propagated in an isotropic fashion. In the case of photons, the photon deposits its energy to an orbital electron and the electron goes on to elevate other electrons from the valence band to the conduction band and in the process of de-excitation, ends up releasing optical photons. A couple of decades ago, most applications used PMTs for photon detection. Generally, scintillators were grown to match the active area of the PMT so that the photons impinging on the entire detection area would be sensed by the photon detection media.

With the development of new optical photon detection devices like SiPMs, researchers have been provided with more freedom. This newfound freedom has enabled researchers to explore a variety of SiPM mountings. It is worth mentioning that in cases of large detection areas, it is not economically feasible to cover the entire detection surface. From a technical standpoint, even if the entire area was covered, SiPMs are connected in parallel, which means, with every SiPM connected in parallel, the capacitance linearly adds up. This ultimately leads to a small voltage signal because the charge released by the impinging photons on the SiPM is constant while the capacitance increases. Therefore, in recent years, efforts have been put into positioning the SiPMs at optimum locations. This requires the researchers to have knowledge about photon transport inside the scintillator and reflector materials that are required to be used. In this section, we shall be going over the background of optical photon transport tools and some of the work that has been done. We shall be focused on Detect2000 and Geant4, their input decks, and some differences in functioning.

2.3.3.1 DETECT2000

DETECT2000 is purely a photon transport code. This is a C++ based code that was used extensively in the early and late 1990s before the prominence of Geant4 [133]. In DETECT2000, the user first defines the geometry that is required to be simulated. Geometries are either defined as planes, cylinders, or points, once the geometry is defined, surface attributes are assigned to the surfaces like the surface finish, reflectivity, etc. Bulk properties like refractive index, absorption mean free path, and scattering mean free path are then defined. These parameters are used in determining the scattering or absorption of photons. Once all the geometries are defined, we enter the optical photon generation regime where the user is required to provide a region where photons can be generated. This is where the total number of runs and the random seed is initiated. Options like the lifetime of the photon can also be fed as input. The lifetime of a photon determines how long each photon is run. In case a photon is not absorbed, scattered, or escapes the system after the user set time, the history is terminated. DETECT2000 also generates a time-of-flight histogram after each run if requested by the user. This helps in providing rough estimates for the time it takes for photons to be terminated. Similar to the PTRAC card in MCNP, DETECT2000 also provides an option for tracking each photon. In this mode, the fate of the photon (counted, escaped, bulk absorbed, surface absorbed, timed out, or transmitted), wavelength, surface count and the final coordinates can be determined. This data is extremely useful in generating surface heatmaps of the optical photon distribution. An example of a simple DETECT2000 code describing a 3-body deck is shown in Fig. 21.

```
DMAT1,2.15N,200AD,200SD
DMAT2,1.5N

DFIN1,DETECT
DFIN2,POLISH

DPLN1,0Z
DPLN2,10Z
DCYL1,10R
DPT1,15Z
DPT2,10Z
DPT3,10Z,5X
DCONE1,PT1,PT2,PT3

COMP1,MAT2
SURF,FIN1,PLN1,ZL
SURF,FIN2,CYL1,RS
SURF,FIN2,CONE1,RS
SURF,FIN2,PLN2,ZS,C2

DCYL2,5R
DPLN3,20Z

COMP2,MAT1
SURF,FIN2,PLN2,ZL,C1
SURF,FIN2,CYL2,RS
SURF,PLN3,ZS,C3
DPT4,20Z
DSPH1,PT4,5R

COMP3,MAT1
SURF,FIN2,SPH1,RS
SURF,PLN3,ZL,C2

GEN,MAT1,10ZS,25ZL,-5XS,5XL,-5YS,5YL
LIFE1000

HIST,STEP0.1,30STEPS
FATES1
SEED 19
RUN500

END
```

Fig. 21. An example of a DETECT2000 input deck

Additional features like surface connections are also available in DETECT2000, where the user is being provided the option to perform a surface mate between two objects that are in contact with each other. In this tool, an option to provide sampling decks for the refractive index, absorption/ scattering mean free paths and other optical parameters of the scintillator as a function of wavelength are also available.

Although this is easy to use a quick tool, there are several drawbacks of using DETECT2000. In the current world, many new surface models are being used. More recently models have been developed for specific reflectors and surface finish conditions where data has been recorded for each incident angle. These models are widely accepted to be more accurate than the traditional reflection models that are being used. The second disadvantage of using DETECT2000 is that it does not represent the true behaviors of the scintillator. It is not hard to imagine that the interaction of ionizing photons in a scintillator is very much dependent on the cross-section of the detection medium at a given energy. In DETECT2000, optical photons are randomly generated inside the volume defined by the user, this simplification works great when we are dealing with high energy photons. However, this method does not efficiently work if charged particles are involved rather than photons. Some notable advantages of this tool are its ease of operation and user-friendly nature.

2.3.3.2 Geant4

Geometry **an**d **T**racking 4, more commonly known as Geant4 is a tool kit developed by the Conseil Européen pour la Recherche Nucléaire (CERN) for the passage of particles through matter [134-137]. This is an open-source C++ based software that can be efficiently used for several applications including medical imaging, high energy physics or space equipment application. In this work, we shall be using Geant4 to design the detection geometry and use the general particle source (GPS) option in the macro files to realize a cylindrical source that is emitting photons. These ionizing radiations interact with the scintillation crystal and produce optical photons that are transported through the volume.

There are two major models used for optical photon reflection: Glisur and Unified. In the Glisur model, it is assumed that a surface is made up of multiple microfacets. Each time a photon interacts with a surface, a micro-facet is selected from a distribution, and based on the microfacet selected, the photon is reflected. The second type of reflection is based on the unified model. In the unified model of reflection, when a photon interacts with a surface, four types of interactions are possible: specular spike, specular

lobe, backscatter, and diffused reflection. Fig. 22 shows the various types of reflection in a unified model [138].

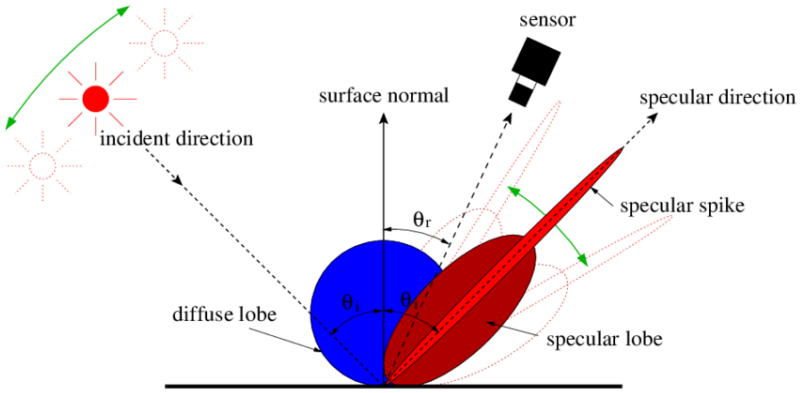

Fig. 22. Reflection mechanisms in the unified model

It is worth mentioning that the probabilities of the four types of reflections must add to unity and in the Geant4 framework, these factors are independent of the incident angle of the photon. However, in reality, it has been observed that these probabilities change with the angle of the incidence photon. The unified model of reflection is the same algorithm that is used in the DETECT2000 toolkit. However, it must also be pointed that the default reflection model in Geant4 is the Glisur model of reflection.

The second parameter of importance is the type of reflector. Dielectric-dielectric and dielectric-metal are the two options available to users. In the case of a dielectric-metal surface, the photons are reflected based on the reflectivity set by the user. The photons that are not reflected are absorbed by the surface. Therefore, in its basic usage, this interface is best suited for a photon absorber or a perfect reflector. The next type of reflector is a dielectric-dielectric surface. The photons can undergo total internal reflection, refraction/reflection based on the angle of incidence, refractive index, and the wavelength of the photon. The major governing factor in this type of surface is the refractive index of the medium the photon is exiting and the refractive index of the medium the photon is entering. In this work, the SiPMs which act as optical photon black-holes use a dielectric-dielectric surface type with a minimal absorption length for the photons in the SiPMs; this essentially terminates the photons as soon as they enter

the SiPMs. In the stepping action section of the code, if it is observed that the photon has entered the SiPMs and it has been absorbed (terminated), the x, y, and z-axis positions of this terminated photon are recorded. Geant4 outputs this coordinate data as a text file which is then read by a MATLAB file to extract the positions along the SiPM plane and plot the data on a heatmap.

The third parameter is the surface finish of the reflector. Broadly speaking there are two types of surface finishes: polished and ground. A polished surface between two bodies is when there is perfect specular reflection. In such cases, the angle of incidence and angle of reflection is almost the same. It has been observed that when such surfaces are employed in the capacity of a reflector, there is a uniform distribution of optical photons on the detection surface. The second type of surface finish is ground, this is the case when diffused reflection dominates. When such reflectors are used there are preferential optical photon hotspots near the surface of the reflector.

The literature review has revealed that the reflection models incorporated in Geant4 are not always accurate and evidence has been provided by various groups where experimental vs simulation data has yielded different results. Therefore, the new releases of Geant4 have provided the users with an option of using reflection coefficients based on experimental data. For this work, it was decided to use data from the DAVIS Look Up Table (DAVIS LUT). These experiments were carried out using LYSO crystal with various surface finishes and reflector combinations. Although these results are not based on the crystal used in this work, it was decided to use the DAVIS model since it’s based on experimental results rather than theoretical models.

2.4 Previous Radioxenon Detection Systems and Concepts

Since the late 1990s, several radioxenon detection systems have been built and tested under a variety of conditions. In any radioxenon system, there are mainly two units, the gas processing unit, and the radiation detection unit. We shall be briefly going over the gas processing units to understand their functionality and then explore in depth the various xenon detection systems that have been built and tested by a number of research groups around the world.

2.4.1 Gas Processing Units

The gas processing section is also divided into two subsystems, the gas collection system, and the gas purification system. Although, this section is not a focus for this work we shall be going over the general process of gas purification and concentration. The gas that is sampled is initially required to be deprived of carbon dioxide and water vapor. The next step of the process is to trap radon gas. It must be noted that radon is also a noble gas and effectively separating these two noble gasses is a challenge that is faced in the radioxenon community. These traps are small in size to ensure that only radon is trapped, and xenon gas is effectively passed on to the next stage. This is followed by absorbing the remainder of the gas in activated charcoal at about -100°C. This is followed by the xenon purification process explained in the next section.

This is then followed by purging the xenon gas that is trapped inside the charcoal. For this process, the charcoal is heated to 300°C and purged along with nitrogen. A number of redundant traps are used to ensure that the maximum amount of xenon gas has been removed from the charcoal. Several molecular sieves are then used to trap any additional radon that was not trapped during the pre-trap process. The gas is then passed through additional moisture and carbon dioxide traps. Finally, the gas is again absorbed in charcoal (smaller dimensions) and transferred to the gas cell scintillation counter where the charcoal is heated to about 350°C before being counted by the detectors. It must be pointed out that a carrier gas such as nitrogen or helium is used to transport the gas to the gas cell for counting. Fig. 23 shows the simplified schematic used in the ARSA detection system [139].

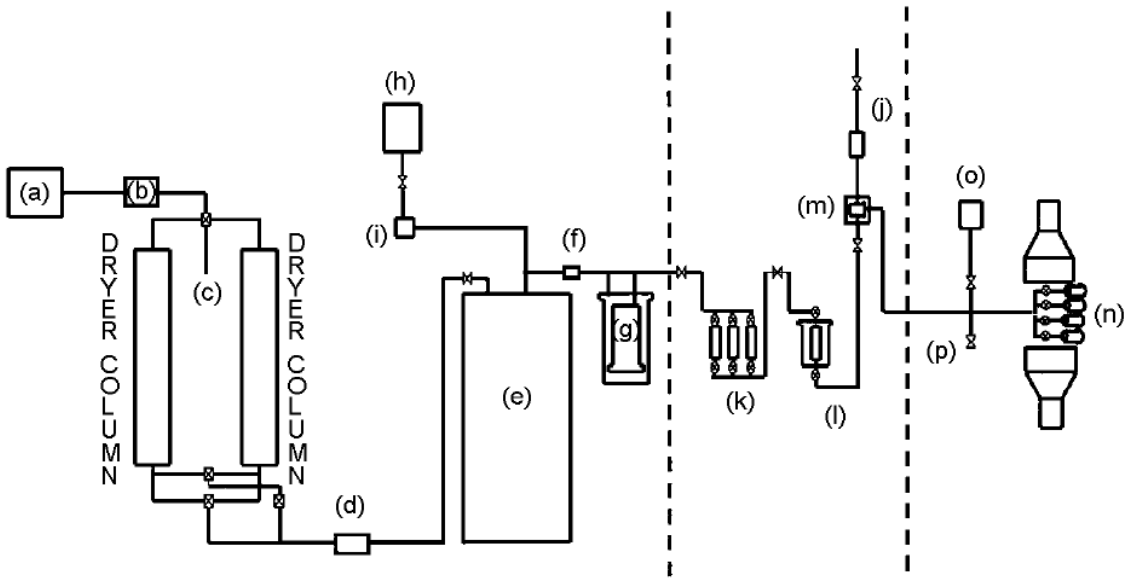

Fig. 23. Schematic of the ARSA gas purification system showing the compressor (a), heat-exchanger (b), air/CO_2 removal columns, charcoal trap (h), final charcoal trap (m), the detection system (n), and the path to the archived bottles (p)

In the 2000s much of the research efforts were focused on improving the shortcomings of the first generation radioxenon detection systems. The flowing years, till the mid-2010s significant efforts have been put into improving the efficiency of the gas processing systems. In the past five years research groups have again diverted their attention towards developing new radioxenon detection systems to improve efficiency and resolution.

2.4.2 Radioxenon Detection Systems

This section provides an extensive review of the radioxenon detection system developed by various scientific groups. These systems include the first generation of radioxenon detectors like the American Automatic Radioxenon sampler/analyzer (ARSA), the Swedish Automatic Unit for Noble gas Acquisition (SAUNA), the Russian Automatic Radioanalyzer for Isotopic Xenon (ARIX), and the French Système de Prélèvement Automatique en Ligne Avec l'Analyse du Xénon (SPALAX™). The next section covers prototype detection systems that have been developed by other groups like the 24-element Si PIN diode detector, and the Mobile Analyzer of Radioactive Gases OuTflows (MARGOT) [140-142]. This is followed by a section on

detectors that were developed at Oregon State University like the Two Element CZT Detection system (TECZT), PIPS-CZT system, the CZT crystal, an Array of SiPMs, and a Plastic scintillator (CASP), and the Stilbene-CZT system. These systems can also be divided according to the technology employed. Some detectors use purely scintillators or semiconductor detectors while other detectors use a mix of scintillators and semiconductors for electron and photon detection.

2.4.2.1 Automatic Radioxenon Sampler/Analyzer (ARSA)

The ARSA detection system was designed and developed by the Pacific Northwest National Laboratory (PNNL). This system employs a coincidence-based detection system for radioxenon measurement. For photon detection, two NaI detectors are employed, and electrons are detected using plastic scintillators. The plastic scintillators in the detector also act in the capacity of a gas cell. Each NaI detector measures about 10.16 x 17.78 x 3.81 cm^3. Four holes each measuring 3.175 cm in diameter are machined in the NaI to accommodate the plastic scintillators. These scintillators are read by two PMTs each. As mentioned previously, this detection system uses activated charcoal for trapping and concentrating the xenon gas from the atmosphere. Fig. 24 shows the cross-section of the first ARSA detection system that was developed. The system was successful in achieving the MDC requirements set forth by the CTBTO [20].

This detection system was able to detect all the radioxenon of interest with respectable energy resolution and within the prescribed MDC requirements. Work on the ARSA detection system also provided insights on dealing with the interference from ^{222}Ra. It was suggested to inject the radon gas inside the plastic scintillator to collect its signatures. Daughters of ^{222}Ra emit photons in the energy range that interfere with ^{135}Xe, ^{133m}Xe, and ^{131m}Xe. Radon daughters also emit a photon at about 352 keV which doesn't interfere with the emissions of radioxenon. The solution put forth by PNNL was to compute the ratios of all the three photons in a set region of interest. These ratios can be used to subtract the counts in the ROI of an actual sample thereby offering a solution to the interference. Some of the drawbacks of the initial ARSA design include

the use of a plastic scintillator which led to an increase in the MDC (memory effect). Xenon gas diffuses through the walls of the gas cell leading to an elevated background which is detrimental for low-level counting. Other drawbacks of this design are the extensive gain matching that is required to be done because of several detection elements. This also leads to a second problem of the detection system, if one of the PMTs is lost in the system, there is a significant effect on the operation of the entire detector.

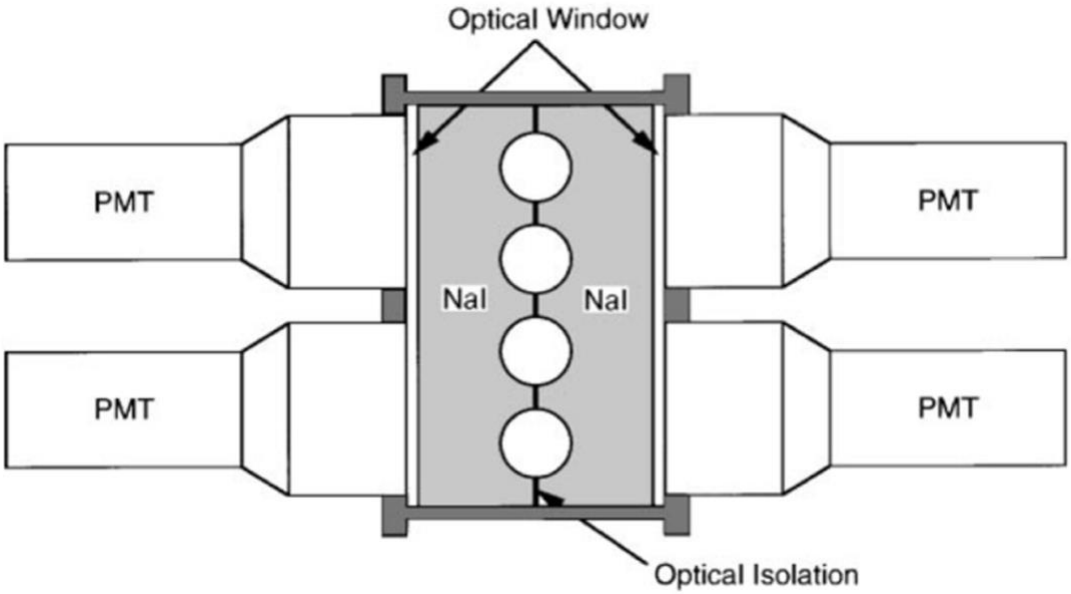

Fig. 24. The initial ARSA detection system showing the two NaI detectors and the four plastic detection cells

To overcome some of these drawbacks discussed previously, PNNL designed a revised version of the ARSA and named it *redesigned beta-gamma coincidence system* (Fig. 25) [143]. There were some significant changes made in the system including the use of a CsI(Na) rather than a NaI system. From a scintillation material standpoint, CsI(Na) offers higher physical density and electron density which leads to higher efficiencies. It is worth mentioning that at low energies (<100 keV) NaI offers better energy resolution than CsI(Na). Another major change made to the system was the use of four independent electron and photon detectors. This means each plastic gas cell had its own CsI(Na) detection media surrounding it. This led to the development of the system where the failure of a PMT will only cause one detection cell to fail and not the entire

system. Reduced amount of quality assurance and quality control, improved detection efficiency (solid angle), and robustness of the system are some of the advantages of this design. From an electronics standpoint, CsI(Na) has a similar decay time compared to NaI of about 630 ns which leads to no extensive changes in the electronics of the system.

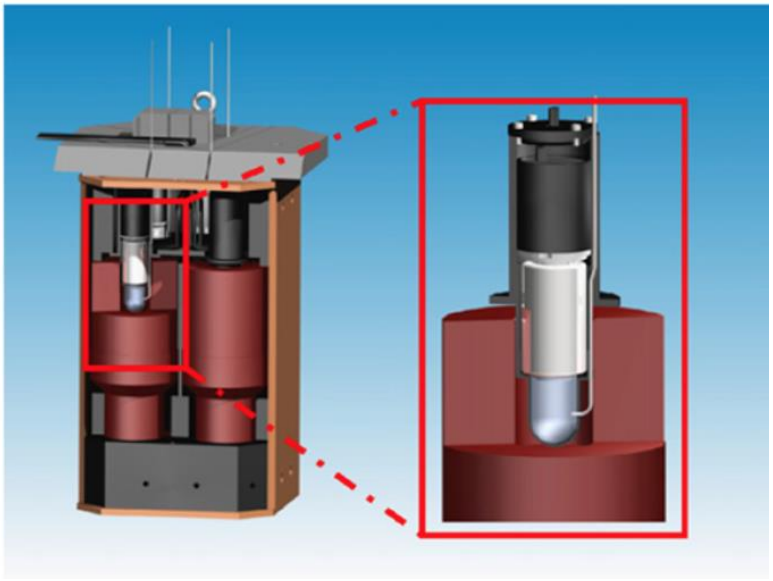

Fig. 25. The redesigned ARSA detection system. The plastic gas cell for beta detection and the CsI(Na) detector for photon detection are shown in the inset

Further development in the field of radioxenon detection at PNNL has been focused more on the improvement of gas processing parameters. These include sampling more gas or processing the gas in less amount of time. Efforts have also been made to improve the efficiency of gas sampling techniques. This work was a collaborative effort between PNNL and Teledyne Brown Engineering [21-23]. This system employs a NaI crystal in the capacity of a photon detector in conjunction with a plastic gas cell for photon detection. The general design is similar to that of the redesigned ARSA system except for changing the material from CsI(Na) back to NaI. Some additional requirements of the Xenon International as prescribed by PNNL includes a collection time of 8 hours with an objective of 6 hours. This helps in performing measurements in quick succession. The system is required to have a daily reporting frequency and measurement and time before reporting of 24 and 48 hours respectively. The MDC of

the system is estimated to be 0.3 mBq/m^3 for ^{131m}Xe, ^{133}Xe, and ^{133m}Xe with an objective of 0.15 mBq/m^3. For ^{135}Xe the MDC is aimed below 1 mBq/m^3 with a target of 0.5 mBq/m^3. Two-way communication with the system is required to be established with a 95% availability and an annual downtime of fewer than 15 days and a maximum of seven days consequent downtime. The MDC measurements with the Xenon International system suggest that an MDC of below 0.1 mBq/m^3 was achieved. The Xenon International system along with the nitrogen generator and the Uninterruptible Power Supply (UPS) is shown in Fig. 26 [144].

Fig. 26. The Xenon International system conceptualized at PNNL

2.4.2.2 Swedish Automatic Unit for Noble Gas Acquisition (SAUNA)

The SAUNA system was designed and developed by the Swedish Defense Research Agency (FOI). This system also employs a NaI and a plastic scintillator for photon and electron detection respectively. Both these systems operate in coincidence mode. The plastic scintillator in this design also acts in the capacity of a gas cell. Holes were machined in the NaI detectors to accommodate the plastic scintillators. Two PMTs were used for reading the optical photons from the electron detector. The NaI detectors were read by a single PMT. The gas cell and the aluminum thickness were chosen such

that the electron detection is maximized and the attenuation of the photons (especially the low energy 30 keV photons) is minimized. A 5 cm thick lead shield was used in the capacity of a radiation shield and an additional 5mm of copper was used to absorb the X-ray emitted by the lead. Standard NIM bin modules and CAMAC electronics were used for signal readout. Fig. 27 shows the SAUNA detection system [17]. As it can be observed there are two independent gas cells used in this design, this is done primarily to remedy the problem of memory effect which is observed in the SAUNA as well.

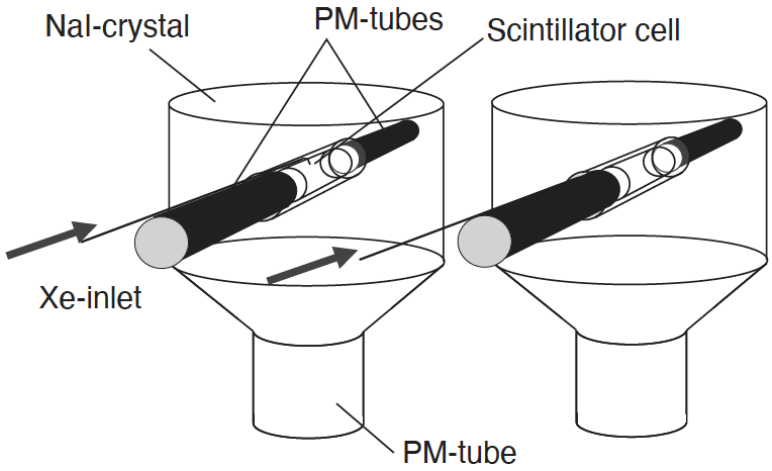

Fig. 27. The SAUNA detection system showing the Xenon gas inlet, NaI crystal, the plastic detector for electron detection and the PMTs

The SAUNA detection system was successful in identifying all the radioxenons of interest. This system also achieved an MDC of below 1mBq/m^3 during the Internal Noble Gas Experiment (INGE). Significant drawbacks of these systems include complex gain matching followed by the memory effect. Efforts have been put to remedy the problem of memory effect by coating the interiors of the gas cell with aluminum oxide (Al_2O_3). This process is called Atomic Layer Deposition (ALD), in this method, the material is deposited slowly in the form of thin layers on the surface of an object [145, 146]. This layer ensures that no gas diffuses through the gas cell wall during the process of gas counting. It must however be noted that coating the interiors of the gas cell with a relatively high atomic number material will have detrimental effects on the detection efficiency of the cell. This path was followed since it was

concluded that the memory effect and the resulting lack of detecting low-level activities outweigh the effects of a reduction in the detection efficiency of the electrons.

The Swedish Defense Research Agency also focused their efforts on the improvement of the gas processing systems in the upcoming designs. After the initial SAUNA design, they came up with two new models, the SAUNA II and SAUNA III (Fig. 28) [147-150]. Some of the reasons the FOI pointed to justify the development of new designs include outdated technology, unknown radioxenon backgrounds around the world, and CTBTO preparatory committee requirements were set more than 20 years ago based only on the inputs from the radiation detection standpoint while currently there have been significant improvements made in the field of gas processing technologies, global radioxenon background database, and significant improvements in the field of radiation detection. The practical reasons highlighted include a need to improve reliability, maintainability, and user friendliness. Other potential improvements include improvements in the detection efficiency, uncertainty measurement, and time resolution. Other major changes include the use of a nitrogen carrier gas instead of helium, increased air sampling rate and doubled the number of samples per day from 2 to 4 in the SAUNA III design compared to SAUNA II.

Fig. 28. The SAUNA III detection system

Other major system specifications and results from the SAUNA II/ III design are shown in Table 4 [149].

Table 4. Operational differences and major results from the SAUNA II and SAUNA III detection systems

Parameter	SAUNA II	SAUNA III
Xenon sample (cm^3)	1.25	3.25
Airflow (m^3/hour)	1.44	6.00
Memory Effect (%)	<0.1	<0.06
Detector Technology	NaI/Plastic	NaI/Plastic
MDC ^{131m}Xe (mBq/m^3)	0.2	0.1
MDC ^{133m}Xe (mBq/m^3)	0.2	0.1
MDC ^{133}Xe (mBq/m^3)	0.2	0.15
MDC ^{135}Xe (mBq/m^3)	0.7	0.3

2.4.2.3 Automatic Radioanalyzer for Isotopic Xenon (ARIX)

The Khlopin Radium Institute (KRI) in the Russian Federation developed the Automatic Radioanalyzer for Isotopic Xenon (ARIX) [18, 19, 151]. There were two iterations of the design that were developed over the years. In the initial design, it was decided to use a NaI detection system coated with a plastic scintillator on the interiors of the gas cell. The NaI detector was machined to accommodate this design. Xenon gas was loaded in the gas cell and events were identified based on a coincidence detection system between the NaI photon detector and the plastic detection media that was coated on the inside of the photon detector. This type of detection is called beta gated gamma coincidence. In this detector, the electron energy was not detected because the layer of plastic scintillator material used was too thin to effectively measure the energy of the electron. Therefore, the system was triggered based on the fact that an electron has interacted with the plastic detector. The photon energy on the other hand was successfully recorded. The energy spectrum thus obtained includes only the photon

energies. There are some significant drawbacks to this method. Xe-131m and ^{133m}Xe both emit a 31 keV X-ray photon and a conversion electron at 129 and 199 keV respectively. In the current design, differentiation can't be achieved based on the 30 keV photon that is released since this is emitted from both the isotopes (^{131m}Xe and ^{133m}Xe). One possible solution is to employ the fact that both these radionuclides have different half-lives, so based on this we might be able to estimate the contribution from both these isotopes. The drawback of this method is that the CTBTO requires the IMS stations report data daily but a 7–10-day lag in data reporting would result in not meeting the requirements of the CTBTO. Fig. 29 shows the initial design of the ARIX detection system [151].

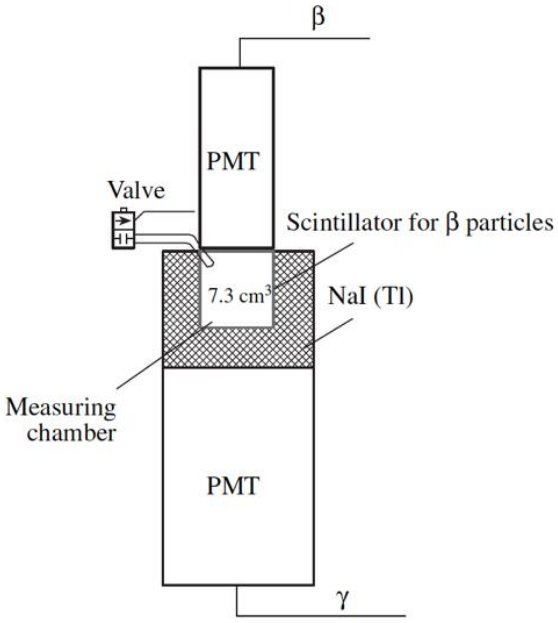

Fig. 29. The initial ARIX detection system illustrating the NaI detector, the gas inject line, and the PMT for the electron and photon detectors

Therefore, to remedy this situation, the redesigned version of the ARIX detection system employed the concept of electron-photon spectroscopy based on coincidence-based detection. This was achieved by employing a plastic scintillator for electron detection in conjunction with a NaI photon detector. In the revised design, both the electron and photon energies were independently captured, this enabled accurate reporting of the ^{131m}Xe and ^{133m}Xe activities and MDC values for both these radioxenon.

2.4.2.4 Système de Prélèvement Automatique en Ligne Avec l'Analyse du Xénon (SPALAX™)

The SPALAX detection system was developed by the French Atomic Energy Commission (CEA). The first iteration of this detector was only sensitive to the photons being emitted from the radioxenon. For photon detection, the SPALAX employed an HPGe detector. This was successful in achieving an exceptional photon detection resolution, the major drawbacks of this detection system include the bulky cooling systems that are required for an HPGe detector followed by low detection efficiency for a germanium crystal as opposed to other detection media like NaI, and its operation in the singles mode which makes this system vulnerable to stray background counts which might fall in the ROI, thereby increasing the MDC [69, 77, 78, 152, 153].

To improve some of the above drawbacks the second iteration of the design used a PIPSBox in conjunction with a NaI detection system. The PIPSBox uses silicon wafers measuring about 0.5 mm in width to achieve electron detection. A significant drawback of this system however is considerable electron backscatter which leads to peak broadening and a tail at energies below the full energy peak. The other downside of this detector is the solid angle of the system, not all electrons emitted by the radioxenon of interest are actually detected by the silicon because of a solid angle of less than 4π for electron detection. This detector operated in coincidence mode with dedicated detection media for each type of radiation. This design was successful in achieving a very low background and near-zero memory effect because of using the PIPSBox. The third generation of the SPALAX detection system employed the PIPSBox in the capacity of an electron detector and a broad energy germanium detector in the capacity of a photon detector. This ensures the best possible energy resolution for both electron and photon detection. The volume of the gas cell was 11.7 cm^3 and ultra-pure aluminum was used to make the external body of the detector which also acts in the capacity of a gas cell. The 129 keV peak was reported to have an energy resolution of 7% FWHM. This high resolution enabled it to successfully distinguish the 129 keV and 160 keV conversion electrons from ^{131m}Xe. This system also offers a very low background and memory effect. All these factors coupled with relatively high detection efficiencies

compared to the previous versions enabled a drastic reduction in the MDCs. This detector was successful in achieving an MDC of 0.1 mBq/m^3 for ^{131m}Xe, ^{133m}Xe, and ^{133}Xe, while an MDC of 0.3 mBq/m^3 was achieved for ^{135}Xe which are significantly below the MDC requirements set by the CTBTO. Fig. 30a shows the SPALAX-NG detection system. The internals of the PIPSBox (silicon wafer) and the externals along with the carbon window are shown in Fig. 30b and Fig. 30c respectively.

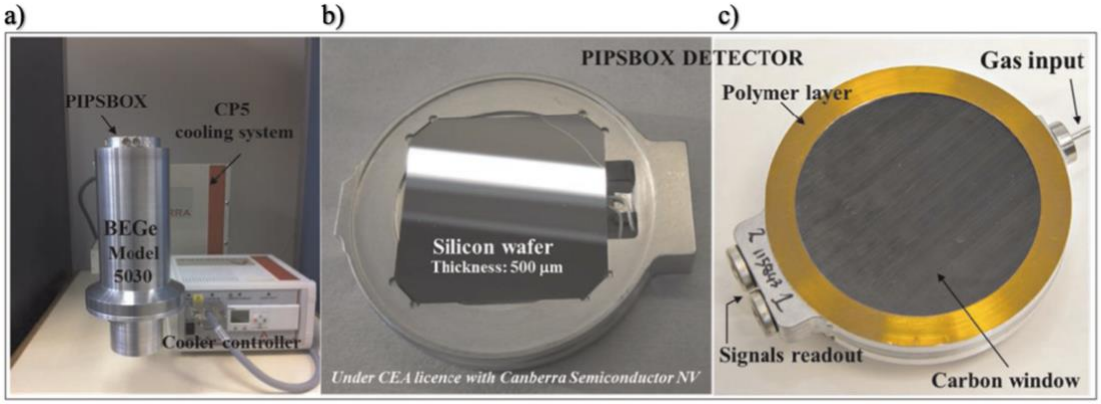

Fig. 30. a) The SPALAX-NG detector showing the PIPSBox, the Germanium detector and the cooling system; b) The PIPSBox detector without the carbon window showing the silicon wafer; c) the PIPSBox detector showing the gas input line, carbon window for reducing background and the signal readout from both the wafers

Work on the SPALAX family of detection systems also suggested techniques to calculate the MDC if no counts were detected inside the ROI. The MDC equation has two general terms, one dependent on the detector geometry and one dependent on the number of counts that are recorded inside the MDC. Some research groups have only taken into account the geometric factor while reporting the MDC but work on the SPALAX system suggested expanding the ROI if no counts are detected. This is done in small increments in both directions (electron and photon axis) until a count is detected. In this case, the counts in the ROI will be calculated as the ratio of the area under the initial ROI and the expanded ROI where the first count is detected. The SPALAX-NG detection system was able to sample 60 m^3 of air every 8 hours, several other significant improvements have also been made in the gas processing and radiation detection front of the SPALAX design.

2.4.3 Other Radioxenon Detection Systems

Apart from the prominent radioxenon detection systems developed by major national labs, research institutes, various other research groups have developed prototypes of radioxenon detection systems. Some of the detectors covered in this section include phoswich detectors developed by various groups, novel radioxenon detection systems, and other coincidence-based detection systems that were based on the detectors previously discussed.

The first detection system going to be discussed is the Gas Proportional Scintillation Counter (GPSC) [154]. This detector is sensitive to only photons. In this system, low energy X-ray photons were used to sense radioxenon. Although this novel detection technique was effective in detecting X-rays, high-energy photons were not detected using this system, and since this system doesn't operate in coincidence, no information regarding the electron energies is collected and this system is also susceptible to background radiation. Another novel detection method is the Gas Analysis, Separation, and Purification System (GASP) [155]. In this detector, the radioactive noble gas is passed through the detector at variable pressure and flow rates and the number of counts that are recorded in each pass is used to calculate the activity of the sample. The drawback of this method is the variable electron efficiency at each pressure. Various other works have also suggested that variable pressure has a pronounced effect on the detection efficiency of the electron. Recently a well-type plastic cell in coincidence with an HPGe detector was designed. In this design, the plastic cell acts in the capacity of the electron detector/ gas cell and the HPGe is used for photon detection. This system had a gas cell volume of 8.8 cm^3 and the 129 keV conversion electron resolution was determined to be about 29%. This radioxenon detection system was also successful in achieving an MDC of below 1 mBq/m^3 for all radioxenon of interest. Various attempts have also been made to design a single channel and an electron gated gamma spectroscopy device for radioxenon detection. The electron gated detection system reported a Minimum Detectable Activity (MDA) of 1.8 mBq after a 24-hour measurement using ^{133}Xe. The single-channel photon detection system was able to detect the radioxenon of interest, but the MDC values were three orders of magnitude

over the CTBTO prescribed limits [156]. Fig. 31 shows a pictorial representation of the GPSC system.

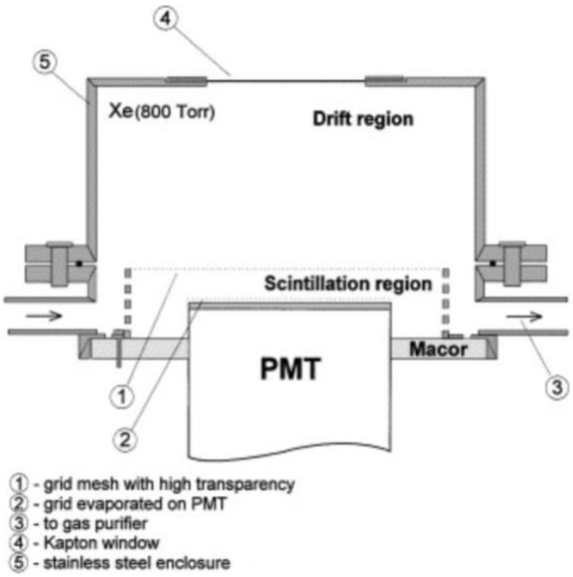

Fig. 31. Schematic of the Gas Proportional Scintillation Counter

This section goes over the phoswich detectors that were designed over the years. Attempts were initially made by PNNL to develop a phoswich detection system using NaI(Tl) and CaF_2(Eu). Initial results suggested that there was a need to develop algorithms that are successful in performing pulse shape discrimination in real-time [157]. XIA LLC developed a phoswich detection system consisting of CsI(Tl) and BC-404 for radioxenon measurements. This system implemented the concepts of pulse shape discrimination and integrated readout electronics. Literature suggests that the MDC, background count rate and the memory effect of the system were comparable to the state of the art [158, 159]. A three-element phoswich detection system with active Compton suppression and real-time pulse processing using an FPGA was designed at Oregon State University for radioxenon detection [26, 28, 34]. This system was successful in detecting all the radioxenon of interest and achieved an MDC of below 1 mBq/m^3.

Efforts have also been put into the development of coincidence-based detection systems using a plastic scintillator for electron detection and a well-type NaI detector for photon

detection. The Iranian Noble Gas Analyzing System (INGAS) was able to attain an MDA of 1.24 Bq after 24-hour counting of ^{133}Xe, which is comparable to the state-of-the-art detection systems (Fig. 32) [160]. A Stilbene-based radioxenon detection was also developed where pulse shape discrimination was implemented to improve the MDC. This detector used a NaI detector in coincidence with a stilbene gas cell for photon and electron detection respectively. Preliminary results indicated that an improvement of 1% in the MDC was observed because of implementing pulse shape discrimination [161].

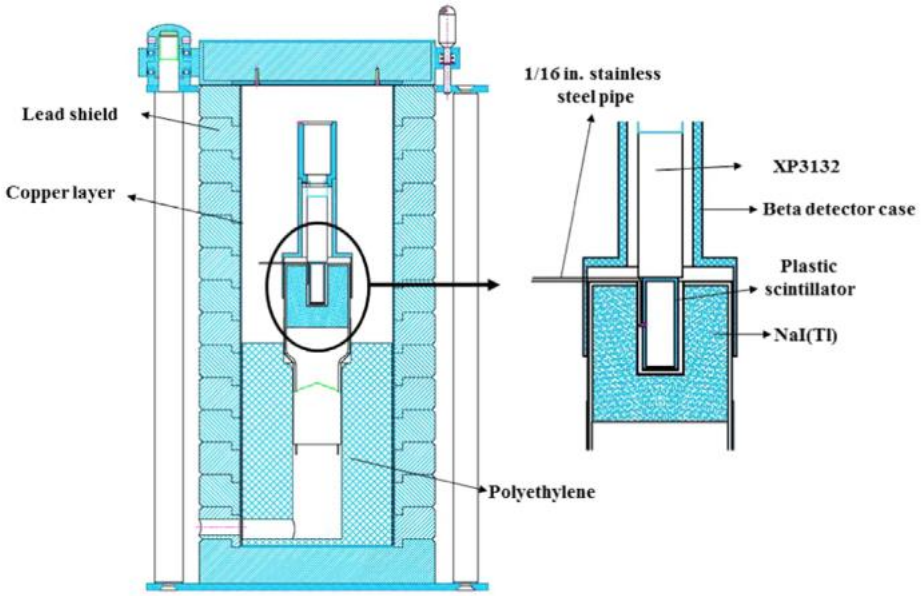

Fig. 32. The Iranian Noble Gas Analyzing System (INGAS) for radioxenon measurement

2.4.4 Radioxenon Detection Systems Developed at Oregon State University

Over the past few years, Oregon State University has developed several radioxenon detection systems. In this section, we shall be going over the Two Element CdZnTe (TECZT), a plastic and CZT detection system (CASP), the Stilbene-CZT detection system, a PIPS-CZT, and a PIPS-SrI_2 detection system. In these technologies, electrons and photons have been detected using both scintillation and semiconductor technologies. An attempt has also been made to detect these radiations using more than one detection media for the same radiation type (either photon or electron). For work

carried out at OSU, stable xenon isotopes have been loaded in a syringe and irradiated at the Oregon State University TRIGA reactor thermal column, the flux at this location was about 7 x 10^{10} n cm^{-2} s^{-1}. After irradiating the gas, the samples were injected into the detection system to record the radioxenon signatures. In the following sections, we shall briefly go over each detection system, its respective design, advantages, and drawbacks.

2.4.4.1 Two Element CdZnTe (TECZT)

The Two element CdZnTe (CZT) system featured two face to face 1x1x1 cm^3 CZT detectors. These detectors were responsible for sensing both electrons and photons [25, 27]. An inject hole was located on the side of the gas cell to facilitate radioxenon injection. The gas cell was 3D printed and epoxy was used to seal the area after positioning the CZTs to ensure airtightness. A coplanar anode pattern was chosen to take advantage of the single charge carrier design. Overall, each functional CZT features a cathode, which would generally be subjected to ~1000V, and two anodes. Fig. 36a shows the TECZT detection system. The non-collecting anode would be placed at a relatively higher negative potential compared to the collecting electrode to steer the incoming electron in the right anode. This design would enable charge induction on both anodes till the electrons reach very close to the anode where they would be sensed by the collecting electrode (because of a relatively higher potential). Real-time coincidence identification was achieved using an FPGA, once a coincidence event was identified, the FPGA would transfer the pulse data to a MATLAB interface for amplitude identification and histogram plotting.

This detection system was excellent for detecting photons. As for electrons, because of the high atomic number nature of the CZT, it resulted in extensive electron backscatter which resulted in a tail below the conversion electron peak. Some of the other drawbacks of this system include the poor detection solid angle because the detection elements were recording emissions from only 2 of the 6 possible sides. Since each CZT requires two dedicated preamplifiers and a subtraction circuit, the electronics of the TECZT system were relatively complex.

2.4.4.2 A CZT Crystal, an Array of SiPMs, and a Plastic Scintillator (CASP)

The CASP detection system employs a plastic scintillator in conjunction with a SiPM array for electron detection operating in coincidence with a CZT detector for photon detection [29, 30]. This system also uses an FPGA to identify coincidence events and the MATLAB user interface is responsible for computing energy deposition and histogram plotting histogram as well as recording the individual pulse data. For this work, a 1x1x1 cm^3 CZT crystal along with a well-type plastic scintillator is used. This plastic scintillator works in the capacity of a gas cell and an electron detector. The thickness has been chosen such that the intrinsic electron detection efficiency is unity, and the photon attenuation is minimum, especially for the low energy X-rays. An inject hole has been machined at the top to accommodate the inject tube for transferring the irradiated radioxenon from the TRIGA reactor.

This detector improved some of the drawbacks observed in the TECZT detector like electron detection efficiency and electron backscatter. All the signatures from the radioxenon of interest were positively identified and the MDC of the system was also respectable compared to the state of the art except for ^{135}Xe. The major drawbacks of this system were poor photon detection efficiency and memory effect. Since only one CZT was used in this work, a lot of coincidence events weren't recorded by the system which ultimately led to poor detection efficiency for photons. This ultimately resulted in a poor MDC for ^{135}Xe. When calculations were performed even with no counts inside the region of interest the MDC obtained was close to 1mBq/m^3 for ^{135}Xe, this is because the MDC equation consists of two terms, one for the detection efficiency and the other for the actual counts inside the ROI. Since a plastic scintillator was used in this work, this led to the introduction of the memory effect in the system. A memory effect of about 5% is estimated based on the literature. This is the first detector employing a mix of scintillator and semiconductor technologies for radioxenon measurement that was developed at Oregon State University.

2.4.4.3 PIPS-CZT

The PIPS-CZT detection system uses the CZT for photon detection and the PIPSBox for the detection of electrons [31, 37]. The PIPSBox consists of two detection bodies, the passive implanted planar silicon (PIPS) is a thin layer of silicon about 0.5 mm thick which performs the task of electron detection. Two CZTs were mounted right next to the outer casing of the PIPSBox to facilitate photon sensing. Each of the CZTs measure 1x1x1 cm^3 and employ single charge sensing by implementing a coplanar grid anode pattern. The PIPSBox was manufactured by Mirion Technologies and the encapsulated CZTs were grown by Kromek. It must however be noted that the Silicon wafers are held in place by an Aluminum body and an external carbon window is located on either side to prevent any charged particle interaction with the silicon. This system requires a total of 4 detection channels and a coincidence pattern was defined such that a coincidence between either a silicon or a CZT is recorded. Efforts were also put into summing the signal from the two PIPSBox channels if a coincidence is detected in conjunction with a CZT. An 8-channel digital pulse processor was designed and developed at OSU with a MATLAB interface for real-time coincidence identification using the Xilinx Kintex-7 FPGA. Fig. 36b shows the PIPS-CZT radioxenon detection system. The sizes of the CZTs relative to the PIPSBox are worth pointing out in terms of photon efficiency.

One of the prominent advantages of using this design was a drastic reduction in memory effect (about 20 times) which is extremely valuable in running experiments in quick succession. The electron energy resolution obtained for the 129 keV conversion electron of 12.5% FHWM is about half of what would be obtained had a plastic scintillator been used. The 129 and the 159 keV conversion electrons were successfully captured in the spectrum, something that would not be feasible with a plastic scintillator. Some of the drawbacks of this system however were its electron backscatter and poor photon detection solid angle. Although efforts have been made to digitally sum the backscattered electrons, the threshold of each silicon wafer and the fact that the solid angle of the PIPSBox is not 4π inevitably leads to a tail below the full energy

peak. The use of CZT limits the photon detection efficiency which also has a detrimental effect on the MDC of the system.

2.4.4.4 Stilbene-CZT

The Stilbene-CZT detector uses the same system developed for the CASP detection system but replaces the plastic with a stilbene gas cell and uses a higher grade CZT from Redlen Technologies [32, 37]. For this work also it was decided to use a coplanar grid anode design, the CZTs were encapsulated to prevent degradation due to external factors. Stilbene was chosen because of its superior electron energy resolution and near-zero memory effect. The external diameter of the stilbene gas cell was chosen to match the size of the SiPM array that was used in the CASP system. The wall thickness was maintained at 1.8 mm and the detector was built using three parts made out of stilbene (the body, top, and bottom cap). There is a fused silica layer at the bottom end to enable refractive index matching with the optical photon detector. A 2-channel DPP was used for reading pulses from the detector and the MATLAB user interface was used for pulse processing and displaying the histogram. The stilbene CZT system mounted on the Printed Circuit Board (PCB) is shown in Fig. 36c.

This system positively identified all the signatures from the radioxenon of interest. A memory effect of 0.045% was reported for this stilbene gas cell, almost two orders of magnitude reduction compared to plastic scintillators. An improvement in energy resolution of about 15% was observed for the 129 keV conversion electron from ^{131m}Xe compared to a plastic scintillator. Although this detector was successful in addressing the drawbacks faced by most of the detection systems discussed above, the problem of poor photon solid angle remained.

2.4.4.5 PIPS-SrI_2(Eu)

The PIPS-SrI_2(Eu) system employs a PIPSBox in the capacity of an electron detector and the SrI_2(Eu) for photon detection [162]. This system operates in coincidence mode and requires the use of the 8-channel digital pulse processor for signal readout, coincidence identification, and eventual data processing is performed using the MATLAB user interface. 2 '*D*' shaped SrI_2(Eu) crystals read by SiPM arrays are used for sensing optical photons from the scintillator. Four of the eight-channel digital pulse processor channels were utilized in reading the signals from the detectors. A dedicated preamplifier for the PIPS box was used to reduce the noise in the system. This detection system solved the problem of low photon detection efficiencies that were observed in the PIPS-CZT system while maintaining its low memory effect. Problems related to electron backscatter remain in this system. Fig. 36d shows the PIPS-SrI_2(Eu) detection system.

This system was successful in identifying all the signatures from the radioxenon of interest. The increase in photon detection has resulted in MDCs below 1mBq/m^3 for all radioxenon including ^{135}Xe. The memory effect of the system was also about 0.318% (similar to what was observed in the PIPS-CZT detection system). The main drawbacks of this system include the high cost of the PIPSBox and the dedicated preamplifier (~$55,000) and the slow response time of the SrI_2(Eu) scintillator. Although this scintillator is one of the brightest scintillators used for radiation detection, strontium iodide has a slow primary decay time of about 1 μs and secondary decay time constant of 5 μs which make it slow compared to standard NaI or fast scintillators like $LaBr_3$ or $CeBr_3$.

2.5 Motivation

Considering all the detection systems that were developed, some of the major factors of importance are high photon and electron detection efficiency, low memory effect, no electron backscatter, no complex gain matching or electronic processing, and high-resolution materials. In this work, an attempt has been made to address a majority of

the shortcomings of the detection systems that were developed in the past. It is anticipated that this system will be successful in detecting the radioxenon signatures of interest and achieve an MDC of below 1mBq/m^3 to meet the requirements of the CTBTO.

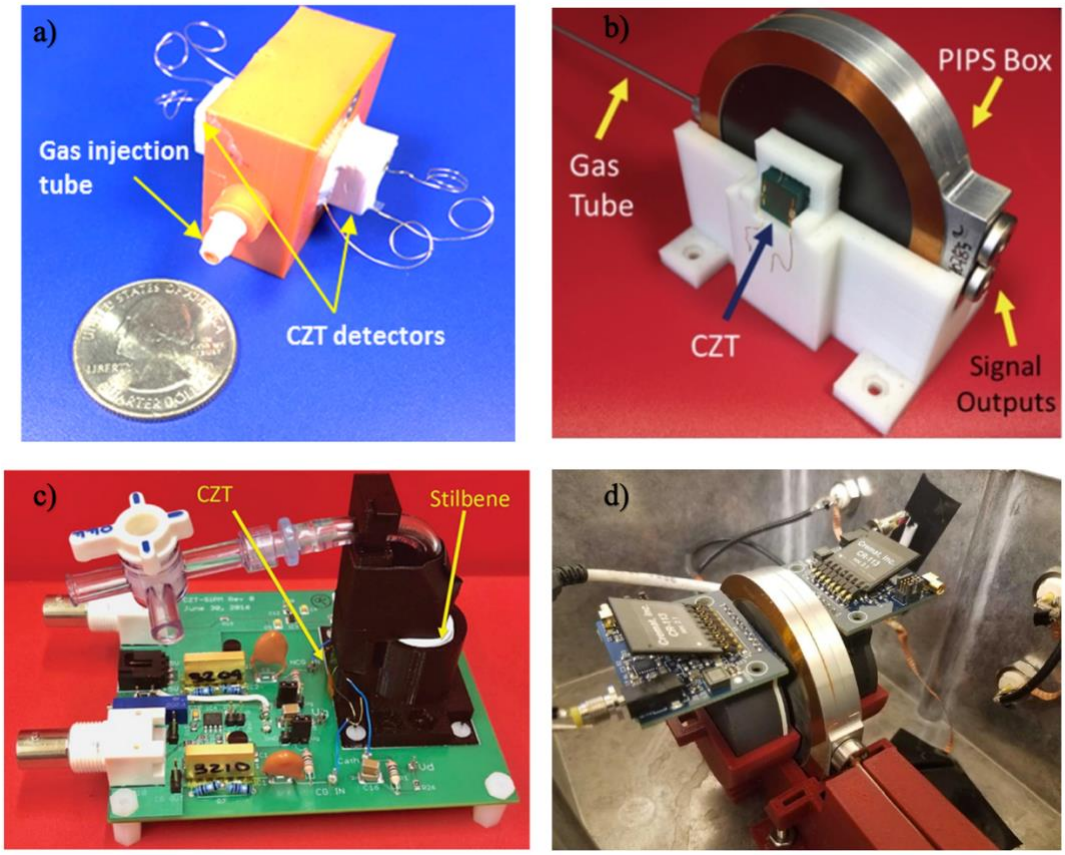

Fig. 33. The CZTs inside the detector holder and the inject hole along with a quarter dollar coin for reference (TECZT); b) the PIPS-CZT detector showing the PIPSBox, CZT, the gas injection line, and the signal output; c) the stilbene-CZT detector mounted on a PCB; d) the PIPS-SrI_2(Eu) detector showing the D-shaped detectors mounted on the exteriors of the PIPSBox carbon window

3. MATERIALS AND METHODS

This research work mainly concentrates on the developments of the $SrI_2(Eu)$ – Stilbene detection system. Some sections of this work are also dedicated to the initial $CeBr_3$ – Stilbene detection system and the challenges that were faced in this design. In the path towards developing and designing these detection systems, several requirements/ guidelines were followed. In this section, we shall be covering the design requirements for these systems, strategies/ methods that were used to realize these detectors, and challenges that were faced in the process.

Radioxenon detection systems are very high sensitivity detection systems that are required to achieve an MDC of below 1 mBq/m^3 for ^{133}Xe according to the CTBTO. However, nowadays an MDC requirement of below 1 mBq/m^3 is extended for all four radioxenons of interest. Several factors play a role in the design of a good detector, one of the factors is the coincidence identification module. This is the functional block responsible for detecting coincidence events in real-time, therefore there have been several experiments that were conducted to ensure the successful functioning of the coincidence identification module. Maintaining a low coincidence time window also ensures that stray background events are not accidentally recorded, which eventually plays an important role in quantifying the MDC of the system. For achieving a low MDC there are a couple of other factors that play a role such as, employing a high-resolution detection media for electors and photons, high detection efficiency, low memory effect, and low counts in the regions of interest during background acquisition. The use of a single, low atomic number electron detection media ensures that there is no significant electron backscatter while maintaining a high intrinsic detection efficiency. The stilbene detection system has also been previously used in conjunction with the CZT and has achieved an excellent memory effect. This high solid angle also ensures that a high detection efficiency is achieved. The 31 keV X-ray is released by three of the four radioxenon of interest, therefore this also imposes a restriction that the attenuation of the X-ray is maintained as low as possible. On the photon detection front, two materials have been explored, $CeBr_3$ and $SrI_2(Eu)$. It was initially decided to

explore the $CeBr_3$ option but complications during experimentation and detector performance forced the use of $SrI_2(Eu)$. In this work, we shall briefly be going over the various detection material options that were explored, the challenges in the use of some of these materials, and the $CeBr_3$ /$SrI_2(Eu)$ detector designs.

The Stilbene-$SrI_2(Eu)$ design is a low background, high sensitivity radioxenon detection system. The use of stilbene for electron detection ensures that the memory effect is maintained very low (about two orders of magnitude below that of plastic scintillators). The use of two-photon detection bodies plays a vital role in improving the photon detection efficiency compared to other designs like the TECZT or CASP. Although it must be pointed out that the photon detector design is the same that was used in the PIPS- $SrI_2(Eu)$ detection system. The only difference is the use of stilbene instead of the PIPSBox. This theoretically offers an advantage, a significant improvement in the electron detection efficiency which has an inverse effect on the MDC, which means a high detection efficiency directly translates to a reduced MDC. On the flip side, the use of stilbene doesn't offer the same energy resolution as the PIPSBox. Using low energy resolution materials requires defining a wider ROI which increases the chances of recording a higher number of background events. Taking a closer look at the MDC equation points to the linear square root relation between the MDC and the number of counts recorded during the background measurements. Taking this into account, the Stilbene-$SrI_2(Eu)$ detection system is expected to produce an improvement in the MDC of the system although there is an expected reduction in the conversion electron energy resolution. Fig. 34 and Fig. 35 show the SolidWorks cut section views of the Stilbene-$CeBr_3$ and the Stilbene-$SrI_2(Eu)$ detection systems respectively. The internals of the electron and photon detection media have also been illustrated.

In addition to the development of these systems, significant efforts have also been put into the compilation of the Geant4 optical photon decks. This was initially done to observe the optical photon distribution in the $CeBr_3$ design. Several reflection models

and surface materials have been utilized. Finally, a comparison between the Geant4 and the DETECT2000 optical transport model has been performed.

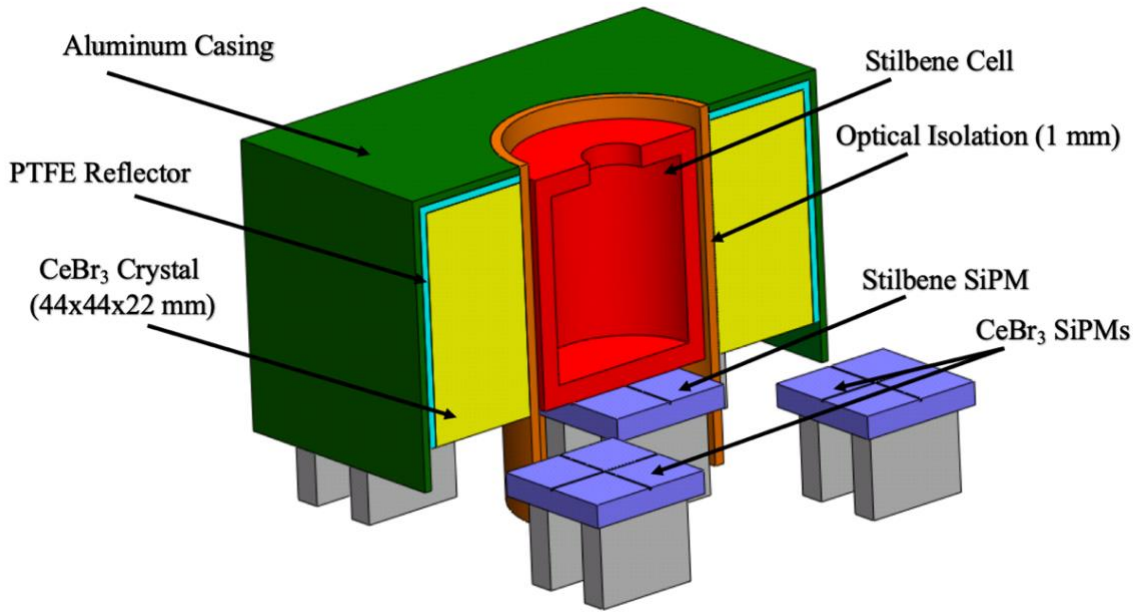

Fig. 34. SolidWorks cut section view of the Stilbene – $CeBr_3$ radioxenon detection system design

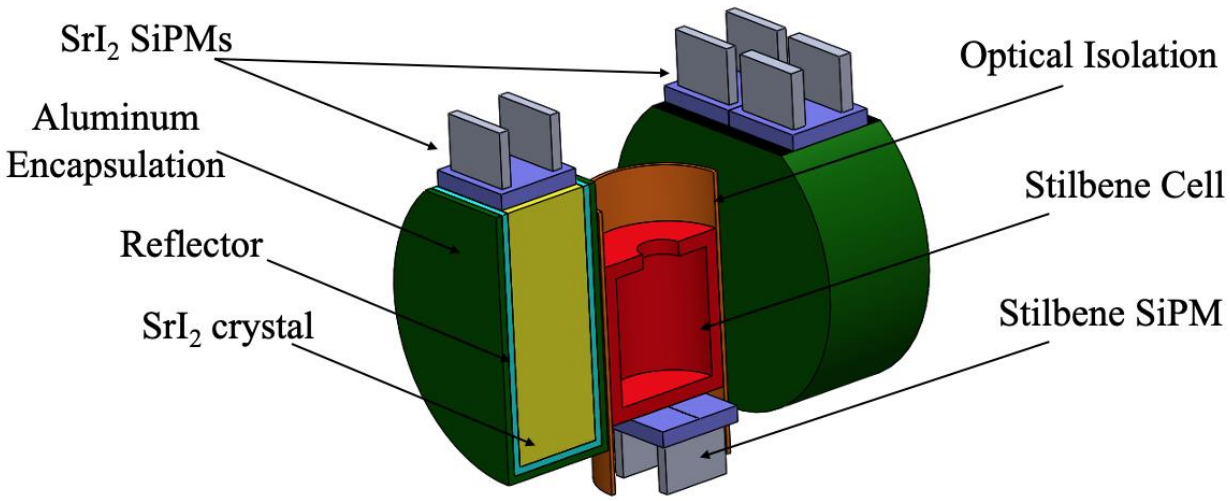

Fig. 35. SolidWorks cut section view of the Stilbene – SrI_2(Eu) radioxenon detection system design

It must be pointed out that the signals from the SiPM anodes were read by a custom-built PCB. The analog conditioning electronics were all present on the board and the signals from the SiPMs were routed through these electronics before being read by the digital pulse processor.

3.1 Detection Media and Components

3.1.1 Cerium Bromide ($CeBr_3$)

The Cerium bromide which was initially planned for this work was grown and assembled by Hilger Crystals Ltd. This detector was designed with keeping in mind some of the factors to improve the MDC like the detection efficiency of the $CeBr_3$. Therefore, to realize this, it was decided to employ a thru-hole detector design to allow radiation photons to be sensed from all directions. For optical photon readout, four SensL J series SiPMs (ARRAYJ-60035-4P-PCB) were mounted at the corners of the detector. To maximize the light collection efficiency of the detector, it was decided to use a Teflon reflector on all sides of the detector. Additionally, an Aluminum casing was used to act in the capacity of encapsulation to prevent any moisture uptake by the crystal, since $CeBr_3$ is hygroscopic in nature. Sensing the 30 keV X-ray was of utmost importance, therefore, care was taken to ensure that the thickness of the aluminum casing was minimum in the thru hole to enable the passing of the X-rays without significant attenuation. From prior experience, it was observed that in some cases optical photons from under the SiPMs can also interact with the microcells and cause them to fire, these interactions are no different from actual optical photons from a scintillator. Therefore, to prevent such unwarranted interactions, the underside of the SiPMs was backfilled with a 2mm thick grey color potting compound seal. SiPMs were aligned at the corners and mounted using a 310M-2 SiPM/ crystal optical interface to facilitate optimal photon transport.

$CeBr_3$ is one of the fastest scintillators with a decay time of about 20 ns and also one of the brightest with an optical photon yield of about 68,000 photons per MeV. These factors accompanied by its excellent energy resolution of about 4% FWHM for the 662 keV peak makes it one of the most attractive materials for modern-day spectroscopy

applications. This scintillator peaks at about 370 nm which does not exactly align with the sensitivity peak of the SensL J-Series SiPMs. It must however be noted that although the SensL SiPMs peak at about 420 nm, these SiPMs maintain a PDE of above 25% in the wavelength of interest for the $CeBr_3$ detector with a 2.5V SiPM overvoltage. Similar comparisons were also performed for the choice of reflector material between Polytetrafluoroethylene (PTFE) or more commonly known as Teflon and Enhanced Specular Reflector (ESR) by 3M. The literature points out that Teflon would act as a better reflector compared to ESR, especially below 400 nm [163, 164].

For our application, where the design of compact detectors is important, SiPMs play an integral role in realizing these designs. Their compact and modular nature is often of great interest to the researchers since it allows them to place the photon detectors in various configurations, unlike PMTs where there are strict restrictions. This also raises a question of performance comparison between PMTs and SiPMs in terms of energy resolution. The literature review suggested that various series of SensL SiPMs have been tested with $CeBr_3$ and have reported an energy resolution of 6.6%, 5.6%, and 4.8% for the C, B, and J series respectively [165-167]. Therefore, it was decided to continue and explore the usage of SiPMs in this design. The top view and the cut section view of the $CeBr_3$ detector are shown in Fig. 36 and Fig. 37 respectively. This design would have yielded a solid angle of about 2.5π as opposed to ~0.2π in the case of the CASP.

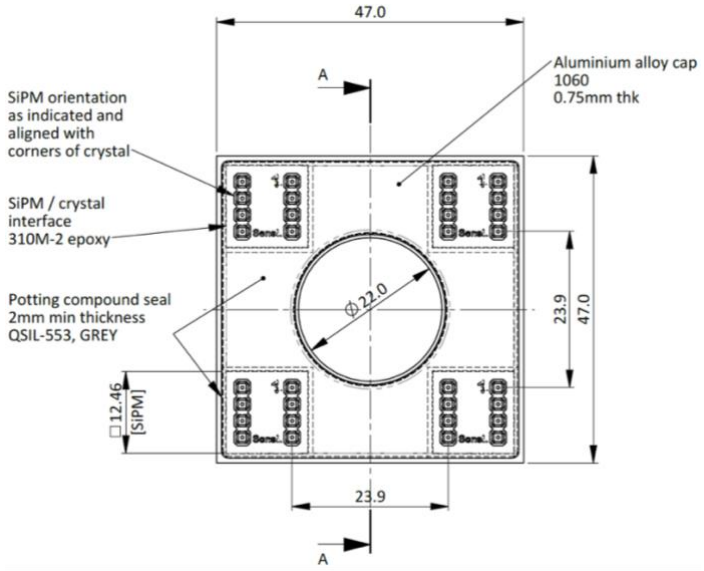

Fig. 36. Bottom view of the $CeBr_3$ detector

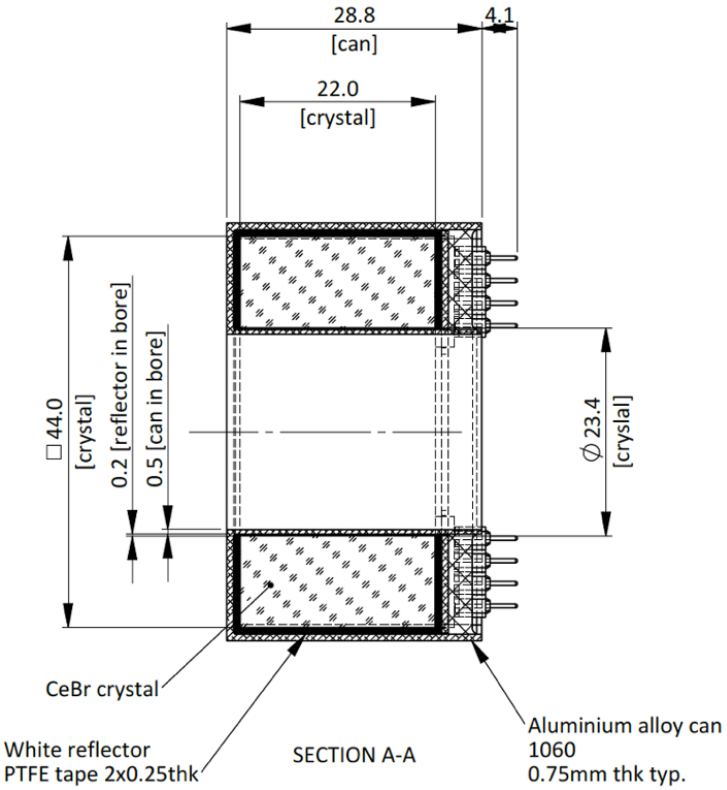

Fig. 37. Cut section view of the $CeBr_3$ detector showing the internal dimensions of the crystal, PTFE reflector and the encapsulation

The detector measures 47 x 47 x 28.8 mm^3 with a 22 mm diameter thru-hole in the center for accommodating the stilbene detector. The stilbene detector measures 18.7 mm in diameter and including the Teflon wrapping the diameter increases to about 19.70 mm. It was decided to accommodate a 1 mm thick optical isolation ring to prevent external photons from interacting with the SiPM. The additional 0.3 mm was provided for any clearance to place the isolation ring and the stilbene on top of the SiPM. The aluminum casing was used to prevent any moisture uptake and maintain the light-tight nature of the detector. On the external surfaces, 0.75 mm thick aluminum was used while in the thru hole, the thickness dropped to 0.5 mm to reduce the attenuation of the 31 keV X-ray. PTFE was used as a reflector to increase light collection efficiency. The SiPMs were mounted at the four corners of the detector and backfilled with a potting seal to maintain light/ air tightness and also prevent any optical photon interaction with the SiPMs from under the surface. The distance between the

pins of each array was maintained at about 23.9 mm, this distance was used in designing the PCB board for signal readout.

On the PCB side, both the stilbene and $CeBr_3$ were planned to be powered using a single +5V power supply. The power supply was then routed through the LT8410 ultralow-power boost converter to step up the voltage to about +28.5V to power the cathodes of the SiPMs [168]. Since there is a single array used for reading out photons from the stilbene, the anode outputs from the four stilbene SiPM pixels are summed and read. Readout from the 4 SiPM arrays for $CeBr_3$ presents us with two options, either all the anode outputs from the 4 SiPM arrays (16 in all) can be summed together and routed through an op-amp or each SiPM array's anode signals (4 each) can be routed through an individual op-amp and then summed together at the end. Although the first option requires the use of fewer electronic components, the fact that connecting 16 anodes in parallel leads to a drastic increase in the circuit capacitance (capacitance ads linearly in parallel). The second option requires the use of several electronic components, but the capacitance can be reduced four-folds. An increase in the capacitance leads to a reduction in the voltage signal at the output since the charge produced by the SiPMs is constant. Therefore, in the interest of obtaining a large output signal, it was decided to use individual op-amps for each SiPM array. The anode signals from each array were routed through four individual LMV861 op-amps from Texas Instruments and then summed together at the end before being available for signal readout. All the op-amps were powered using a +3.3 V supply. Fig. 38 shows the schematic of the custom-designed Stilbene – $CeBr_3$ readout board at Oregon State University.

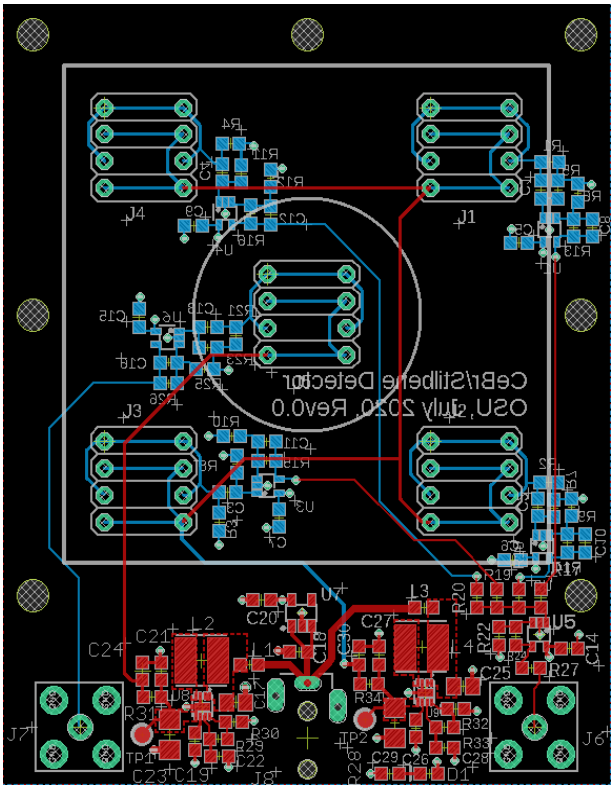

Fig. 38. Eagle layout of the Stilbene-$CeBr_3$ PCB for signal readout

3.1.2 Strontium Iodide [$SrI_2(Eu)$]

The strontium iodide used for this research was grown and assembled by CapeSym Inc. This crystal was doped with 5% Eu^{2+} to maximize the photon light yield [100]. This material is known for its exceptional light yield (one of the brightest) and high energy resolution. With its high density, effective atomic number, depth independent response (compared to CZTs), and absence of intrinsic radioactivity, $SrI_2(Eu)$ are very well suited for our application. There are some observable downsides for this material as well, such as long decay time between 1-5 µs. This long decay time limits the use of this scintillator in high count rate situations but in the case of radioxenon detection systems where the number of counts is relatively low, $SrI_2(Eu)$ can be successfully used. Some other challenges with using this material are its hygroscopic nature, which is the reason it was decided to encapsulate the crystal using light and airtight epoxy. PTFE reflectors are used to cover all the surfaces of the crystal except the area for photon readout. Since this detector is designed to function in a laboratory environment and is not intended to be moved much after placing the detector in the holder, the

problems of the hygroscopic nature of the crystal is not much of an issue because the epoxy is intended to hold its integrity in such an environment.

Taking the compact nature of the detectors into consideration, it was decided to explore the option of using SiPMs for photon readout. The literature was studied to check the compatibility of SiPMs with $SrI_2(Eu)$, some reports suggested that there was no observable decrease in the energy resolution while other studies indicated that there was a change from 3.4% to 4.4% for the 662 keV peak from ^{137}Cs [118]. One possible concern with using SiPMs is saturation because of the very bright nature of the scintillator. The long decay time of the scintillator (between 1-5 µs) helps solve this problem because these photons are distributed over a relatively long time thereby preventing saturation. The next point of interest is the number and locations of the SiPMs. The idea is to employ a minimum number of SiPMs to collect the photons. The linear additive nature of the SiPMs prohibits the use of extensive arrays in parallel. Therefore, it was decided to machine the top of the cylindrical ingot to accommodate the SiPMs. This D-shaped scintillator allows us to accommodate two J-series SensL SiPMs at the top. Two such scintillators are employed for increased photon detection efficiency. Fig. 39a and Fig. 39b shows the sketch of the $SrI_2(Eu)$ detector and the $SrI_2(Eu)$ crystal inside the encapsulation respectively.

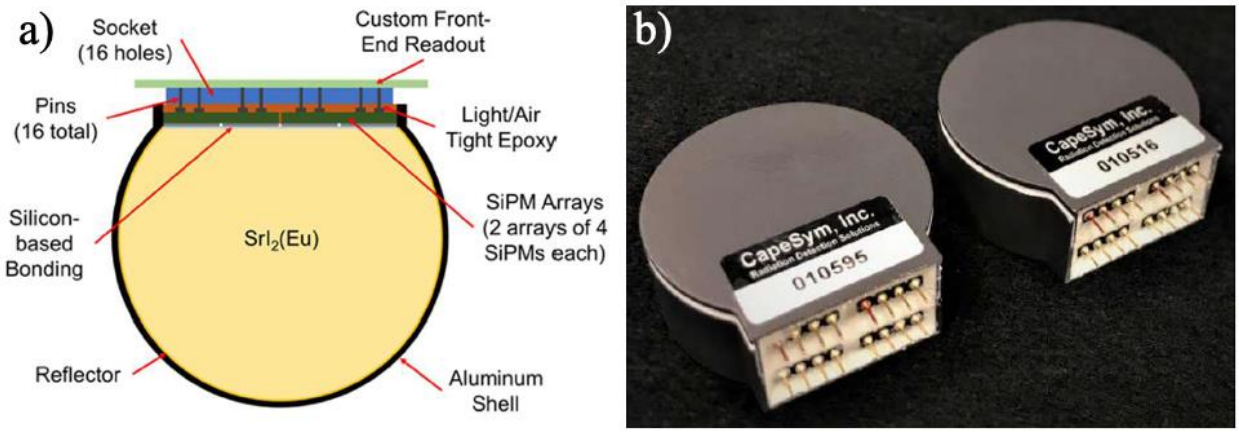

Fig. 39. a) schematic of the $SrI_2(Eu)$ detector showing the reflector, Aluminum casing and SiPM readout; b) the assembled $SrI_2(Eu)$ photon detectors with mounted SiPMs

Each SrI_2(Eu) detector was read by two SensL Array-J 60035-4P-PCB SiPM arrays. These arrays were permanently mounted on the crystal surface to improve light collection efficiency and energy resolution. The SrI_2(Eu) scintillator peaks at about 420 nm which is well suited for the J-Series SiPMs and also has a peak sensitivity at about 420 nm. Each scintillator measures 38.11 mm in diameter and is 12.7 mm thick. The entire crystal is wrapped in a PTFE reflector except the region meant for optical photon readout. A 0.5 mm thick aluminum casing was used to prevent moisture uptake since SrI_2(Eu) is hygroscopic in nature. Epoxy was used to further enhance the light/ airtightness of the scintillator and prevent external optical photons from interacting with the active area of the scintillator from beneath the SiPM array. The anode and cathode pins of the SiPM are the only components that protrude from the epoxy, this was done to enable biasing of the SiPMs and signal readout from the anode. A 9-pin Dual-in-line (DIL) female socket connector was employed as a connection between the SiPM pins and the PCB board for signal processing.

On the PCB front, a custom board was designed at Oregon State University to enable the front-end analog processing of the pulses from the SiPMs. A male 2.35 x 0.7 mm plug was used to power the board using a +5V power supply. A stepping regulator in the form of an LT8410 was used to step the voltage from +5V to +27.5V to power the SiPMs. A Cremat Inc. charge sensitive preamplifier (CSP) with a time constant of 50 µs was used onboard to integrate the charge from the scintillator [130]. Since the scintillator has a decay time between 1 and 5 µs, using a preamplifier with about 10 times the scintillator decay time is more than sufficient to integrate all the charge that is generated. Initially, the digital integration method was tried but the 30 keV peak was not successfully separated from noise which prompted the investigation of the Analog Integration board. It must be pointed out that while using a CSP, the decay time of the pulse is dependent on the electronics being used (RC of the preamplifier) rather than the decay time of the scintillator. The rise time of the pulse was noted to be about 11 µs, it is worth mentioning that the trapezoidal flat-top time should be around 11 µs to capture the full energy deposition of the pulse. The pulse output is initially read by an MMCX-BNC connector after which a BNC-MMCX connector is used to route the

signal to the digital pulse processor. Fig. 40 shows the schematic of the Cremat readout board used for the $SrI_2(Eu)$ detectors.

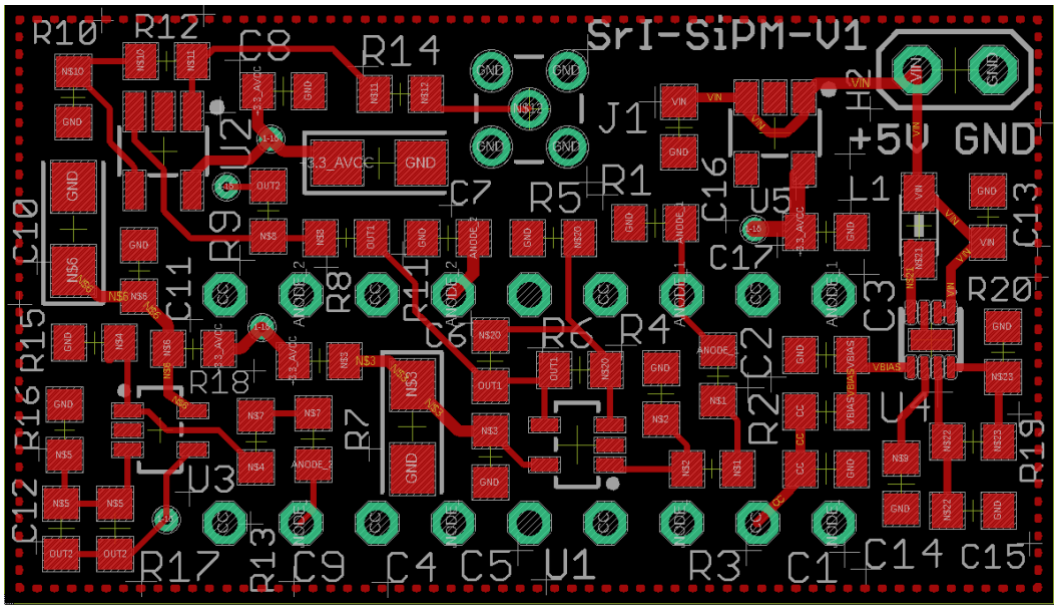

Fig. 40. The Eagle layout of the Cremat board for the $SrI_2(Eu)$ detector data readout

3.1.3 Stilbene Gas Cell

Stilbene was used to function in the capacity of a gas cell as well as an electron detector. Stilbene is one of the materials which is a hydrocarbon from an atomic standpoint but features a crystalline structure, just like inorganic scintillators. This is especially useful in achieving two orders of magnitude reduction in the memory effect compared to plastic scintillators. These features in conjunction with the fact that stilbene has a better conversion electron energy resolution compared to plastic scintillators (about 15%) make it an ideal candidate for this research.

The gas cell is 21.7 mm in height and has an external diameter of 18.7 mm with a wall thickness of 1.8 mm. The total internal volume of the gas cell is about 3.17 cm^3. The stilbene gas cell is made up of three parts, the main body, and two end caps, all made of stilbene. A 0.6 mm diameter hole is drilled on the top end cap to accommodate the gas injection tube. A nylon barb is attached to the top cap to act as a connection between

the stilbene gas cell and the plastic injection tube. A 3-way Luer lock is attached on the other end of the plastic tube to enable gas injection and extracting the gas after measurements are completed using a roughing pump.

In the previous Stilbene-CZT design, the photons from the gas cell were read by an array of 3x3 SensL J-Series SiPMs. In the current research, the stilbene gas cell is only being read by a 2x2 SensL J-series array. This presents a problem with regards to light loss, there is an abundance of stilbene surface through which optical photons can be sensed but is limited by the size of the 2x2 array. To remedy this, it was decided to paint the outside edge of the stilbene gas cell with reflective paint. The stilbene gas cell manufacturer (Inrad Optics) was contacted to apply white reflective paint on the outside edge of the detection surface to reduce the active area through which optical photons might escape. Fig. 41 shows an image of the detection surface of the gas cell with the reflective paint.

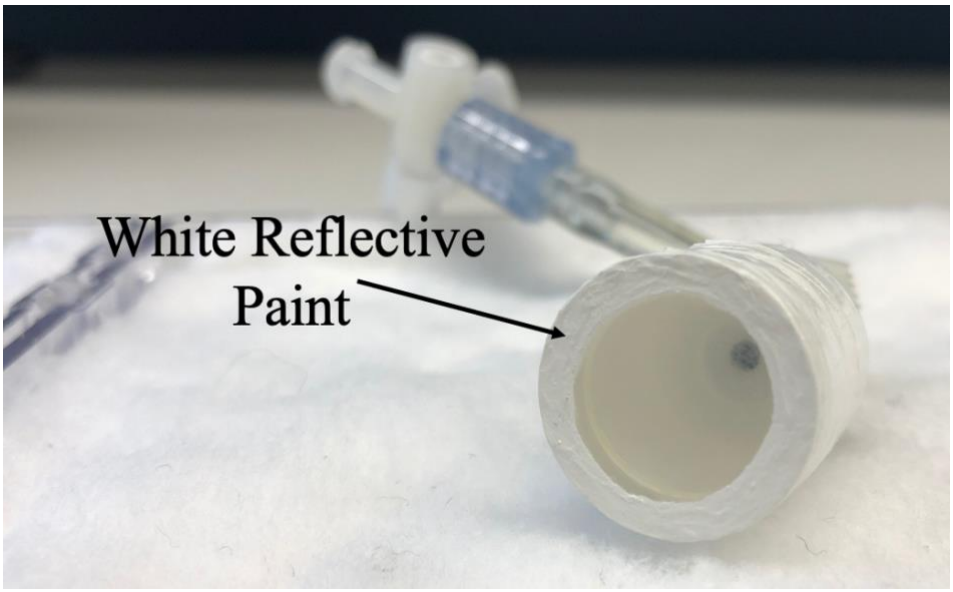

Fig. 41. The detection surface of the stilbene gas cell and the white reflective paint to increase light collection efficiency

3.1.4 Digital Pulse Processor and Coincidence Identification

For the radioxenon detection system to function successfully, the pulse processing and coincidence identification module is equally important. In this section, we shall be looking at the various aspects of the digital pulse processor/ MATLAB user interface and the coincidence identification methods.

The 8-channel digital pulse processor was designed and developed at Oregon State University. This is an upgrade to the previously used 2 channel digital pulse processor. The DPP8 was designed to process signals from eight detection bodies in real-time. The board was designed to operate in either singles mode or in coincidence mode where the user can define the channels between which they would like to observe coincidence events. The processor is powered by a +5V DC power supply. The processor in essence is a combination of 2 PCBs. The top board is responsible for converting the pulses from analog domain to digital domain using an ADC clocking at 125 MHz (8 ns sampling period) with 14-bit vertical resolution. Once the signals have been converted to the digital domain, these signals are then routed through the commercially available Opal Kelly board [168]. This board features a Xilinx Kintex-7 FPGA, a USB interface, and a cooling fan. Opal Kelly also provides a VHDL-MATLAB API interface through which the MATLAB and FPGA can communicate. The block diagram of the interface between Opal Kelly and the PC is shown in Fig. 42. The DPP8 is shown in Fig. 43 along with some important components on board.

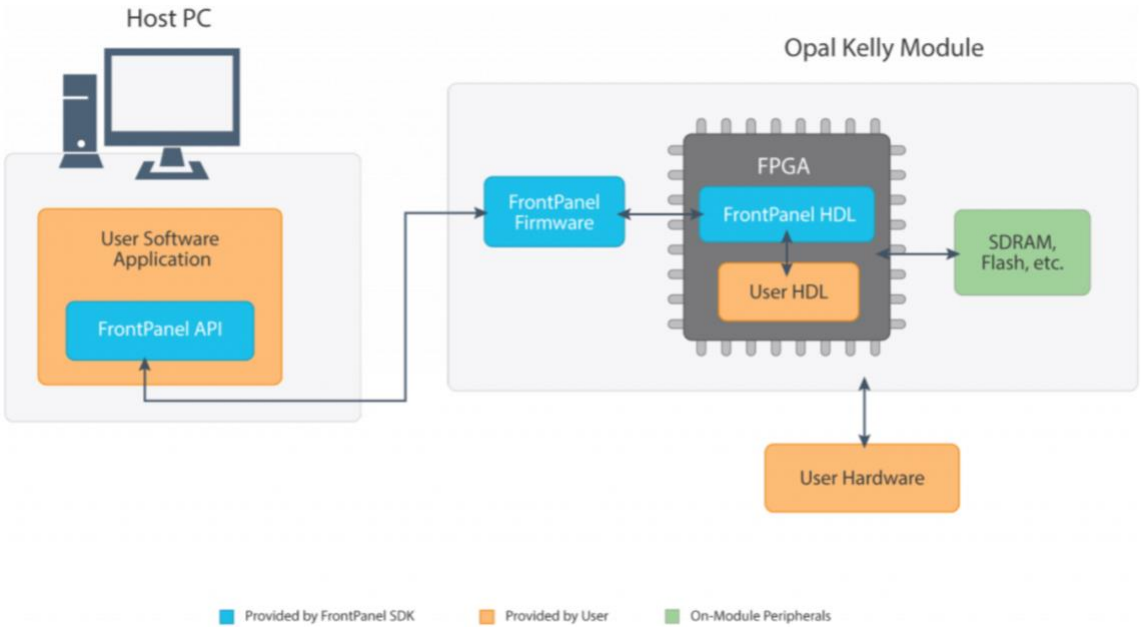

Fig. 42. Block Diagram of the connection between the Opal Kelly module and the Host PC

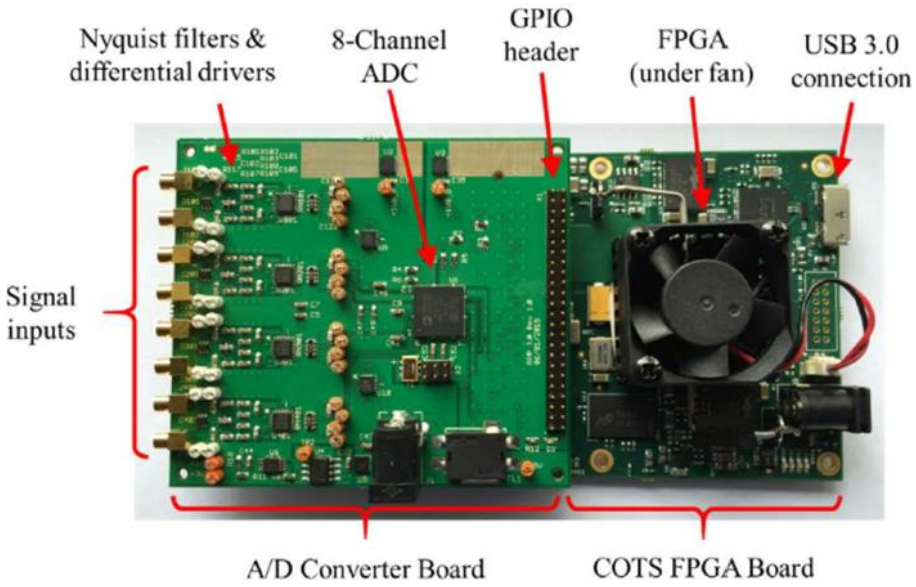

Fig. 43. The eight-channel digital pulse processor illustrating some of the important onboard components

In this work, there were two $SrI_2(Eu)$ detection bodies acting in the capacity of photon detectors and one stilbene gas cell acting in the capacity of an electron detector. Therefore, for this project, three of the eight channels were put to use. The user, in the

MATLAB interface, has an option of choosing the channels they are interested in monitoring and also mention the trigger filter parameters for each channel [170]. This is one of the major improvements over the DPP2 where the user has the flexibility of changing the filter coefficients on the fly in MATLAB rather than synthesizing a new bit file altogether. When the trigger filter output exceeds the user-defined threshold, the leading-edge trigger produces a one-clock high pulse after which the FPGA begins capturing the pulse data. The user has the option of delaying the pulse capture for a given number of samples (this is generally done to compute the baseline). After valid pulses have been captured, the FPGA transfers this pulse data to the MATLAB user interface for further processing.

There are many parameters that can be set using the MATLAB user interface such as the coincidence time window, trigger threshold, trigger filter coefficients, coincidence channels of interest, and the pulse delay. The only parameter which can't be set in the DPP8 compared to the DPP2 is the gain of the pulse. It is worth mentioning that there are several features like trigger filter parameters and pulse delay which cannot be set using the MATLAB user interface in the DPP2 but are available in the DPP8. Overall, the DPP8 offers more features compared to the DPP2 in terms of overall pulse processing.

In the DPP2, since there were only two channels available, a coincidence event would involve both those channels. In the case of the DPP8, there are 8 channels, and a coincidence event might involve any of those channels. In our case, a coincidence event might involve a valid trigger between Stilbene-SrI_2(Eu)-1, Stilbene- SrI_2(Eu)-2, and Stilbene- SrI_2(Eu)-1- SrI_2(Eu)-2 (triple coincidence). In the first two cases, where only a single SrI_2(Eu) is involved, both these pulse data would be transferred to the MATLAB user interface for amplitude determination and plotting the 2-D spectra. In case there is a triple coincidence detected, the pulse data of all three-detection media would be transferred to the MATLAB user interface and amplitude determination would be carried out for the respective channels. In the end, the amplitude of both the SrI_2(Eu) detectors would be added to obtain a summed energy deposition in the photon

detection media. This summed energy would be plotted in conjunction with the electron media energy deposition.

In the FPGA space, this logic is implemented using an 8-bit binary pattern matching, where “1” means channels of interest and “0” means channel, not of interest. For example, if the user is interested in a coincidence event between channel 3 and channel 7, the binary pattern would read “01000100”, where the least significant bit represents the first channel while the most significant bit represents the eighth channel. For example, let’s suppose the user has requested a coincidence event between channel 7 and channel 3. If channel 3 (or channel 7) triggers first, the FPGA starts a clock and will wait till the user-defined coincidence time window (CTW) elapses for the second channel to trigger. If both the channels trigger within the set timeframe, the FPGA tags these events as a coincidence event and pushes both the pulse data to the MATLAB user interface for further processing. In case, only one of those channel triggers within the CTW, the FPGA tags these events as single events and starts looking for valid triggers all over again.

3.1.5 **Detector Holder**

The detector holder plays an integral part in holding the detector together at the right place and also ensures that it is mechanically stable. Although we are testing this detection system in a lab environment where extensive mobility is not expected after assembling the detector, it is still beneficial to design a holder that can keep the detection elements stable and restrict unwanted movements. The detector holder was designed in SolidWorks and printed using the Ultimaker S3 3-D printer in the radiation detection lab at Oregon State University [171]. There were a couple of design philosophies that were followed to obtain the best results. Apart from holding the detector components in place, the holder also had the task of optically isolating the stilbene SiPM, therefore it was decided to use black PLA to minimize optical photon reflection. In addition to this, it was also decided to use at least 2mm thick design features like the external walls to maintain the mechanical integrity of the holder.

Since this detector uses the board initially designed for the stilbene-$CeBr_3$ for reading the anode signals from the stilbene SiPM array and the two $SrI_2(Eu)$ for detecting photon signatures, it was decided to use a single holder for accommodating both the Stilbene and $SrI_2(Eu)$ detectors. Arithmetic calculations were performed beforehand to ensure that the centers of the stilbene and $SrI_2(Eu)$ detectors align to maximize efficiency. The buckets for holding the $SrI_2(Eu)$ were designed keeping the same design philosophy in mind. To ensure that the $SrI_2(Eu)$ detectors are properly in place, a top cap for the $SrI_2(Eu)$ detector was designed which prevents any rotation along the radial direction. To prevent motion along the axial direction, a small lip was designed at the edge of the holder which prevents the motion of the detection media in the forward direction. All these steps ensure that once the $SrI_2(Eu)$ detectors are in place, their movement is restricted in all directions. Fig. 44 shows an image of the stilbene-$SrI_2(Eu)$ holder mounted on top of the readout board.

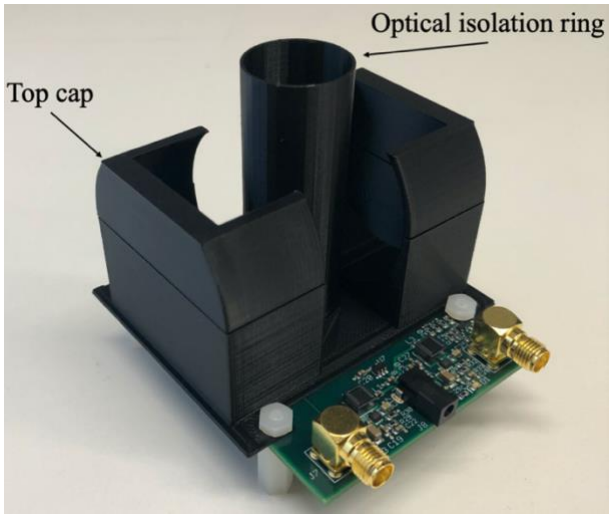

Fig. 44. The Stilbene-$SrI_2(Eu)$ detector holder illustrating the optical isolation ring and the top cap for holding the detection elements in place

The same aluminum box that was used for the PIPS-$SrI_2(Eu)$ detector was used for this project. It must be pointed out that some elementary changes were required to be made to the configuration to make accommodations for the custom PCB. The PIPSBox required support on one end of the injection tube which required the machining of a hole on one of the sides, the same hole is currently being used to route the stilbene

signal from the board which was initially designed for the stilbene- $CeBr_3$ detection system. Additionally, a 2.35 x 0.7 mm plug was connected to the common power supply for the two $SrI_2(Eu)$ detectors to power the stilbene SiPMs. The PIPSBox connectors were further removed from the side of the Aluminum box and black electrical tape was used to prevent any external photons from entering. It is brought to the reader's attention that after the SMA connection was made for reading the stilbene SiPM signal, the additional area in the inject tube hole was covered using black electrical tape to maintain optical integrity. Fig. 45 illustrates the assembled system with the $SrI_2(Eu)$, and Stilbene detectors mounted on the board along with the DC power supply and pulse readout.

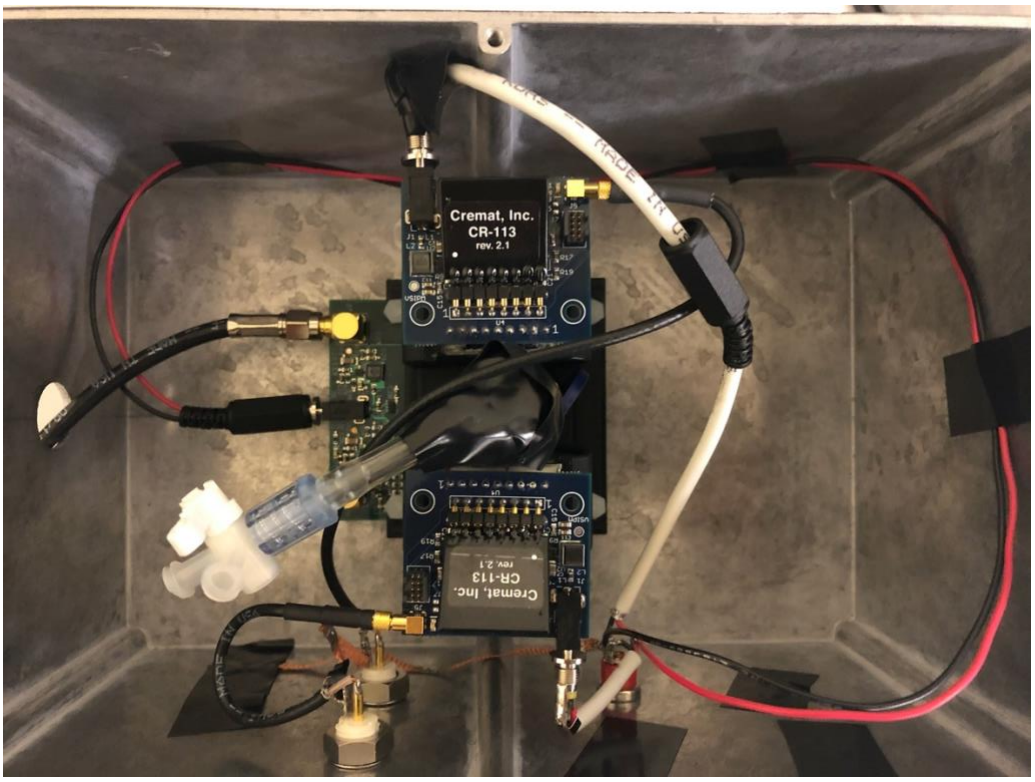

Fig. 45. The Stilbene-$SrI_2(Eu)$ detection system inside the Aluminum box along with all the power supplies and the signal readout

3.1.6 Power Supply and Vacuum Pump

The final components of the detection system are the power supply and the vacuum pump. The +5V power supply is used to power the Stilbene SiPM and the two $SrI_2(Eu)$

SiPMs. The +5V is stepped up to +27.5V using the LT8410 stepping regulator. It was decided to use a single power supply for all the components in the electronics to prevent any complications arising from ground loops. One possible option is to connect all the power supplies to a common ground, but this option was not preferred since all the power supplies required for the detector were +27.5V. The DPP8 also accepts a +5V supply but it was decided to use a separate power supply since it was much easier to route the power cord through a wall plug rather than powering it using a wire from the detector.

The vacuum pump also plays an instrumental role in the functioning of the radioxenon detection system. Previously a hand pump was used to create a vacuum in the detectors, the same hand pump was used for evaluating the memory effect of the PIPSBox. The results obtained did not show a significant decrease in the memory effect when compared to the plastic scintillator. Research performed by other research groups has indicated that using the PIPSBox, significant improvements in memory effect have been observed. This led to the use of a roughing/ turbopump since similar equipment was being used by other research groups as well. Welch Duo-Seal 1400(B-01) roughing pump was used to achieve a vacuum in the gas cell. It was decided to also use a digital gauge to monitor the pressures being achieved and, in the process, Inrad Optics, the manufacturer of the stilbene gas cell was also consulted to ensure that the cell can maintain mechanical stability without rupturing at 2-3 torr. The exhaust from the pump was directly released in a fume hood to ensure that no radioactive gas reaches the ambient air. Although an electrical pump was being used, there have been instances of occasional drops in pressure due to inevitable leakage in the pipes.

3.2 Simulation Work

Performing simulations play an important role in estimating the performance of the detection system. Therefore, two such codes have been put to use to analyze the detection performance and the optical photon distribution using MCNP and Geant4 respectively. Additionally, the PTRAC card has been used in MCNP to extract

additional history level interaction with the detector bodies of interest. This section provides a brief description of the simulation work performed in this project.

3.2.1 MCNP and PTRAC

Monte Carlo N-Particle Transport code (MCNP) is a general-purpose particle/ photon transport code written in Fortran and was developed by Los Alamos National Laboratory (LANL) [172]. This code provides the freedom to model several user-defined geometries and source definitions that are used in a wide array of applications (reactor design, medical imaging, radiation detection, etc.). In this work, the detector geometries were modeled in MCNP and an f8 tally was performed for all the radiation and detection media of interest. An f8 tally is performed over a detection body which provides the histogram of the energy deposition of a given radiation type for a set number of particles, often referred to as histories. These simulations are often used in understanding the efficacy of the system in terms of detection efficiency. The user is required to define all the cells in the simulation followed by the respective density and the surface numbers bounding the volumes. After which the user defines the source geometry and the type of radiation being simulated. This is where the user specifies if the radiation being simulated is a neutron, electron, or photon. Source histograms can also be mentioned at this place (this feature is especially useful for beta spectra). As far as the source geometry goes, the user can define a simple point source or a complex mix of multiple sources to be simulated. In the end, the user mentions the type of tally being performed (in our case an f8 tally) and the histogram parameters like the number of bins followed by the threshold of the histogram. It is often recommended to have a relatively low threshold to account for events that undergo no interaction/ deposit very low energy in the detection medium.

On the PTRAC front, all radiation of interest has been simulated, using the PTRAC card enables the user to track each interaction of the radiation of interest. For example, if we are simulating an electron, the PTRAC card records each interaction of the electron with the body, surfaces crossed, type of interaction, and energy deposited in each interaction. This history-wise data that is obtained is synonymous with obtaining

the individual pulse data based on which the spectrum is constructed. Spectral broadening can be achieved using the script used for plotting the spectrum. In the case of a simple geometry like the Stilbene-SrI_2(Eu) detection system, where there is a single electron detection body with near 4π detection efficiency, there is no need to exclude any geometries from the PTRAC simulation. Sometimes the complexities of the simulation demand the exclusion of some detection bodies in the interest of reducing the size of the output file. For this research work, both PTRAC simulations as well as f8 tallies were performed to evaluate the performance of the detection system. A custom-built script was used to parse through the PTRAC file to extract energy information and also identify coincidence events. Each history in the PTRAC file contains a particle number, if there is a match between the particle number between the electron and photon deck for a certain coincidence mechanism, the python code records this event as a coincidence event. This coincidence data is then read by MATLAB where spectra broadening is implemented, and 2-D spectra plotting is performed.

3.2.2 Geant4 and DETECT2000 Simulations

Geant4 stands for **Ge**ometry **a**nd **T**racking 4, this is an open-source C++ based particle transport code developed by CERN initially for the Large Hadron Collider (LHC) experiment. After about two decades of usage, there are currently multiple communities and code versions that are specialized in performing certain kinds of simulations (medical, space, sub-surface, radiation detection, etc.). In our application, the $CeBr_3$ detection system was simulated to observe the optical photon distribution at the locations where SiPMs were present. Several reflection models and surfaces were used to study their effect. Experimental reflection Look Up Table (LUT) values were also incorporated in the simulations to obtain realistic results. There was also a comparison made between a specular and a diffused reflector on the photon distribution on the SiPMs. As part of the simulation, the $CeBr_3$ detector geometry was built in Geant4 using the properties of the detector like density and photon light yield. Radiation photons were generated in the source volume mimicking the geometry of the stilbene gas cell. Reflective material was used for the external surface of the detector to maintain high reflectivity. The Geant4 code has multiple header files and their corresponding

source code files. Care should also be exercised while working in Geant4 because there are many different methods that can be used to achieve the same result. Data recording was performed by printing out the termination coordinates of the optical photons in the SiPMs. This data is then subsequently loaded in a MATLAB script to plot the photon distribution in the SiPMs. It must be pointed out to the reader that Geant4 offers extensive optimization and customization options in terms of particle termination or extracting the type of data for a given interaction like the angle of incidence, location of termination, etc. Fig. 46a shows the Geant4 simulation of the detector body with the reflector material indicated in green, the SiPMs indicated in white, and the detection crystal shown in yellow. Fig. 46b shows the optical photons being transported through the detection body.

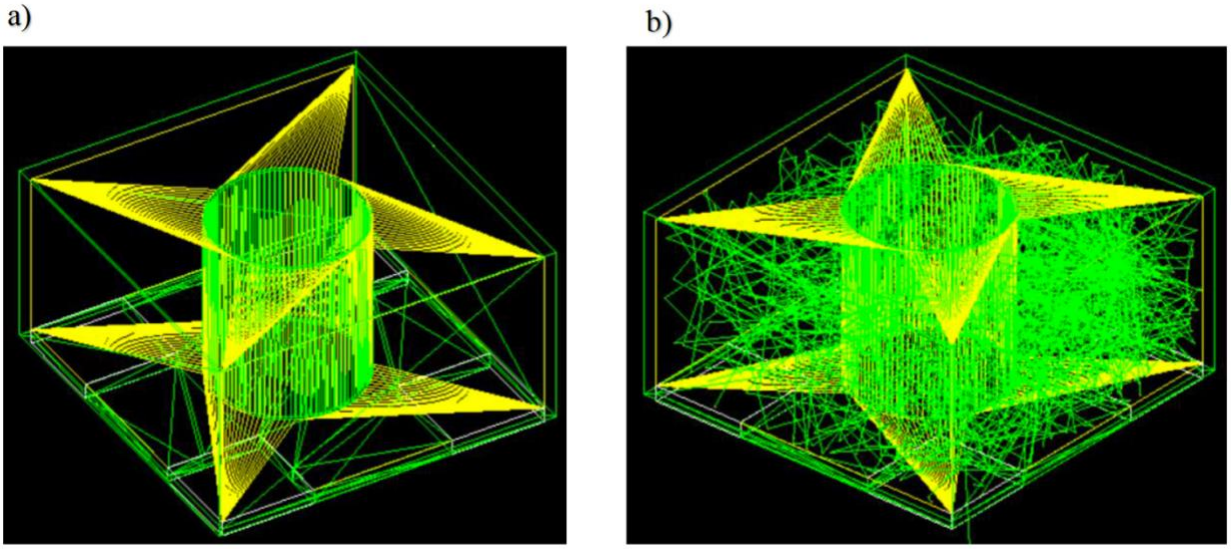

Fig. 46. a) 3-D rendering of the detector in the Geant4 visualizer; b) optical photons being transported in the detector volume

Simulations were also performed using DETECT2000, an optical transport code. This is similar to MCNP where the scintillator geometry is constructed along with some basic details like the refractive index and the optical photon wavelength of interest. DETECT2000 is purely an optical photon transport which is one of the major points of differentiation between Geant4 and DETECT2000. Geant4 on the other hand is equipped to handle both the ionization radiation, the subsequent optical photon generation, and transport through the geometry of the scintillator. In this toolkit, the

user builds the optical transport geometry followed by defining the volume of photon generation. This is the major point of differentiation between Geant4 and DETECT2000, in the former the optical photons are generated based on the location of ionizing photon interaction whereas, in the latter, this is predefined by the user. This difference can be especially pronounced when low energy ionizing photons are involved which interact close to the detection surface as opposed to high energy ionizing photons which produce optical photons at a relatively larger depth than low energy photons. Therefore, the point of origination is different based on the energy of the ionizing photons, this difference can be successfully accounted for in Geant4 but not feasible in DETECT2000. In DETECT2000, there is an option of tracking the history of each photon by using the FATES command. This provides the user with the start and end coordinates of the photons. This data is then read by a MATLAB script to plot the photon distribution at the location of interest. The point of this exercise was to arrive at a conclusion if there are any observable differences between the results obtained from Geant4 and DETECT2000. The working theory is that, since the geometry planned to be simulated are not extremely complicated as opposed to other systems involving light guides, large volumes, etc. Therefore, the differences between the photon distribution for Geant4 and DETECT2000 is expected to be minimal. This is further supported by the fact that the scintillator material in question has a relatively high photon light yield, therefore even for a low energy deposition, there will be a significant number of optical photons that will be produced and transported through the scintillator volume.

3.3 Experimental Work

Before starting the xenon measurements, it was required to evaluate the performance of the stilbene gas cell, individual $SrI_2(Eu)$ detectors, and the combined detector performance. To perform this task, it was decided to mostly use a ^{137}Cs source because of its relatively long half-life of about 30 years, relatively high energy photon, and quick availability. On some occasions, it was also decided to use the low energy variable energy X-ray source to evaluate the photon detectors. After both the detectors were individually calibrated and characterized it was decided to check the coincidence

module using the ^{137}Cs source. After this, the response from individual xenon isotopes of interest (^{131m}Xe, $^{133/133m}$Xe, and ^{135}Xe) were recorded and evaluated.

3.3.1 Evaluating the SrI_2(Eu) Detector

There were multiple tests conducted to evaluate the performance of the SrI_2(Eu) detector, it is brought to the reader's attention that although most of these tests were performed previously for another project it was required to perform these tests again to observe and assess any changes. The list of experiments is provided below:

- Calibration using ^{137}Cs and other check sources
- Energy threshold testing using a variable energy X-ray source
- Backscatter coincidence between the two SrI_2(Eu) detectors using ^{137}Cs

3.3.2 Evaluating the Stilbene Gas Cell

The stilbene gas cell in this system was used in the capacity of an electron detector. Although this detector was previously used for the Stilbene- CZT detection system, some basic testing was done on the detector which includes:

- Efficacy of the optical isolation ring in presence of ambient lighting
- Preliminary calibration using a ^{137}Cs source
- Optimize the filter for the stilbene detector using the 129 keV CE for ideal performance

3.3.3 Other Testing

Apart from the ones identified above, there were a couple of more tests that were performed to ensure the functioning of the electronics and the detectors. A dual-channel pulse generator was used to test the efficacy of the coincidence identification module. This was achieved by programming a delay between the two signals and setting the coincidence time window to a little over the delay and observing the number of pulses. Other tests include the noise evaluation using the DPP2 and DPP8, this was done to test for any spectral broadening that might be introduced because of the processing electronics.

3.3.4 Complete System Characterization

Once each detector and the coincidence module were tested, the next step is to characterize the entire detection system using lab check sources. This is performed as a final step before injecting xenon samples. For this work, it was decided to use a ^{137}Cs source and record backscatter coincidence between the stilbene and the $SrI_2(Eu)$ detectors. The coincidence module was set such that the coincidence events between either of the photon detectors and the electron detector were recorded. On top of that, coincidence events between all the three detectors were also set to be recorded. It must however be pointed out that the probability of such an event being recorded is extremely low.

3.3.4.1 Xenon Sample Preparation

Radioxenon used in this work is produced by irradiating ultra-pure samples (~99.99%) of xenon isotopes (^{130}Xe, ^{132}Xe, and ^{134}Xe) in the Oregon State University TRIGA reactor. These gas samples were purchased in the late 2000s and early 2010s. These cylinders were initially at air pressure when they were purchased but with eventual use, there is a significant pressure drop. Over the years, there have also been instances of accidental valve openings which has led to ambient air entering the cylinders. Although ambient air is present in the sample it doesn't present itself as a challenge because the amounts of xenon gas required for substantial counts to be recorded by the system are relatively low.

For loading the sample, a polystyrene syringe is used (generally between 3 and 5 ml). This is connected to the xenon cylinder and a hand pump is also connected to create a vacuum in the plastic tubing. After this, the gas valve is opened, and a stable xenon sample is drawn into the syringe. This syringe is then irradiated in the thermal column at a thermal neutron flux of about 7×10^{10} neutrons per cm^2 per second for a duration of about 7 hours in the Oregon State University TRIGA reactor. After this, the xenon samples are injected into the stilbene gas cell one after the other. Again, a hand pump is used to create a vacuum in the stilbene gas cell following which the radioxenon is injected. Fig. 47 shows the gas sample being loaded into the syringe. Care has been

exercised to ensure that relatively small amounts of samples are irradiated to ensure minimal pileup in the detection system. It must however be pointed out that in certain cases when the count rate was really high, it was decided to wait for the activity to drop before data acquisition.

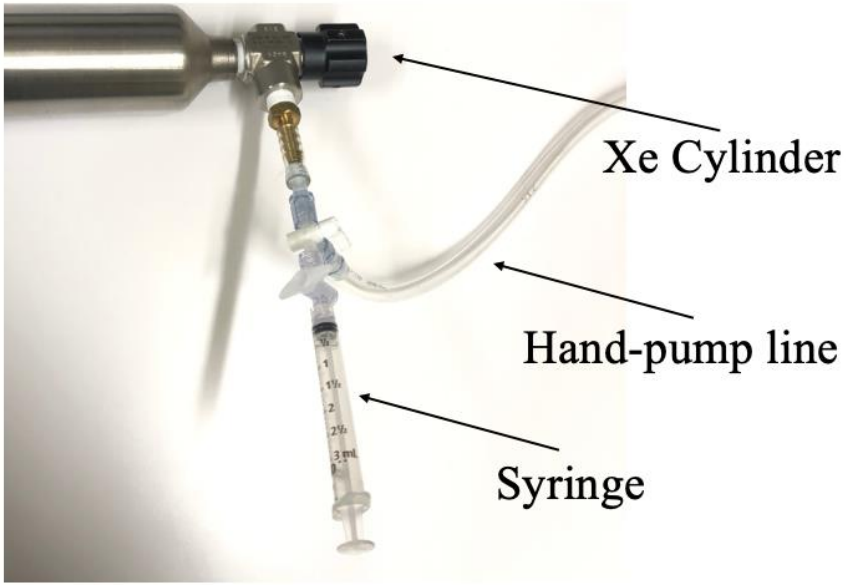

Fig. 47. Illustration of the xenon gas being loaded in the syringe for irradiation in the OSU TRIGA reactor thermal column

3.3.4.2 Absolute Efficiency for MDC Calculations

The MDC of a radioxenon detection system, which is a sensitivity parameter of the detector is important during the evaluation of the detector. An important parameter in the MDC calculations is the efficiencies of the electron and photon detection system. For obtaining this number, there are one of three ways, either MCNP simulations can be performed to obtain this data, or two equal samples can be prepared, and one sample can be injected into a well-characterized detector while the other sample can be injected into the detector whose efficiencies are unknown. The third option is to use a relative method, where based on the electron/ photon singles and the coincidence counts, the efficiencies of each of the energy of interest can be obtained.

Using the first option, it has been shown that there is sometimes a significant difference between the efficiencies obtained from simulations and those calculated using experiments. These can be partially from the unknown geometry of the detector internals (for example the variance in the thickness of encapsulation material). It has also been observed in some cases that the peak to total ratio is quite different between experimental and simulation results. This might result from variable Gaussian Energy Broadening parameters used in simulations compared to experimental work. These differences are sometimes more pronounced at low energies. The second option is to use two samples of equal activity and inject them into two different detectors. Although this method works in theory, there are several complications in implementing this method. Accurately monitoring the amount of gas drawn from the cylinder is a challenge that is required to be overcome. Other challenges include maintaining the same thermal neutron flux for both the gas samples, this is something that can't be effectively monitored. The third challenge identified in using this method is having an accurate knowledge of the volumes of the gas cell internals and the tubing used to transfer the gas, this factor affects the amount of gas that actually enters the gas cell once the radioxenon is injected after creating a vacuum in the system.

Therefore, to avoid these challenges it was decided to pursue the third method of calculating the absolute efficiency. This method was described in detail by Cooper et.al. By following this method, the user is only required to create a single sample of radioxenon and moreover, the knowledge of the activity of the sample is not required to be known beforehand. The quantities of interest in this method are the singles electron/ photon count rate and the coincidence count rates. There are some simplifications that are made for this work such as assuming the 129 and 199 keV have a near 100% detection efficiency, and the electron detection efficiencies obtained from MCNP are taken to be true. These simplifications can be made because of the near 4π solid angle of the Stilbene detector. The three efficiency equations used for this work are as follows [173]:

$$A_T = \frac{C_{\beta\gamma}}{BR_{\beta\gamma}\varepsilon_{\beta\gamma}} = \frac{C_{\beta\gamma}}{BR_{\gamma}\varepsilon_{\beta\gamma}} = \frac{C_{\beta\gamma}}{\varepsilon_{\gamma}\varepsilon_{\beta}BR_{\gamma}} \quad (7)$$

$$A_T = \frac{C_{\gamma}}{\varepsilon_{\gamma}BR_{\gamma}} \quad (8)$$

$$A_T = \frac{C_{\gamma}}{1-(1-\varepsilon_{\beta})\left(1-\varepsilon_{CE_i}BR_{CE_i}\right)} \quad (9)$$

In these equations, A_T represents the total activity of the sample, $C_{\beta\gamma}$, C_{β}, and C_{γ} are the count rates for coincidence, electron singles, and photon singles respectively. In all cases, the branching ratio of beta is assumed to be 100% which results in some additional simplifications. This implies only the branching ratio of the photon is used in the calculations. Observing these equations, it can be inferred that determining the photon efficiency is challenging because we are required to take into account multiple decay paths. Since there were no other methods available to calculate the absolute efficiency, it was determined to use the aforementioned methodology.

4. RESULTS

The following section initially goes into the simulation work that was performed using MCNP and the two optical photon transport codes. This is followed by exploring some of the work that was performed using the $CeBr_3$ detection system. Results from initial characterization using the SrI_2(Eu) and the Stilbene gas cell are then presented followed by the evaluation of the entire radioxenon detector. Lastly results from the xenon injections in the SrI_2(Eu)-Stilbene system is presented along with absolute efficiency calculations and the MDC.

4.1 Simulation Work

In the simulation work section, we shall be looking at the results that were obtained using the MCNP code in terms of the PTRAC card, detection efficiency, and the GEB. These results can be effectively used to perform a comparison between the experimental and simulation data. The sub-section of this work explores the results from the optical transport models that were developed using Geant4 as well as DETECT2000. This is followed by providing a performance comparison between the two codes from a simple scintillator geometry perspective.

4.1.1 Monte Carlo N-Particle (MCNP) Transport Code

MCNP is a deterministic transport code that is widely used for several applications for the general transport of particles/ photons through matter. For our application, MCNP was extensively used for the estimation of detection efficiencies for various photon energies and the spectral broadening of the peaks at various energies to estimate the peak to total ratio. For our simulation, the Stilbene cell, the PTFE reflective tape, the Aluminum external encapsulation, and any void spaces like the inject hole were modeled. Volumes that were not covered by either of the materials were assumed to be a vacuum with an electron and photon importance set to unity. The density of the gas was taken to be ~4.5×10^{-3} kg/m^3, this value was calculated based on a conservative estimate that the injected gas consists of about 70% xenon and 30% nitrogen carrier gas. Having a high density of the gas directly results in a tail for the conversion

electrons while having negligible effect for the photons. There were many parameters that were investigated including the solid angle of the photon detector, MCNP generated spectra, and the simulated efficiencies for the regions of interest.

4.1.1.1 Solid Angle

Solid angle is one of the most important parameters when it comes to estimating the efficiency of the detector. A higher solid angle is generally associated with a higher detection efficiency. It must be pointed out to the reader that; the energy of the particle and the cross-section also play a role in efficiency determination. The solid angle in its most simplified form is the amount of *face* the detection surface is presenting to the source. For example, if we consider a hollow sphere with a photon source at the center of the sphere, all the photons that are emitted by the source are going to interact with the sphere irrespective of the zenith and azimuth angle. In such a case, we call the solid angle to be 4π because all the photons that are being emitted pass through the hollow sphere. While attempting to perform solid angle calculations in MCNP it is always recommended to use high energy photons or reduce the density of all bodies which are not of interest to zero. In this work, the solid angle of the photon and electron detector was of interest. The effect of the cut on top of the photon detector to accommodate the SiPMs was also of great interest.

MCNP simulations indicated that the solid angle of the electron detector was about 3.9π and the solid angle of both the photon detectors combined was estimated to be about 1.64π. If the top cut was not present in the design, the solid angle would have been 1.68π, a not so significant reduction in the photon solid angle in return for the ability to place SiPMs for optical photon readout. This is almost an 8-fold increase compared to the CASP/ stilbene-CZT detector and a 4.5-fold increase compared to the PIPS-CZT design. Although this design falls marginally short in terms of photon detection solid angle compared to the PIPS-SrI_2(Eu) design (1.78π), this is more than compensated for by the near unity electron detection solid angle of the stilbene gas cell.

4.1.1.2 MCNP Spectra

The MCNP transport code was also utilized to generate the simulated spectra from the detection media for various energies and particles of interest. To obtain realistic spectra from the photon detectors it was decided to implement the GEB card in the MCNP deck. For this to be implemented there is a need to know the values of three parameters, a, b, and c. These parameters relate to the FWHM of the peak according to equation 10.

$$FWHM = a + b\sqrt{E + cE^2} \tag{10}$$

Where *a*, *b*, and *c* bear the units MeV, $MeV^{1/2}$, and MeV^{-1} respectively. FWHM is the full-width half maximum of the peak at a given energy in the units of MeV. Therefore, to determine these three parameters there is a need to determine the FWHM of the detector at three different energies. For this work, the FWHM of the SrI_2(Eu) detector at 81, 250, and 662 keV were considered to account for a wide range of energies. Entering the three FWHM equations in a linear equation solver yielded -5.38931e-03, 5.69392e-02, and -4.31743e-01 for *a*, *b*, and *c* respectively. These values were subsequently used for the GEB card in MCNP for the photons. It is worth mentioning that when the FWHM of the 31 keV photon was used in the equation solver it often led to imaginary solutions. For the electron detector, since energy resolution was not available at three distinct energies, it was decided to not use the GEB card. The GEB parameters for plastic scintillators were used based on literature but this did not yield expected results (CE Peak and beta continuum).

Once the MCNP deck was run, the data was read by a MATLAB script and plotted. Since MCNP provides the interactions in each bin not as a number but rather a fraction of the total histories that fall in a particular bin, it was required to multiply this value by an arbitrary number to obtain a whole number rather than a decimal. The photon spectra from 31, 81, and 250 keV X-ray/ gamma are presented in Fig. 48a, Fig. 48b, and Fig. 48c respectively. The 346 keV and 910 keV beta spectra are shown in Fig. 49a

and Fig. 49b, respectively. The spectra from the 45, 129, and 199 keV conversion electrons are shown in Fig. 50a, Fig. 50b, and Fig. 50c respectively.

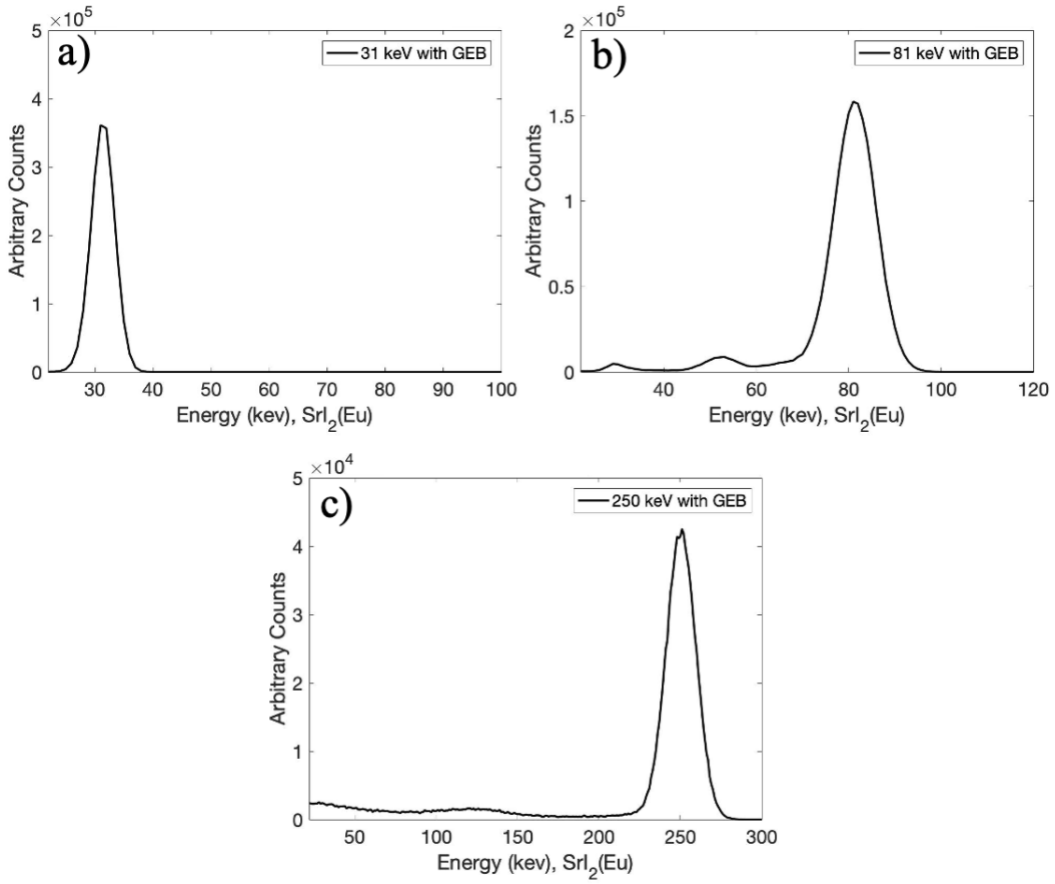

Fig. 48. MCNP generated spectra for the a) 31 keV X-ray; b) 81 keV, and c) 250 keV gamma photon

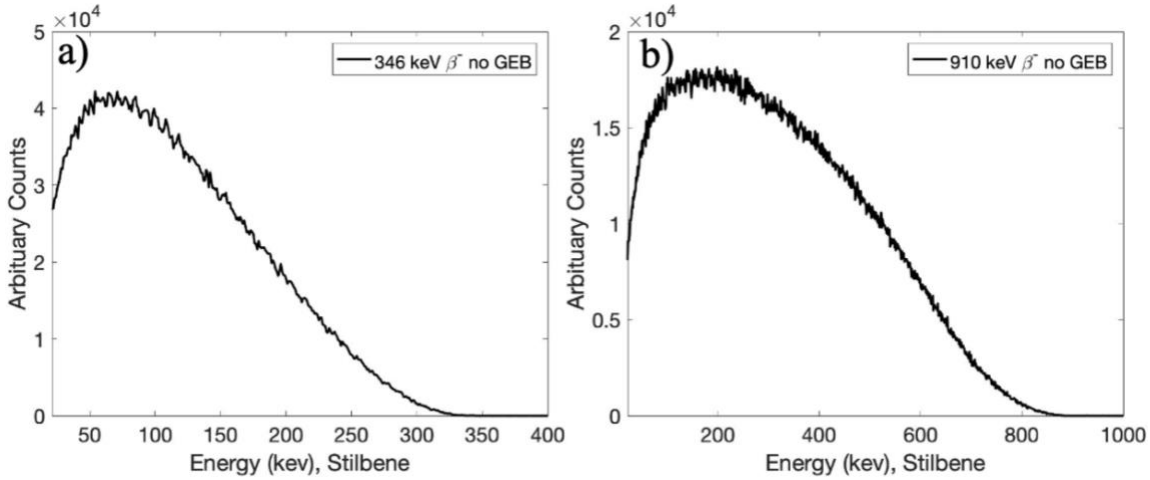

Fig. 49. MCNP generated spectra for the a) 346 keV, and b) 910 keV β_{max}

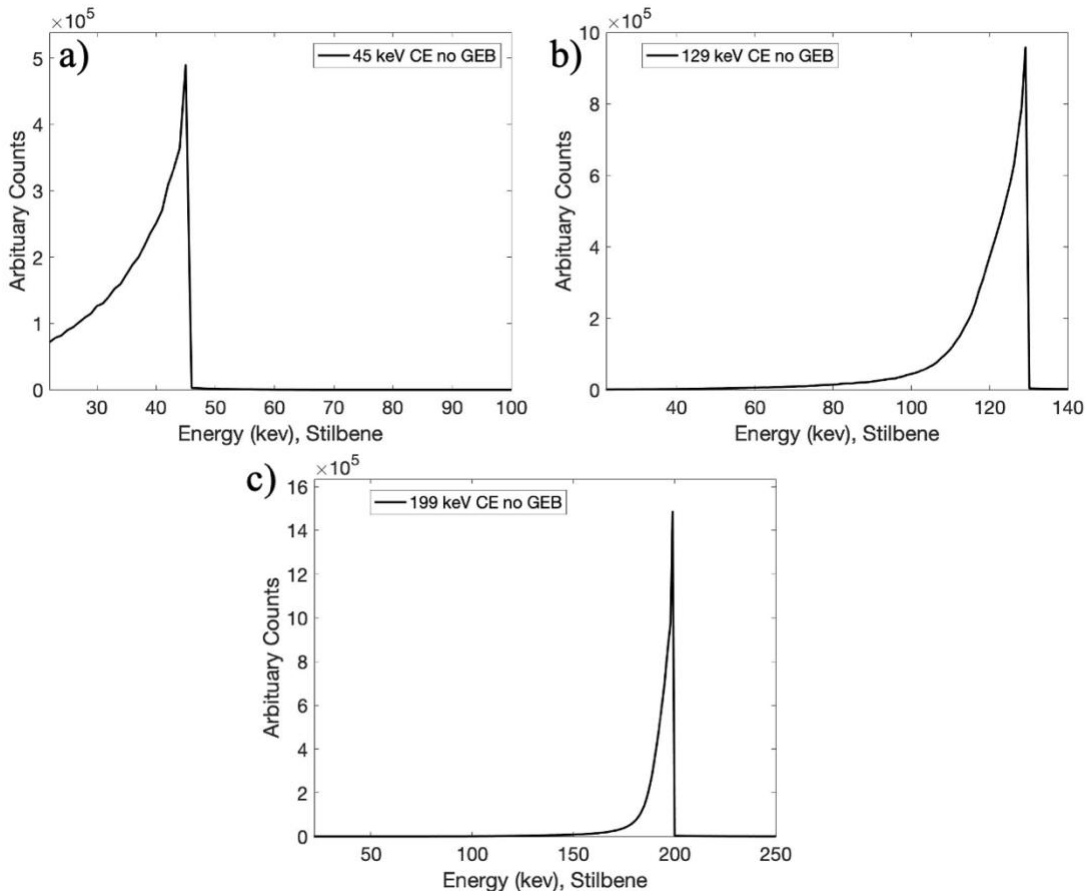

Fig. 50. MCNP generated spectra for the a) 45 keV; b) 129 keV, and c) 199 keV CE

In the photon spectra that were obtained using MCNP, it has been observed that the peaks are symmetric, but the Compton continuum was not accurately accounted for. The beta spectrum looks similar to what would be observed in experimental work. A significant difference that was observed is the fewer counts that would be observed at low energies in the experimental work (30 keV). This might be because of the threshold that was in place for the experimental work as opposed to simulation-based work where no thresholds are applied. The conversion electron spectra are significantly different compared to what would be observed in experimental work because of not implementing the GEB. Some features that stand out are the tail that is observed below the full energy peak. This is because of the electron interactions with the gas in the Stilbene detection cell which results in some energy loss for the electrons. This effect is more pronounced at low energies compared to high energies; this was an expected

phenomenon. If the MCNP simulations were run setting the gas density to zero, the spectra would have featured a single peak at the energy representative of the conversion electron.

4.1.1.3 Simulated Efficiencies

Having the spectra at each energy of interest helps in evaluating the detection efficiencies at each energy. For this work, the energy threshold for the electron and photon detector has been set at approximately 30 and 20 keV respectively. The MCNP output file provides a histogram of the interaction probabilities as a function of energy. From a photon perspective, the threshold should not significantly affect the detection efficiency because the energies of interest are relatively higher than the threshold. As for the conversion electrons, the 129 and 199 keV emissions are significantly above the threshold, even if the tail is included. As for the 45 keV conversion electron, there are a fraction of counts that will fall below the noise threshold. Similarly, for the 346 and 910 keV β_{max} emissions, there are a fraction of the counts which fall below the energy threshold and will not be accounted for in the energy spectra. Coincidence efficiencies are simply the product of the electron and photon detection efficiencies. Table 5 shows the electron, photon, and coincidence detection efficiencies for all the radioxenon and decay modes of interest.

Table 5. MCNP6 simulated electron and photon detection efficiencies and the Coincidence Detection Efficiency

Regions of Interest (ROI)	ε_{e^-} (Stilbene)	ε_{γ} ($SrI_2(Eu)$)	Coincidence Efficiency
^{131m}Xe (31 keV X-ray + 129 keV CE)	96.72 ± 0.01%	37.35 ± 0.14%	36.12 ± 0.13%
^{133m}Xe (31 keV X-ray + 199 keV CE)	97.20 ± 0.01%	37.35 ± 0.14%	36.30 ± 0.13%

^{133}Xe (31 keV X-ray + 0-346 keV β_{max})	65.01 ± 0.04%	37.35 ± 0.14%	24.28 ± 0.09%
^{133}Xe (81 keV gamma + 0-346 keV β_{max})	65.01 ± 0.04%	39.59 ± 0.14%	25.73 ± 0.09%
^{133}Xe (31 keV X-ray + 45 keV CE)	36.33 ± 0.07%	37.35 ± 0.14%	13.56 ± 0.05%
^{135}Xe (250 keV gamma + 0-910 keV β_{max})	87.82 ± 0.02%	23.96 ± 0.14%	21.04 ± 0.12%

4.1.2 Optical Transport Codes

This section covers the work performed in terms of the optical photon transport in the $CeBr_3$ crystal. This work was done to study the optical photon distribution on the SiPMs at the four corners of the crystal. Two codes were explored in this work: DETECT2000 and Geant4. A brief comparison was performed in terms of the results obtained using these two codes from a photon distribution standpoint.

4.1.2.1 DETECT2000

The crystal geometry measuring 44x44x22 mm and reflection properties deck was first built in DETECT2000. This toolkit enables the user to specify a single optical property for each surface, for example, detection surface, polished reflection surface, etc. In the case of the $CeBr_3$ design, one of the surfaces is required to accommodate 4 detection surfaces (SiPMs) and the remaining area is to be covered by a reflection surface. Therefore, to effectively replicate the detector design it was decided to use a total of nine cuboids and attach each adjacent surface using a connect command in DETECT2000 to build the entire crystal. The connect command is used when two

bodies are sharing a common surface. For this work, both specular and diffused reflectors were simulated to observe for differences in optical photon distribution over the surface. It is worth mentioning that since DETECT2000 is only an optical photon transport code, the effective volume of photon generation in the scintillator heavily dictates the photon distribution over the detection surface. After the geometry was defined, 10 million photons were simulated for both diffused and specular reflector surfaces. The FATES command was used to record the coordinates of each photon's termination. This data was then read by a MATLAB script and based on the termination position a heatmap was plotted. For better visual resolution, a pixel size of 0.1 mm was chosen. Fig. 51a and 51b show the results from DETECT2000 while employing paint (diffused) and metal (specular) reflective material respectively.

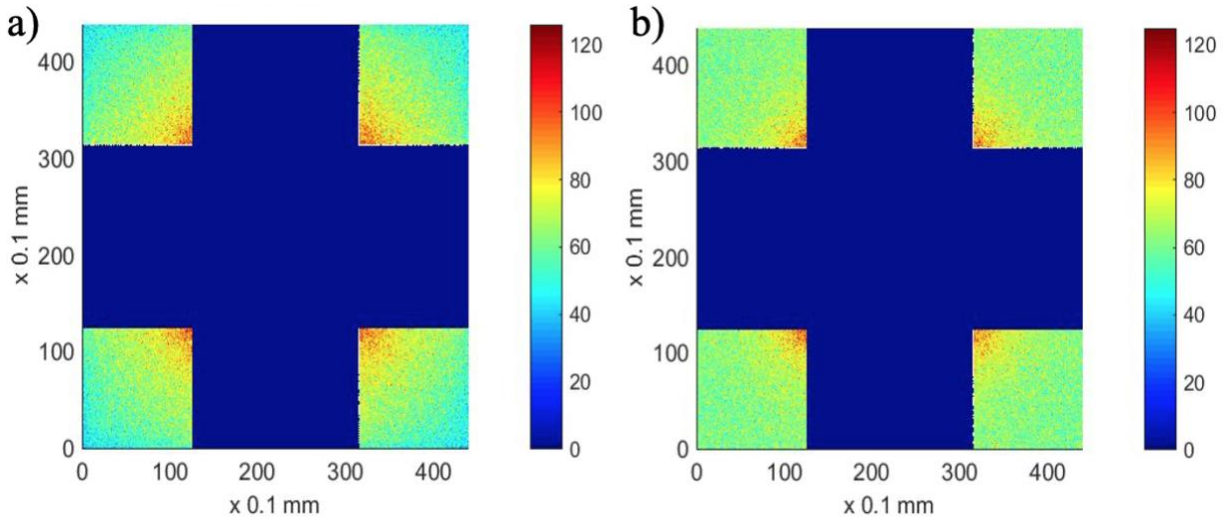

Fig. 51. DETECT2000 results using a) diffused, and b) specular reflector

As it can be observed in the heatmaps, the interior corners of the SiPMs are acting as detection hotspots in both cases. The only difference apart from that is for a polished reflector the photon distribution is rather consistent throughout the surface except for the edges. As for a diffused reflector, the photon distribution is relatively higher at the interiors of the SiPMs (near the centers) and gradually reduces as we proceed towards the outer edges of the scintillator.

It must be pointed out that a metal surface that acts as a specular reflector is not supposed to feature any photon detection hot spots. The reason for a hot spot in the polished reflector is because the source was defined between 11 and 33 mm on the x-y plane and 0 and 22 mm on the z-axis. This results in a majority of photons being generated near the interior of the SiPM detection surface leading to an observable hotspot at the corners.

One major drawback of DETECT2000 is that it is purely an optical photon simulation package, which means there is no transport of ionizing radiation that is performed in the toolkit. Once the source volume for optical photons is defined, DETECT randomly samples inside the volume, and if the location falls inside the detector volume, a photon is generated at this point and isotopically transported through the body of the scintillator. If the point sampled doesn't fall inside the pre-defined volume, the next point is sampled. This method of sampling works best if the entire detector is uniformly producing optical photons from scintillation like in the case of high energy particle detection, but in cases where relatively low energy ionizing radiation is involved, this assumption doesn't hold valid. In such cases, surfaces near the source are more probable to act as locations for initiating optical photon transport. The lack of gamma interaction and the relatively simple treatment of defining optical sources act as major barriers to the DETECT2000 toolkit. Therefore, it was decided to use Geant4 which can handle both the gamma/X-ray interactions and also the generation/ transport of optical photons.

*4.1.2.2 **Ge**ometry **an**d **T**racking 4 (Geant4)*

Geometry **an**d **t**racking (Geant4) is a Monte Carlo based simulation toolkit that has the ability to track ionizing radiation, create optical photons based on radiation interaction, and propagate optical photons in the detector volume. Geant4 offers a potential solution to one of the shortcomings of DETECT2000 where the photons were required to be created in a regular geometry.

A 44x44x22 mm^3 geometry was constructed in Geant4 with a 23.5 mm diameter hole in the center. This was followed by providing the geometry with the properties of $CeBr_3$ like the scintillation yield (68 photons per keV), refractive index (~2.0), and density (5.2 g/cc). Geant4 also provides the option of setting a yield ratio which is the relative intensity of the fast component over the total scintillation yield. This factor was set to 1 because analyzing the timing component of the pulse wasn't in the scope of this work. Assuming that the crystal is pure, the resolution scale of the scintillator was also set at 1. This factor determines the number of photons generated in each interaction. Under ideal conditions, the error in the number of photons generated is equal to the resolution scale multiplied by the square root of the scintillation yield. For the purpose of assigning optical properties to a geometry, the materials properties table in Geant4 was used.

The next step was building a reflector geometry around the surfaces of the $CeBr_3$ scintillator. Three such surfaces were required for this crystal; one around the outer surfaces of the cuboid, the second surface for the interiors of the thru-hole, and the third surface for the area which is not covered by the SiPMs. It must be noted that the thickness of the reflective material didn't seem to affect the reflectivity of the surface, this is contrary to what is observed for PTFE where the reflectivity is heavily dependent on the number of layers of the PTFE wrapping. While setting the surface properties of a reflective surface, the user is presented with three parameters: the surface type, finish, and reflection model. We shall be going over each of these parameters and the various options available.

There are two major models used for optical photon reflection: Glisur and Unified. In the Glisur model, it is assumed that a surface is made up of multiple microfacets. Each time a photon interacts with a surface a microfacet is selected from a distribution and based on the microfacet selected the photon is reflected. The second type of reflection is based on the unified model. In the unified model of reflection, when a photon interacts with a surface, four types of interactions are possible: specular spike, specular lobe, backscatter, and diffused reflection.

It is worth mentioning that the probabilities of the four types of reflections must add to unity and in the Geant4 framework, these factors are independent of the angle of incidence of the photon. However, in reality, it has been observed that these probabilities change with the angle of the incidence photon. The unified model of reflection is the same algorithm that is used in the DETECT2000 toolkit. It must also be pointed out that the default reflection model in Geant4 is the Glisur model of reflection.

The second parameter of importance is the type of reflector. Dielectric-dielectric and dielectric-metal are the two options available to users. In the case of a dielectric-metal surface, the photons are reflected based on the reflectivity set by the user. The photons that are not reflected are absorbed by the surface. Therefore, in its basic usage, this interface is best suited for a perfect photon absorber or reflector. The next type of reflector is a dielectric-dielectric surface. The photons can undergo total internal reflection, refraction/reflection based on the angle of incidence, refractive index, and the wavelength of the photon. The major governing factor in this type of surface is the refractive index of the medium the photon is exiting and the refractive index of the medium the photon is entering. In this work, the SiPMs which act as optical photon black-holes use a dielectric-dielectric surface type with a minimal absorption length for the photons in the SiPMs; this essentially terminates the photons as soon as they enter the SiPMs. In the stepping action section of the code, if it is observed that the photon has entered the SiPMs and it has been absorbed (terminated), the x, y, and z-axis positions of this terminated photon are recorded. Geant4 outputs this coordinate data as a text file which is then read by a MATLAB file to extract the positions along the SiPM plane and plot the data in a heatmap.

The third parameter is the surface finish of the reflector. Broadly speaking there are two types of surface finishes: polished and ground. A polished surface between two bodies leads to perfect specular reflection. In such cases, the angle of incidence and angle of reflection is almost the same. It has been observed that when such surfaces are employed in the capacity of a reflector, there is a uniform distribution of optical photons

on the detection surface. The second type of surface finish is ground, this is the case when diffused reflection dominates.

The literature review has revealed that the reflection models incorporated in Geant4 are not always accurate and evidence has been provided by various groups where experimental vs simulation data has yielded different results. Therefore, the new releases of Geant4 have provided the users with an option of using reflection coefficients based on experimental data. For this work, it was decided to use data from the DAVIS Look-Up Table (DAVIS LUT). These experiments were carried out using LYSO crystal with various surface finishes and reflector combinations. Although these results are not based on the crystal used in this work, it was decided to use the DAVIS model since it's based on experimental results. Fig. 52a shows the optical photon distribution using a polished PTFE reflection while the photon distribution from a rough PTFE is shown in Fig. 52b.

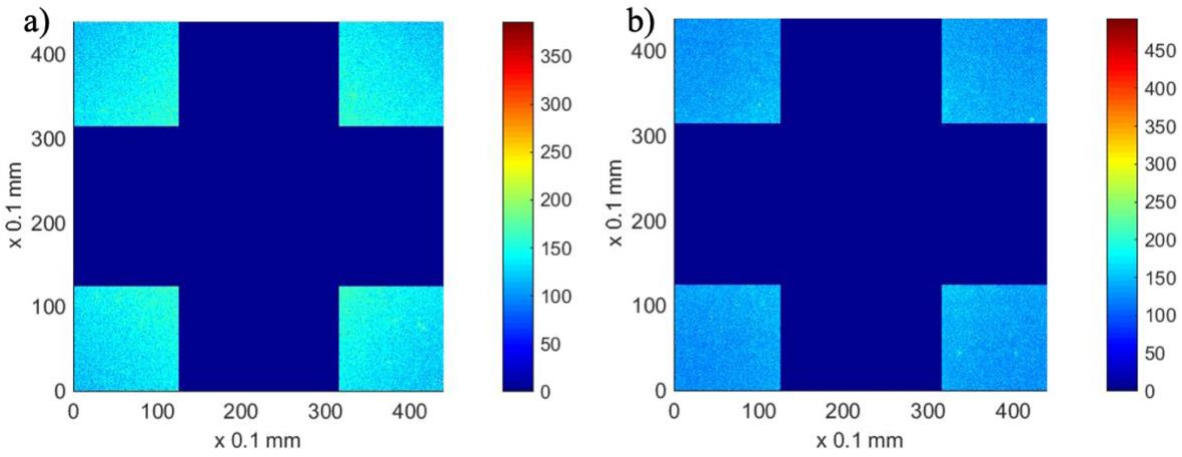

Fig. 52. The DAVIS model results using a) polished, and b) rough PTFE

It can be observed from Fig.52 that both polished and rough PTFE exhibit the same behavior where optical photon hot spots are found at the interiors of the SiPM. Although visually there appears to be a difference between the two reflectors, upon further analysis and matching the heat map indexes, it was found that there are no notable differences between the polished and rough PTFE except for the fact that a polished finish is more efficient in reflecting optical photons. Comparing the results

from DETECT2000 it is noted that there are some similarities like optical hotspots near the interior surface of the SiPMs and a gradual decrease of intensity as we approach the exteriors of the SiPMs. Although in this study there was no significant difference observed in terms of optical photon distribution, Geant4 is expected to provide a more realistic representation of the location where photons are created taking into account that the photon transport code used in DETECT2000 and Geant4 is the same.

4.2 Cerium Bromide ($CeBr_3$) Characterization

In this section, we shall be covering the work that was done using the $CeBr_3$ detector. Initially, it was decided to use the digital integration method after which the choice was made to switch to analog integration using a charge-sensitive preamplifier. The methods used, results obtained, and the challenges are detailed in this section.

4.2.1 Crystal Assembly and Retrofitting

The crystal was grown and assembled by Hilger Crystals Ltd based out of the United Kingdom. Hilger was also responsible for mounting the SiPM arrays according to our design and including encapsulation for preventing any moisture uptake by the crystal. The crystal initially arrived at OSU with some of the SiPM pins severely bent and misaligned. Fig. 53a and Fig. 53b show the alignment of the pins with respect to other SiPM arrays and the extent of the pin bend respectively.

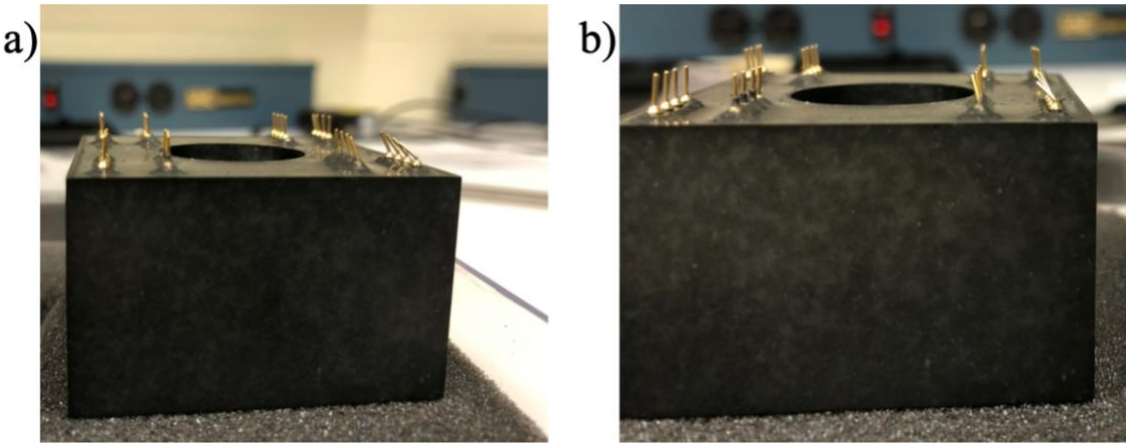

Fig. 53. The $CeBr_3$ crystal illustrating a) the misalignment of the pins, and b) the bent SiPM array pins

Taking into account the extent of the bent pins it was not feasible to place the crystal successfully on the board. Two primary actions were required to connect the board and the crystal: straightening the bent pins and finding an alternative to seat the misaligned pins on the board. Attempts to straighten the bent pins, unfortunately, resulted in 4 of the 8 pins being snapped on one of the SiPM arrays. Two of those snapped pins were anodes and the other two pins were cathodes. SensL SiPMs are designed to operate on a common cathode, which means, having a single cathode connected to the biasing voltage is sufficient to power the entire SiPM array. The anodes however don't share the same feature; therefore, wires were used to physically solder the two anodes on one side to the adjacent anode which still has a physical pin. To address the problem of misaligned pins, it was decided to use four 2x4 dual inline (DIL) 0.3" row spacing sockets on top of the SensL J-series 2x2 SiPM arrays. The depth of these DIL sockets allowed us to push the SiPM pins gently into the sockets. It must however be pointed out that, despite these best efforts, there was some amount of friction that was encountered while assembling the detector on the board. Fig. 54a and Fig. 54b show the soldered pins to enable anode readout and the DIL sockets that were connected to the SiPMs to enable successful mounting of the crystal on the readout board respectively.

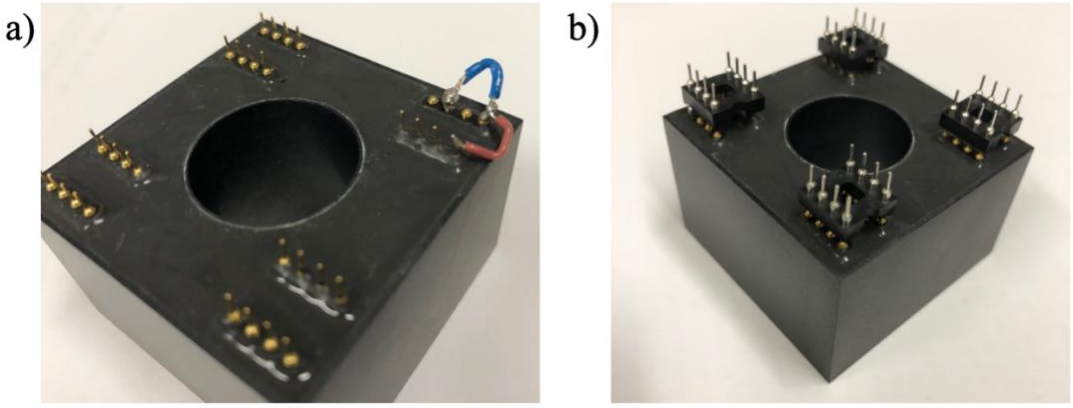

Fig. 54. a) the solder connections made to enable anode signal readout from one of the SiPM arrays; b) the DIL sockets attached to the SiPMs to mount on the PCB for readout

4.2.2 Board Design

There are two methods to detect the energy deposition in a scintillator, in the first method, the current pulse can be integrated over a set duration of time (generally about 5 times the decay time) to obtain the total charge deposition in a pulse. In the second method, the charge is integrated over a capacitor and discharged over a resistor (charge sensitive preamplifier) and the peak of the voltage signal can be sampled, this peak is representative of the total charge deposited in a pulse. The charge produced (current signal) by the SiPMs is initially converted to a voltage signal, this signal is then read by the Analog to Digital Converter (ADC) which digitizes the signal enabling it to be read by an FPGA.

A 4-layer custom board measuring 47 mm x 75 mm was designed for the Stilbene-$CeBr_3$ detection system. It is intended for the detector to be directly mounted in the female sockets of the board. These female sockets provide both the power supply for the cathodes as well as read the signals from the anodes of the SiPMs. A 3.3 V Low Dropout (LDO) regulator was included to power the preamplifiers as well as two separate 3.3V internal layers for power supply and ground. Two switching regulators (LT8410) were used to power the Stilbene and $CeBr_3$ SiPMs. It was decided to use two rather than a single regulator to minimize any crosstalk between the detectors. Four non-inverting amplifiers were used for the $CeBr_3$ SiPM arrays (one amplifier for each array). The signal from the Stilbene SiPM array was routed through a separate non-inverting amplifier. The gain of all the amplifiers was maintained at 11. Each J-series SiPM in the 2x2 SiPM array (MICROFJ-60035-TSV-TR1) has a capacitance of 4,140 pF. Therefore, the total capacitance of the array adds up to 16,564 pF. If all the four 2x2 arrays were connected in parallel, the total capacitance would add to 66,256 pF. In an effort to reduce the total capacitance, it was decided to use individual amplifiers for each of the 2x2 arrays and sum all the outputs at the end. In this way, the total capacitance can be maintained at about 16,560 pF. The reader is reminded that capacitance adds linearly in a parallel connection and an increase in capacitance leads to a decrease in the voltage signal when the charge produced is a constant. It is worth mentioning that the Stilbene-SrI_2(Eu) design used the same board to power the Stilbene

SiPMs. The signal readout for the electron detector was also achieved using the SMA connector jack identified in the board layout.

4.2.3 Digital Integration

The next step in the process was to use lab check sources to obtain a spectrum followed by characterization and calibration. For this purpose, ^{137}Cs was initially used followed by ^{133}Ba. The former was used to determine the energy resolution of the detector and the latter was used to study the performance of the detector at a wide range of energies. The pulse shape from a ^{137}Cs source is shown in Fig. 55.

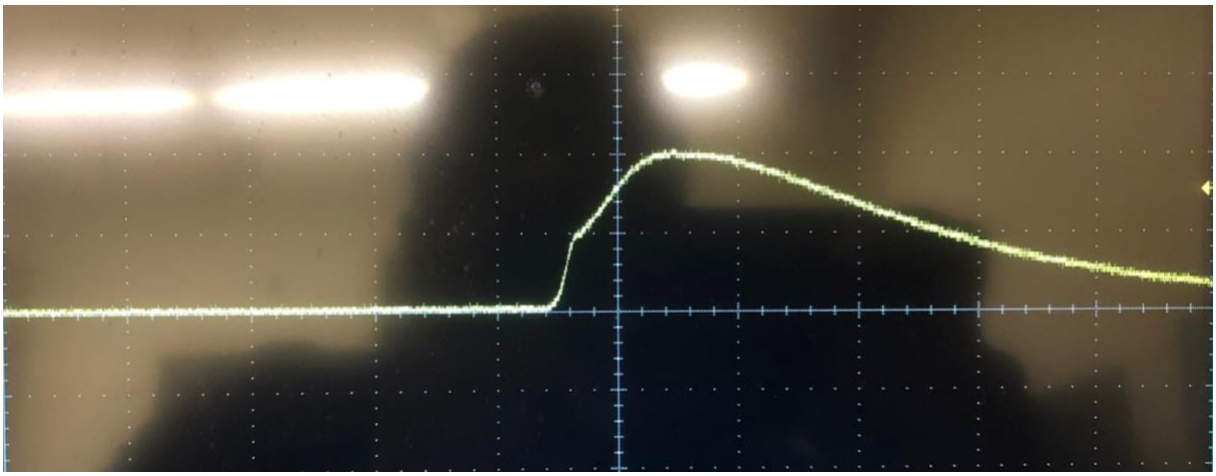

Fig. 55. Pulse from the $CeBr_3$ detector illustrating the two-component rising edge using a ^{137}Cs disk source

The rise time of the pulse was determined to be about 400 ns. The peak amplitude of the pulse was found to be about 200 mV using a ^{137}Cs source. The decay time (τ) observed from the $CeBr_3$ + SiPMs was found to be about 1200 ns. This is significantly longer than the decay time of the $CeBr_3$ scintillator, therefore, it can be inferred that this long decay time is mostly because of the inherent capacitance of the SiPMs used for photon detection. The next step was to collect the spectra using multiple sources. Two digital integration methods were implemented in this study, the first method involved using an accumulator to individually add a set number of data points on a pulse. The second method involved using a filter and a convolution operation to sum

the data points on a pulse. This summed total is appropriately scaled to increment a particular channel on a spectrum. For both these methods, the baseline is initially calculated by estimating the mean of a set number of samples before the pulse rises. This baseline is subsequently subtracted from all the pulse samples. This operation essentially brings the baseline down to zero.

On the pulse processing front, the pulse data from $CeBr_3$ was being read by the 2-channel digital pulse processor. This processor was initially set up to digitize pulses at 200 MHz giving us a sampling period of 5 ns. The challenge in this setup was that the entire pulse was unable to be captured because only 1024 samples (5.12 μs) worth of data was being read by the DPP2. This included 400 samples (2 μs) delay to estimate the baseline. Therefore, to remedy this it was decided to reduce the sampling frequency from 200 MHz to 100 MHz, this increases the sampling period to 10.24 μs which is long enough to account for a good chunk of the pulse before it returns to baseline.

After it was ensured that the entire pulse was being captured, 1 million individual pulses were collected using ^{137}Cs. It was decided to use a rod source at the center of the detector to mimic the radioxenon gas source. The other reason for using a rod source was to ensure that all the SiPM arrays have an equal chance of detecting optical photons from the scintillator. The ^{137}Cs rod source was placed at the center of the $CeBr_3$ crystal to ensure maximum solid angle and improved efficiency. Fig. 56 shows the spectra obtained using digital integration at 100 MHz using a ^{137}Cs source. It is worth mentioning that both the digital integration methods (filter and accumulation) based methods yielded similar spectra.

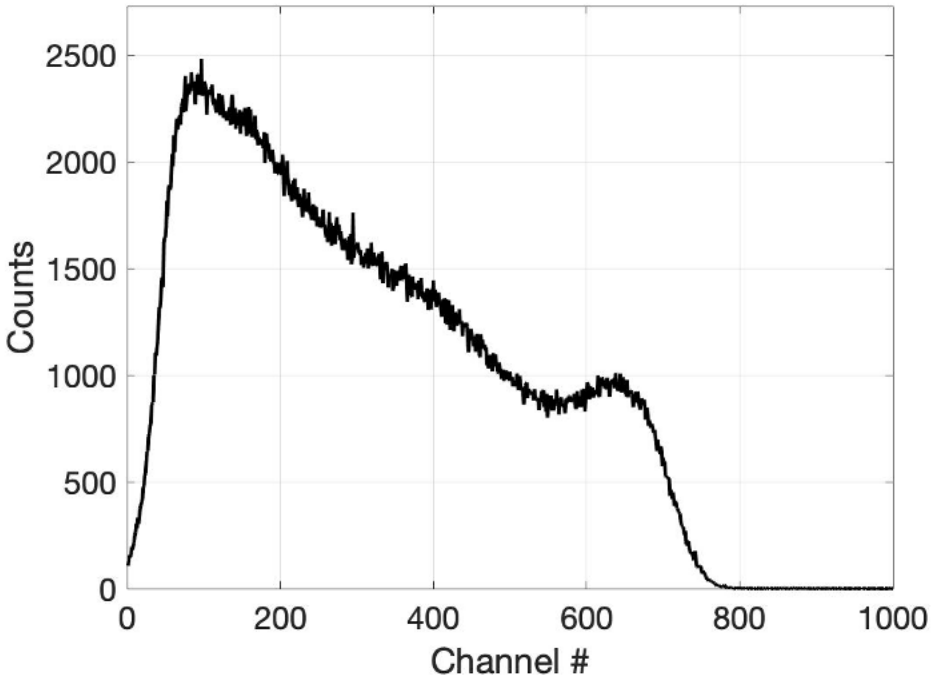

Fig. 56. $CeBr_3$ detector response from a ^{137}Cs rod source using Digital Integration at 100 MHz

4.2.4 Analog Integration

After it was observed that the digital integration method wasn't yielding successful results, it was decided to use the analog integration technique to process the signals from the SiPM. Since it wasn't feasible to redesign a new board for the analog integration method, it was decided to use the Cremat preamplifier board that was designed for the SrI_2(Eu) detection system.

As it was previously mentioned, all the cathodes on the SiPMs are common cathodes, which means providing biasing voltage to one of the pins is sufficient to power all the arrays. On the anode end, it was required to connect all the anode pins across all the arrays together. This was accomplished by soldering the wires between all the arrays. Another important aspect here was decoupling the analog electronics for each array, this was done to prevent any current from reaching the components on the $CeBr_3$ board. To accomplish this, it was required to individually remove the resistor and capacitor from the PCB which were in direct contact with the anode pins on the SiPMs. Once

this was done, the $CeBr_3$ SiPMs were being powered on using the $SrI_2(Eu)$ preamplifier board and the anode pulse processing was being carried out using the Cremat preamplifier.

Individual pulses were then routed through an oscilloscope to observe the shapes of the pulses. This indicated that the rise time of the pulse was about 8 μs, similar to the rise time observed for the $SrI_2(Eu)$ detector. The challenge in the signals being obtained from the preamplifier is the poor signal-to-noise ratio (SNR). The pulse amplitudes for the 662 keV peak were between 25 and 30 mV which is at least an order of magnitude less compared to the $SrI_2(Eu)$ detector. Therefore, it was decided to increase the value of the resistor right before the current signal from the SiPMs reach the Cremat preamplifier. This not only provided an increase in the pulse amplitude but also increased the noise that was observed in the pulse. In other words, the SNR remained almost the same. As a comparison, Fig. 57a and Fig.57b shows an oscilloscope screenshot of the pulses obtained from the $CeBr_3$ and $SrI_2(Eu)$ detectors in response to the 662 keV photon from ^{137}Cs.

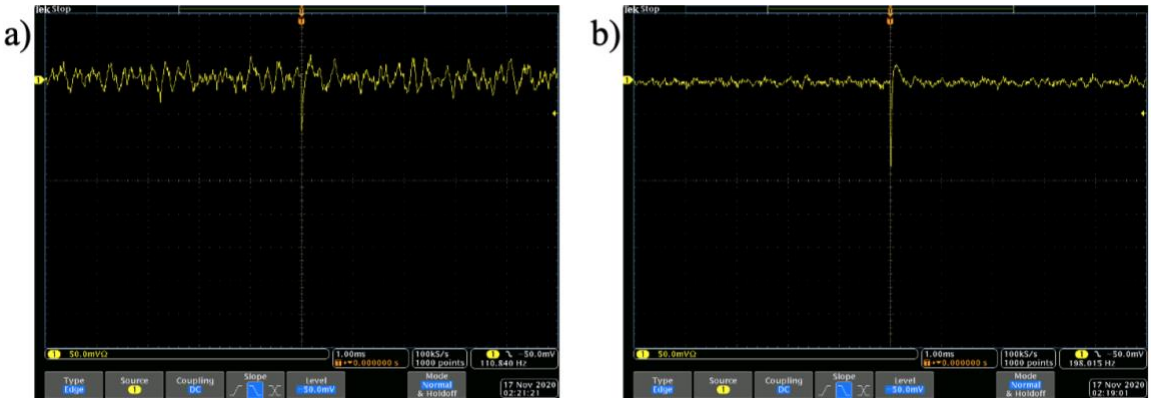

Fig. 57. Oscilloscope screen shots in response to the 662 keV photon from ^{137}Cs using a) the $CeBr_3$, and b) $SrI_2(Eu)$ detector

As it can be observed, the SNR from the $CeBr_3$ detector is significantly poor compared to the $SrI_2(Eu)$ detector. Nevertheless, it was decided to process the pulses using the DPP2 to obtain a spectrum. The flat-top time was chosen to match the rise time of the pulse and multiple peaking times were experimented with. The spectrum from one of the settings is shown in Fig. 58.

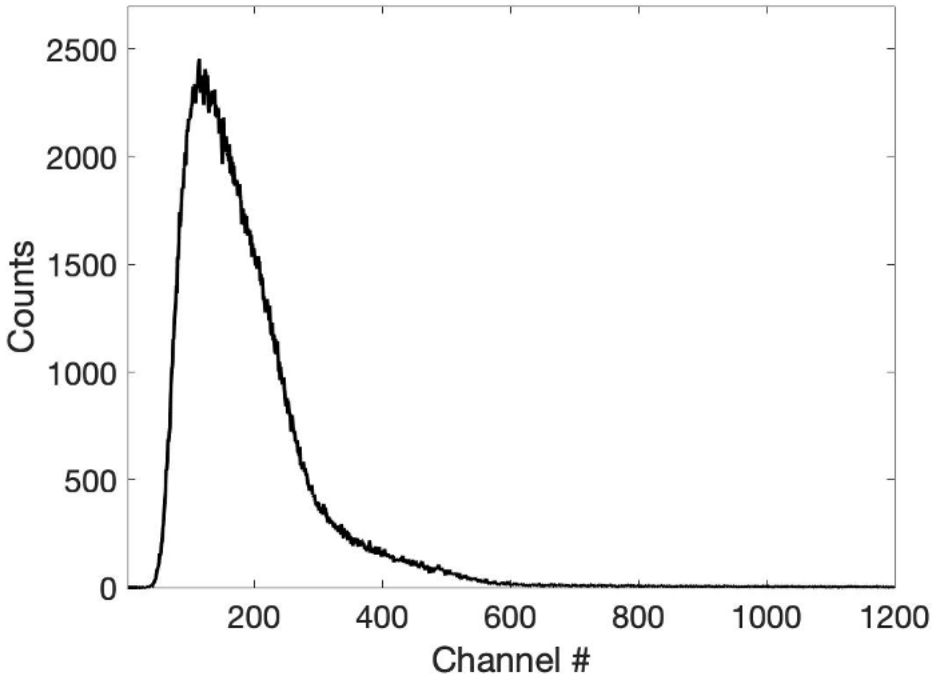

Fig. 58. $CeBr_3$ spectrum using ^{137}Cs employing the analog integration technique (Cremat Preamplifier)

It can be observed that using both the techniques (analog and digital), obtaining an appreciable spectrum using $CeBr_3$ proved to be a challenge. At this point, the manufacturer of the crystal was consulted (Hilger Crystals Ltd.), upon observing the detector response and the techniques that were explored, a few reasons for poor detector performance were hypothesized. Among these reasons were, issues related to SiPM integrity, optical interface complications between both the SiPM/ crystal and the reflector/ crystal, hermetic seal breakdown, and crystal cleavage.

Based on the aforementioned reasons, it was later decided to explore the option of replacing the $CeBr_3$ detector with the two $SrI_2(Eu)$ detectors that were previously used in conjunction with the PIPSBox. This study also provides us an opportunity to experimentally demonstrate that the efficiency of the detection system plays a more important role in the reduction of the MDC compared to the energy resolution. It has been observed that the solid angle for photon detection using both the PIPSBox and the Stilbene gas cell are similar. Therefore, this is an excellent chance to compare the effects on the MDC using the Stilbene- $SrI_2(Eu)$ design. The remainder of the results

section shall focus on the coincidence identification module, detector calibration and response to lab check sources as well as TRIGA reactor irradiated xenon samples of interest.

4.3 Pulse Processing and Coincidence Identification

This section covers the experiments that were done with the DPP2 and DPP8 to identify the extent of spectral broadening that is caused because of the processing electronics and the efficacy of the coincidence identification module used in the DPP8. For both these tasks, the dual-channel pulse generator from Agilent Trueform 33500B was used to create synthetic pulses that resemble the pulses generated from the radiation detection system.

4.3.1 Pulse Processor Spectral Broadening

The pulse processor was used to collect 100 thousand pulses at a set amplitude using both the DPP2 and the DPP8. The point of the exercise was to estimate the amount of spectral broadening that was responsible because of the electronics. Under ideal circumstances, the detector response is supposed to be a delta function for any given photon impinging on the detector. In real life, there are several factors that prevent such a behavior ranging from, electronic noise, digitization errors, fluctuation in the number of photons generated at a given energy, non-uniform photon reflection, electromagnetic pickup among others. Therefore, it was decided to perform a short exercise to estimate the energy resolution of the peaks obtained from the signal generator using the DPP2 and the DPP8. Pulse data was collected in MATLAB and processed using trapezoidal filters, the amplitudes of pulses were adjusted in MATLAB to represent a peak at 662 keV. The spectra for data collected using the processors are provided in Fig. 59.

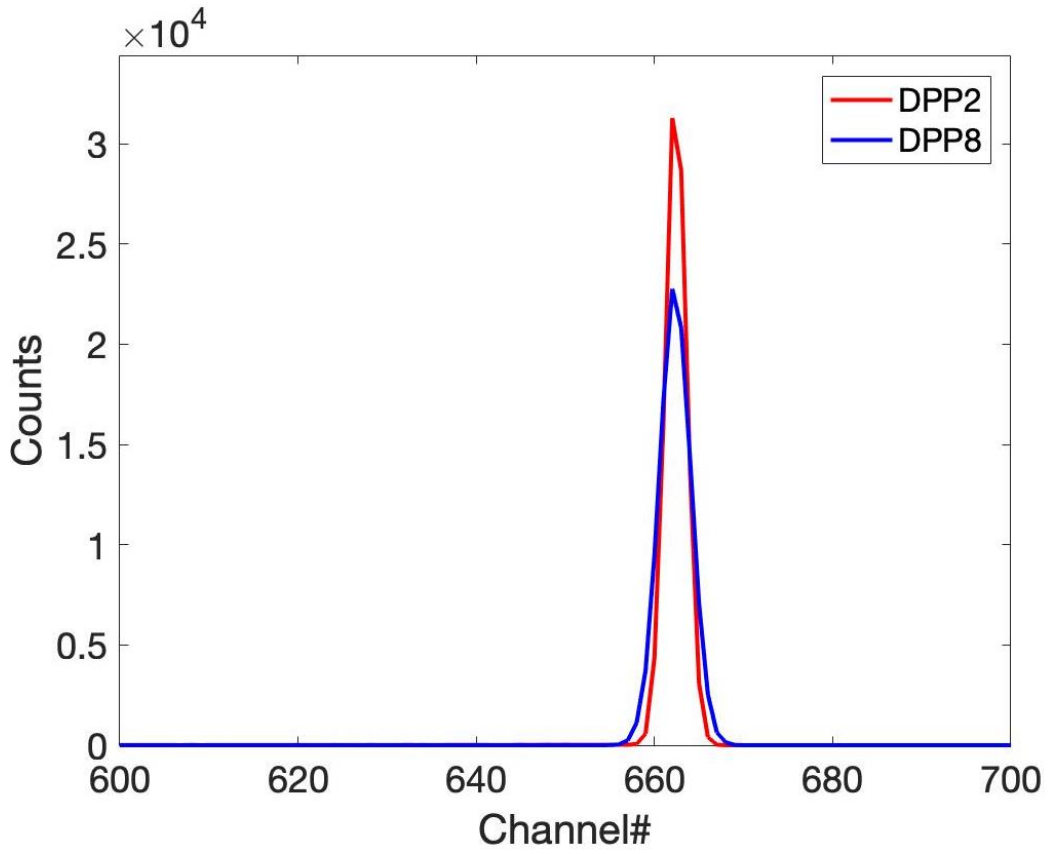

Fig. 59. Comparison between the performance of the DPP2 and the DPP8

This data were routed through a gaussian energy resolution script which determined the energy resolution of the DPP2 and DPP8 to be 0.4212 and 0.6182% at channel number 662 respectively. Therefore, from a theoretical standpoint, it can be argued that the DPP2 performs better compared to the DPP8 in terms of electronic noise. Aspects like the ability to identify coincidence events between 8 channels in real-time, and other advantages like on-the-fly trigger filter, pre-trigger sample adjustments must also be weighed in while deciding to choose a processor. Since this work requires at least 3 channels, it was decided to use the DPP8.

4.3.2 Coincidence Module Testing

Coincidence identification module is one of the most important steps in this research work. Since all the events we are interested in recording are coincidences between an

electron and a photon, the functioning of the coincidence identification module is of utmost importance.

Therefore, for this work, both channels of the pulse generator were used to test the coincidence identification module. There was a 5 μs delay introduced between the two channels (Fig. 60). The ADC on the DPP8 which is clocking at 125 MHz requires us to maintain a coincidence time window of about 625 clock cycles (5 μs). This is calculated by dividing the delay by the clock period of the digitizer. Coincidence count rates were recorded from 615 to 630 clock cycles which translates to 4.92 to 5.04 μs in the time domain. Fig. 61 shows the coincidence count rate as a function of the coincidence time window. It is brought to the reader's attention that, although at 625 samples the maximum count rate was estimated to be achieved, data was collected for an additional 40 ns to ensure that no stray events were being recorded. A flat line after 625 samples represents that all the events recorded were indeed coincidence events. Additional procedures like polarity switch and single-channel test were also conducted to study the coincidence module performance. As expected, the module stopped counting when one of the channels was switched off or when the polarity of either pulse was inverted. All these steps show the robustness of the coincidence identification module implemented in real-time on an FPGA.

Fig. 60. Signal from the two channels that was fed to the DPP8 for coincidence testing

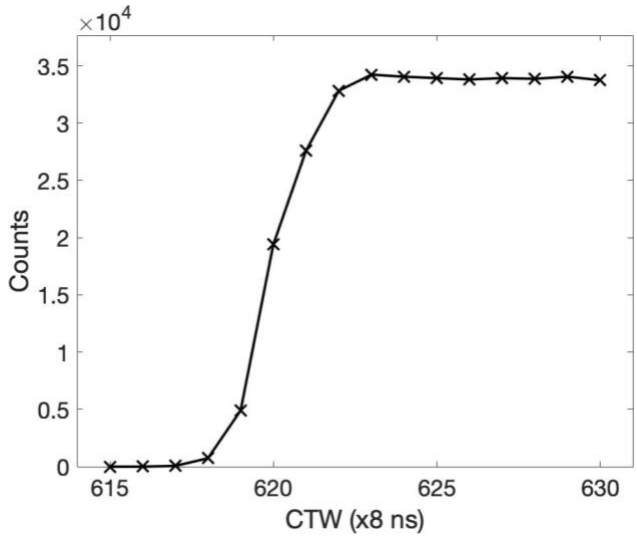

Fig. 61. The number of coincident counts as a function of CTW for a delay of 5 µs (625 samples) using two channels of the DPP8

Fig. 62 shows the block diagram of the coincidence identification for the Stilbene-$SrI_2(Eu)$ detection system and some user-defined variables in the MATLAB interface. Ch-1 and Ch-3 represent the $SrI_2(Eu)$ detectors while Stilbene is represented by Ch-2.

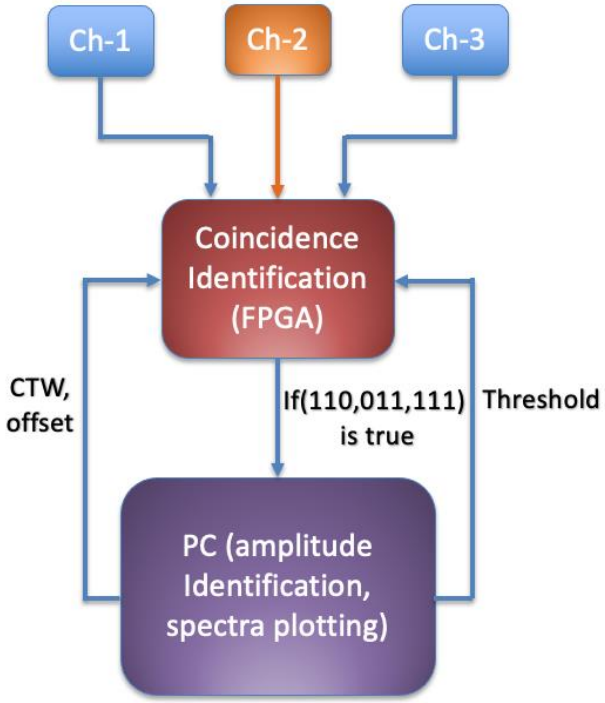

Fig. 62. Coincidence identification for the Stilbene-$SrI_2(Eu)$ design along with the user defined on the fly variables

4.4 Strontium Iodide (SrI_2(Eu)) Characterization

In this section, we shall be going over the preliminary characterization experiments that were carried out using the SrI_2(Eu) detectors. These tests include checking the performance at low energies using the variable energy X-ray source and results from conventional lab check sources. Apart from this, additional tests have also been performed for checking the coincidence backscatter plot and the coincidence timing between the two-photon detectors.

4.4.1 Evaluation Using Lab Check Sources

In this section, we shall be going over the detector response of the scintillator using conventional lab check sources like ^{133}Ba and ^{137}Cs. ^{133}Ba was chosen because of its multiple peaks, especially at low energies (~30 and 80 keV). This is additionally even more important because it allows us to study the performance of the detector at these two energies which are representative of the X-ray and gamma photons released by ^{131m}Xe, $^{133/133m}$Xe. A peaking time of 4.8 μs and a flat-top time of 9.6μs was chosen to account for the entire rising edge and match with the oscillations produced by the switching regulator. The ^{137}Cs spectrum is also important because it allows for the determination of the energy resolution at 662 keV and additionally also emits the 30 keV X-ray which is instrumental in threshold determination. Fig. 63a and Fig. 63b shows the energy spectrum obtained from ^{133}Ba and ^{137}Cs. It is worth pointing out that the energy threshold for SrI_2(Eu) was about 20 keV.

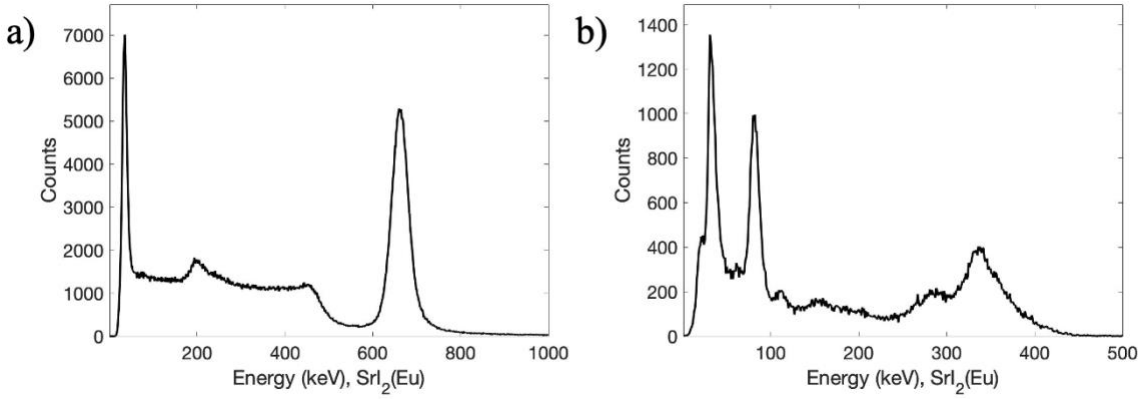

Fig. 63. Energy spectrum from a) Cs-137, and b) Ba-133

As it can be observed in the spectra above, all the features from both the radionuclides are clearly observed. For ^{133}Ba, the 30 keV and 80 keV peaks are prominent, also the peaks at higher energies are observed. Below the 30 keV peak, some amount of background/ noise counts seems to interfere with the symmetry of the 30 keV peak. This problem has since been fixed by marginally increasing the threshold in the ^{137}Cs spectrum. It is brought to the reader's attention that, under some circumstances where the count rate/ activity of the source is very high, having a relatively lower energy threshold is not going to significantly hamper the features of the spectrum. The 662 keV peak resolution was determined to be about 6.5% and the X-ray peak energy resolution was found to be about 28% FWHM. The full energy peak (662 keV) resolution determined using the RX1200 digital pulse processor in previous studies was found to be about 5%. It is also brought to the reader's attention that one of the photon detectors is significantly brighter compared to the other detector (almost 1.8 times). This difference was initially observed while working with the PIPS-SrI2(Eu) detector, but during that work, the difference in brightness was found to be about 1.4 times. This difference in scintillator brightness seems to have increased over a span of 18 months, this might play a role in the reduction of the energy resolution.

4.4.2 Variable Energy X-ray Source

This exercise aims to evaluate the threshold of the photon detector and to observe if the detector is successful in identifying peaks below 30 keV. For this purpose, a variable energy X-ray source was used. This source houses a ^{241}Am source which emits high-energy alpha radiation along with a gamma photon at about 59 keV. These alpha radiations interact with a rotating rack of 6 metal targets which enables the generation of the X-rays at variable energies. The six metal targets, along with the emitted X-ray energy and photon yield are shown in Table 6. It is worth mentioning that, out of these targets, spectra were successfully collected for Mo, Ag, and Ba. Upon experimenting it was observed that Cu and Rb X-rays were below the energy threshold of the scintillator. As for Tb, although the X-rays were significantly above the threshold, the resolution of the SrI_2(Eu) was not high enough to successfully separate the X-ray peak from Tb and the low energy gamma (~59 keV) from ^{241}Am. Fig. 64a, Fig. 64b, and Fig.

64c show the spectra obtained when Mo, Ag, and Ba metal targets were exposed to the alpha radiation source from ^{241}Am respectively.

Table 6. The energies and photon yield of the variable energy X-ray source for the six targets

Target	Energy (keV) Kα	Energy (keV) Kβ	Photon Yield (#/sec/Sr)
Cu	8.04	8.91	2,500
Rb	13.37	14.97	8,800
Mo	17.44	19.63	24,000
Ag	22.10	24.99	38,000
Ba	32.06	36.55	46,000
Tb	44.23	50.65	76,000

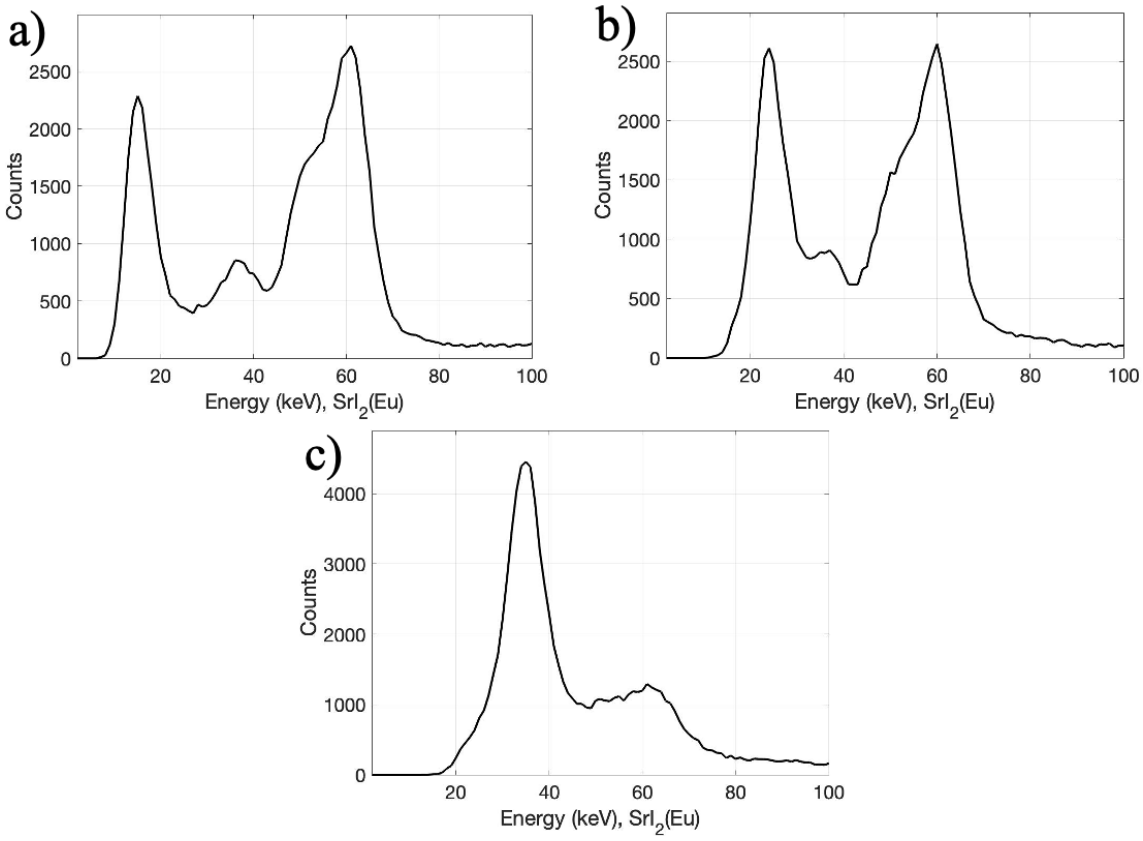

Fig. 64. The photon spectra from the variable energy X-ray source using a) Mo; b) Ag, and c) Ba metal targets

In all the aforementioned spectra, it is interesting to note the symmetry of the peaks at low energy. Also, of interest is the no/ minimal noise that was observed in the case of X-rays emitted by Mo. This shows that the photon detection system is stable even at low energies and can successfully differentiate noise from low energy photons.

4.4.3 Coincidence Time Window Selection

The next step is to determine the coincidence time window for the detection system. Ideally, this is determined after the electron detector is also completely calibrated. In our case, the stilbene detector response is not routed through a charge-sensitive preamplifier, therefore, the direct signal from the SiPMs is read and the digital integration methods are applied for signal processing. This process makes the signal from the stilbene significantly fast compared to the photon detector.

Therefore, the limiting factor in determining the CTW is the slow response of the SrI_2(Eu) detectors. This prompted a study to determine the change in the coincidence counts as a function of CTW. In this experiment, the CTW was varied between 10 and 1000 samples, which in the time domain represents a range between 80 and 8000 ns. It is expected that the coincidence counts would initially rise sharply as the CTW is increased after which the rise in counts will be more or less flat. At each CTW, ten thousand coincidence counts were collected. These experiments were repeated twice for each CTW to ensure that the count rate is not significantly different. An arithmetic mean was then computed for each CTW based on this data.

Fig. 65 shows a plot of the coincidence count rate as a function of CTW. As expected, the count rate increases initially after which the rate of change in counts decreases. It is estimated that the initial steep increase in counts is because of actual coincidence events (until about 500 samples) after which the increase in counts is mostly because of two independent events or background interactions triggering the system. Therefore, based on this study and taking inputs from the PIPS-SrI_2(Eu) research, it was decided to set the CTW at 550 samples (4.4 μs). Observing the coincidence counts as a function of CTW, it can be pointed out that at about 300 samples, a small dip in the counts is

observed. This initially prompted setting the CTW at 300 samples. This however presented a problem of trigger walking at low energies which resulted in switching the CTW back to 550 samples. This phenomenon is discussed in detail in the $^{133m/133}$Xe results.

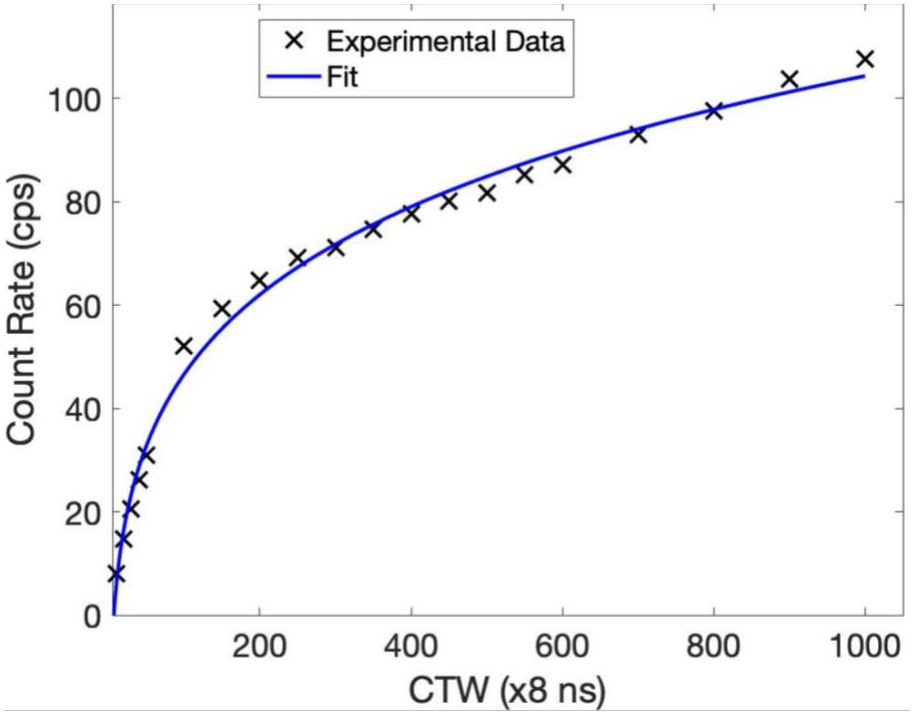

Fig. 65. The coincidence counts as a function of the coincidence time window for the two SrI_2(Eu) detectors. NOTE: At about 300 samples, a small dip in the coincidence counts is observed

4.4.4 Backscatter Coincidence Between SrI_2(Eu) Using ^{137}Cs

After determining the CTW for this project, the backscatter coincidence data were collected between the two SrI_2(Eu) photon detectors. This is an important step in experimentally demonstrating a functional coincidence identification module. For this experiment, a modified version of the detector holder was designed. This holder had all the design features from a photon detector standpoint, the only exclusion was the optical isolation ring for the Stilbene SiPM array. This was done to successfully accommodate the ^{137}Cs disk lab check source. This source was placed approximately between the two-photon detectors (Fig. 66).

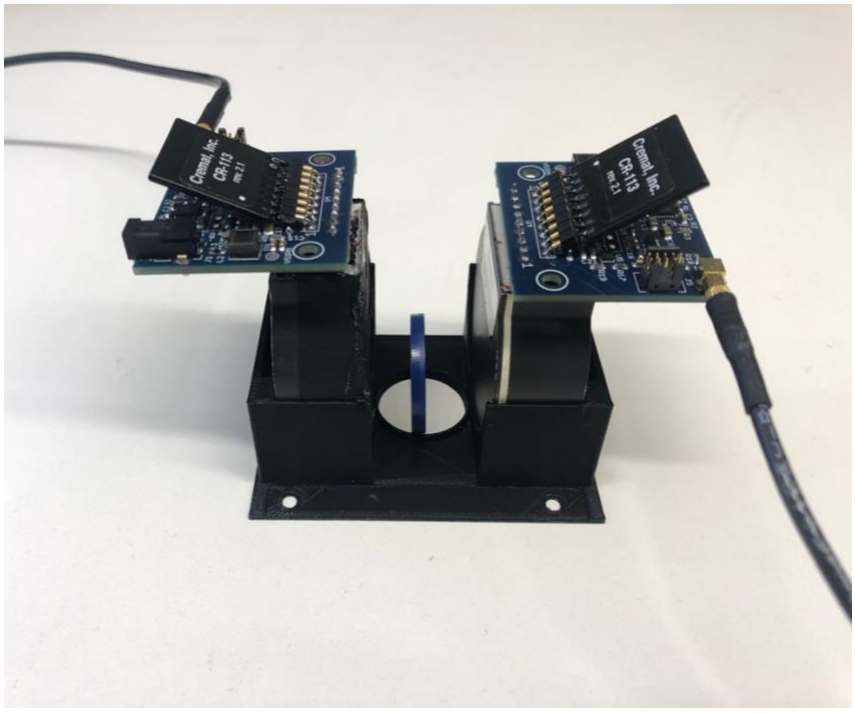

Fig. 66. The experimental setup for the backscatter coincidence measurement using ^{137}Cs. The two SrI_2(Eu) detectors are shown along with the ^{137}Cs disk source in the center

Fig. 67a and Fig. 67b shows the 1-D spectrum for the backscatter coincidence experiment performed using ^{137}Cs for SrI_2(Eu)-1 and SrI_2(Eu)-2 respectively. Under ideal situations, two peaks should be observed in each spectrum at ~185 and 477 keV respectively. Both these peaks are visible in the spectra for SrI_2(Eu)-1 and SrI_2(Eu)-2. Also observed in these spectra are the 662 and 30 keV peaks. This indicates that some of these recorded events are coincidences between the Compton, backscatter photon and the X-ray, gamma photon. It is worth mentioning that reducing the coincidence window in an effort to observe only the 477 and 185 keV photon might prove to be successful. Considering the fact that the source is not highly radioactive (~1μCi), the chances of observing a coincidence between a backscattered photon and a 30/ 662 keV photon drastically reduces. It is worth mentioning that the CTW used for this experiment was 550 samples (4.4 μs). The 2-D coincidence spectrum is shown in Fig. 68.

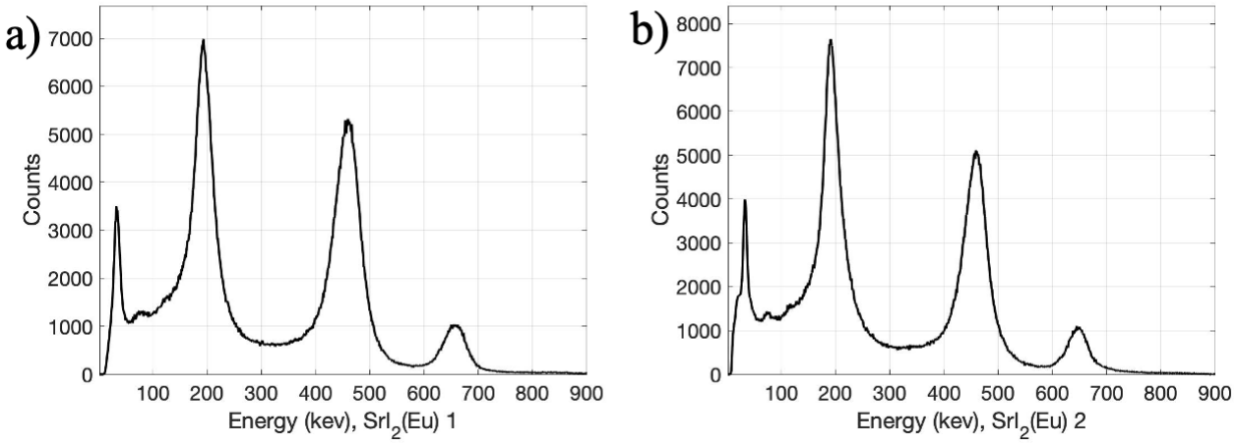

Fig. 67. The 1-D spectrum between a) SrI_2(Eu)-1, and b) SrI_2(Eu)-2 showing the various peaks observed in the coincidence back scatter experiment

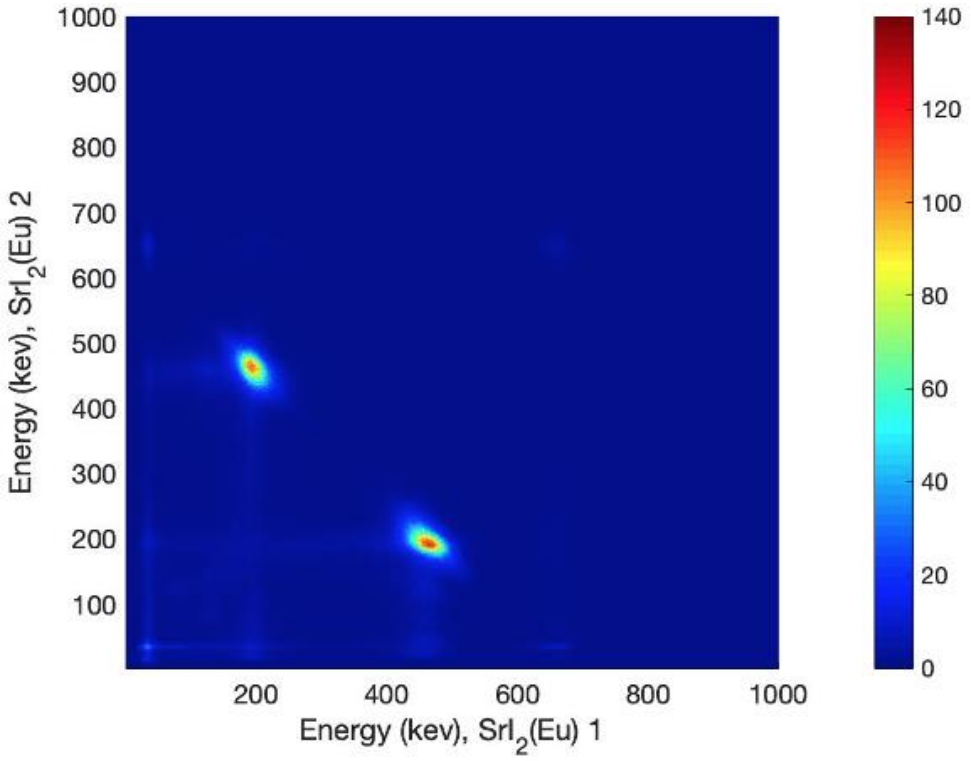

Fig. 68. The 2-D spectrum showing the backscatter coincidence plot between the two SrI_2(Eu) photon detectors using a ^{137}Cs source

The 2-D coincidence spectrum clearly identifies two hot spots at ~185 and 477 keV respectively for both the scintillators. Extrapolating a straight line through both these

points shows that the x and y-axis intercept to be about 662 keV. This experiment demonstrates that the coincidence identification module is working as expected.

4.5 Stilbene Gas Cell Characterization

In this section, we will be looking at the steps and procedures that were performed to characterize the stilbene gas cell and the optical isolation ring to ensure that no exterior optical photons interact with the Stilbene SiPM. For characterizing the stilbene gas cell, a ^{137}Cs disk check source was used, the Compton edge of the spectrum was initially used to calibrate the detector. During measurements using ^{131m}Xe, fine calibration was again performed because a monoenergetic peak offers the best opportunity to accurately calibrate the detector.

4.5.1 Optical Isolation Ring

The optical isolation ring plays an elemental role in keeping external photons from interacting with the Stilbene SiPM array. For this work, once the Stilbene gas cell is sitting on top of the SiPM array surrounded by the optical isolation ring, additional black electrical tape was needed to cover any open areas through which optical photons might interact. Data was collected under four different scenarios: no ring with no masking tape, no ring with masking tape, ring without masking tape, and ring with masking tape. For successfully carrying out these experiments, it was decided to remove the stilbene gas cell from on top of the SiPM array. The output of the Stilbene SiPM was subsequently connected to the oscilloscope and the trigger frequency function was selected. This was done to obtain a quantitative value for the number of triggers in each scenario. Table 7 shows the trigger rate for the four aforementioned scenarios.

Table 7. Performance of the optical isolation ring under various conditions

Ambient Light: On	Optical Isolation Ring	No Optical Isolation Ring
Black Electrical Tape: Yes	<10 Hz	~90k Hz
Black Electrical Tape: No	~68k Hz	~37k Hz

In this study, there were a few expected and a couple of unexpected results. A minimum trigger rate was expected when both the optical isolation ring and the black electrical tape were used. Ideally, the expectation would be for the greatest number of triggers to be recorded when there was no masking tape and no optical isolation ring, but the results point otherwise. A closer look at the pulse data points shows that the SiPMs were firing before even the signal came back to baseline, this resulted in multiple events being recorded above the trigger threshold. For example, if 3 events occur very close to each other in the time domain, the scope is registering this as a single trigger because the signal didn't come back to baseline before the other two events occurred. This results in an underreporting of the number of actual events observed by the SiPM. As for the other two cases where either the electrical tape or the optical isolation ring was not present, data suggests that there is a significant impact of the photons interacting from the sides of the SiPM as opposed to directly from above (vertically). It is worth mentioning that the interpretation of the results also depends on the directionality of the primary optical photon source.

4.5.2 Lab Check Source Calibration

For this experiment, ^{137}Cs disk source was used to collect the spectrum from a Stilbene gas cell. The gas cell was inside the holder for this experiment along with the optical isolation ring and the black electrical tape on top to prevent any external interference. Various thresholds were studied to obtain the best spectrum with minimal noise. For triggering purposes, a filter with 10 samples peaking (80 ns) and 0 samples for the flat top was designed in firmware to identify when the detector has triggered.

After establishing that the channel has triggered, the next step is to determine the number of samples that need to be integrated in order to determine the energy deposition from a pulse. Ideally, under low count scenarios, integration is generally carried out for 4-5 times the decay time of the pulse in order to capture the entire energy deposition. In our case though, the signal that is being processed is not the exact representation of the scintillator response from the stilbene cell. Therefore, it is

important to evaluate the number of coefficients in the filter/ the number of samples to be accumulated to plot the energy spectrum.

Initially, it was decided to use a triangular filter and convolve the pulse data to determine the amplitude of each pulse, this data would then be mapped to a given channel leading to an increment in the count. There were a couple of challenges that were faced in this approach. The first major challenge was pileup, this led to an overestimation of the energy of the pulse. Under some scenarios, the digitized pulse data that is collected for about 32.7 μs consists of multiple complete pulses that might again lead to an overestimation of the energy deposited. The second challenge that was faced was baseline estimations. Since the activity of the xenon gas is considerably high (10s of μCi), this leads to a baseline not being flat. On several occasions, the baseline turned out to be a falling edge of the previous pulse. This leads to improper baseline measurement while ultimately leads to incorrect energy estimations.

To remedy some of the challenges that were being faced, it was decided to use the accumulation technique for energy determination. In this process a fixed number of samples on a pulse are summed, this summation is then used to identify a channel on the spectrum to increment. This partially solves the challenge of pulse pileup. The second method implemented was to integrate the pulses starting only from sample 600. This is because the MATLAB code was set to collect baseline information from samples 1 to 600. As for determining the background of the pulses, it was observed that when data is being collected in coincidence mode, almost all the pulses have a similar baseline ADC value. Therefore, it was decided to use this same value across all the pulses. This prevents the chances of an incorrect baseline estimation which leads to errors in energy estimation.

Fig. 69 shows the spectrum obtained using digital integration over 600 points (4.8μs) in the pulse. It was decided to choose 600 points since it covers the majority of the pulse and ensures that the entire charge released is recorded. The threshold of the Stilbene gas cell was determined to be about 30 keV.

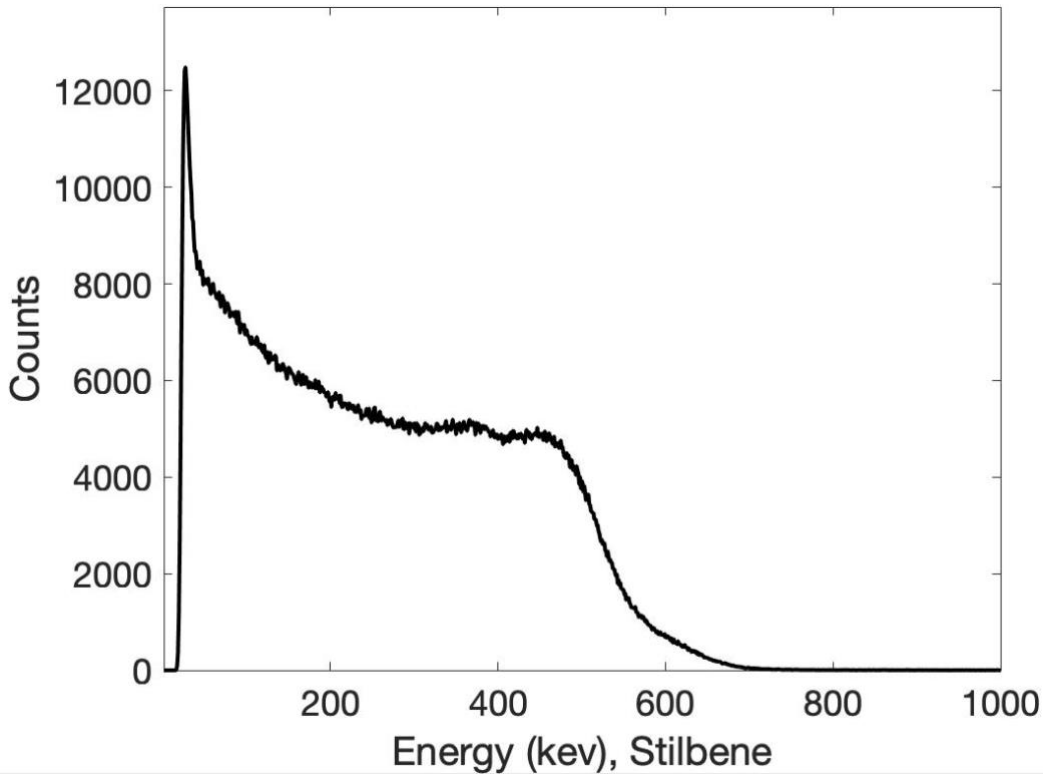

Fig. 69. The spectrum obtained from the Stilbene cell using a ^{137}Cs disk source

In the electron spectrum obtained from Stilbene, the Compton edge appears to be between 470 and 480 keV and the number of counts drops to almost zero at about the full energy of the source (662 keV). This shows that the Stilbene gas cell is performing as expected. There was a small bump that was observed right below 400 keV, this is assumed to be from the PLA material used for the holder from the detector.

4.6 Complete Detector Testing

In this section, the coincidence performance of the detection system will be initially tested using the SrI_2(Eu) and the Stilbene detectors. After which the results from the radioxenon injections will be discussed. This will involve exploring the coincidence spectra, absolute detection efficiencies, and memory effect of the detector. The final step in this research is the collection of a background spectrum to explore the singles rejection rate and calculation of the Minimum Detectable Concentration (MDC). These results will be explored using the ARSA and Xenon International gas processing

parameters. Similarly, both the experimental and MCNP estimated efficiency values are intended to be used in the MDC estimations.

4.6.1 ^{137}Cs Coincidence Backscatter (Stilbene + SrI_2(Eu))

One of the preliminary experiments performed to test the complete detection system is the coincidence backscatter using a ^{137}Cs source. In this setup, the expectation is to record events that trigger both the Stilbene gas cell as well as the SrI_2(Eu) photon detector within the 4.4 μs CTW. The sum of the energy deposition in both the scintillators should equate to 662 keV. Under ideal scenarios, this experiment is expected to yield a diagonal line along both the electron and photon energy axis. Extrapolating the line in both directions will result in an intersection at approximately 662 keV along both the axis. For this experiment, a 1μCi source was used rather than a 10 μCi source to prevent any coincidences between the scattered and 30 or 662 keV photon. Fig. 70a and Fig. 70b show the coincidence spectra obtained from the Stilbene and SrI_2(Eu) detection systems. It is brought to the reader's attention that the SrI_2(Eu) spectrum presented below is the summed result from the two detection bodies. 2 million coincidence pulses were recorded in the experiment. It is worth mentioning that 99.67% of these events happen to fall within the 1000 x 1000 keV coincidence spectrum. The remaining 0.33% of the events were cases where either the electron or photon energy deposition was over the prescribed energy range.

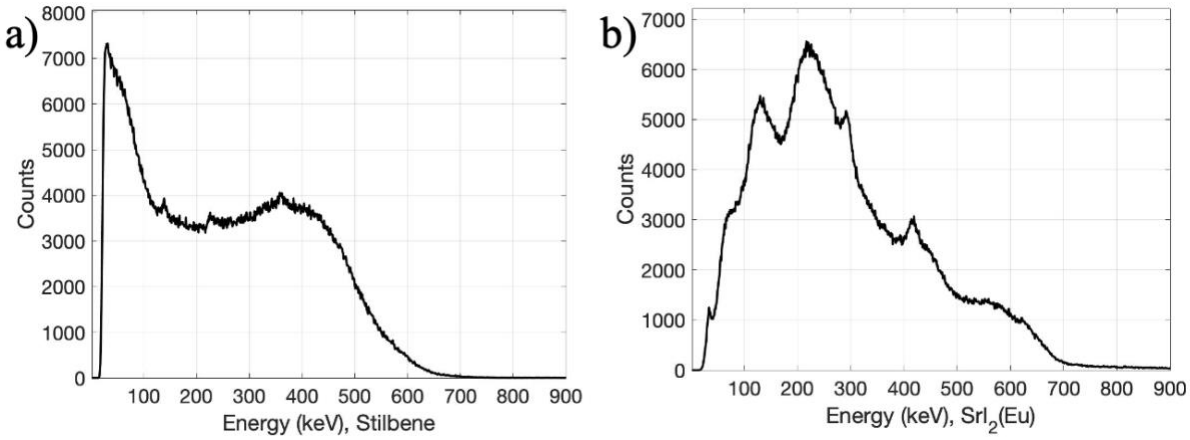

Fig. 70. The 1-D coincidence spectrum of a) Stilbene, and b) SrI_2(Eu)

Fig. 71 shows the 2-D coincidence spectrum for the ^{137}Cs backscatter experiment.

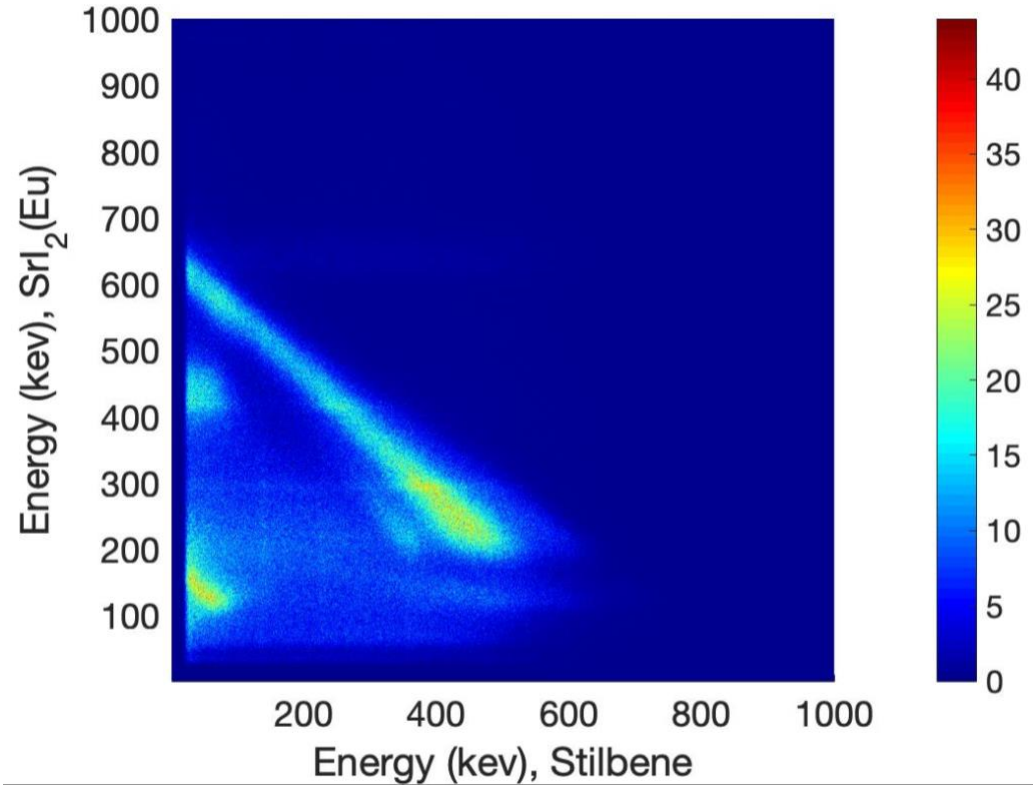

Fig. 71. The 2-D spectrum of the backscatter coincidence between the Stilbene gas cell and the two SrI_2(Eu) detectors

In the backscatter coincidence spectrum, the diagonal line featuring a sum energy deposition of 662 keV is clearly visible. This is again proof that the coincidence module is functioning as expected. Also visible are the hop spots at about 450 and 150 keV along the photon detector. These are mostly coincidence events between the Compton edge (477 keV) or the backscattered photon (185 keV) in the photon detector and the Stilbene cell. It is worth mentioning that a similar spectrum was obtained both for the CASP and the Stilbene-CZT detection system. Upon extrapolating the backscatter feature, it can be observed that the X and Y-axis intercepts are about 660 keV for both the electron and photon detector.

4.6.2 Radioxenon Measurements: ^{131m}Xe

3 ml of stable ultrapure ^{130}Xe sample was loaded in the syringe. This syringe was subjected to a thermal neutron flux of about 7.0 x 10^10 neutrons per cm^2 per sec for a duration of about 7 hours. After this, it was cooled for about 15 hours before being injected into the Stilbene gas cell. It is worth mentioning that the ^{131m}Xe radionuclide is the only isotope of xenon that can help in calibrating both the electron and photon detector because of the 31 and 129 keV X-ray and conversion electron monoenergetic peaks. The results from the electron and photon singles and coincidence events are discussed below. Also, efforts have been put into determining the absolute efficiency using methods identified in the Materials and Methods section.

4.6.2.1 Singles Measurements

In this section, the singles result from both the electron and photon detector will be discussed. 1 million counts were collected using each of the detection bodies using the DPP8. The singles electron and photon spectra are shown in Fig. 72a and Fig. 72b respectively.

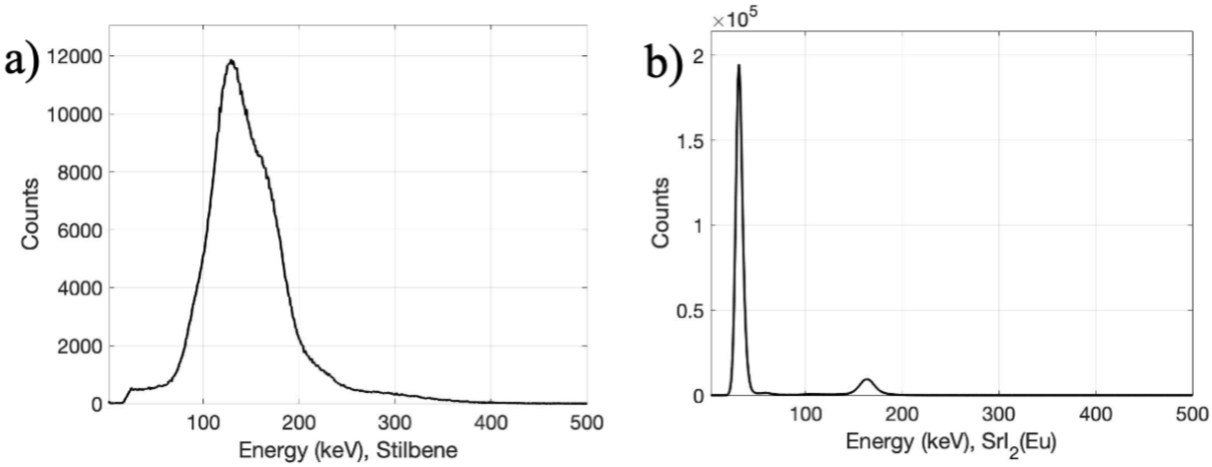

Fig. 72. The 1-D singles spectra of a) Stilbene, and b) SrI_2(Eu) using the ^{131m}Xe gas source

In the photon singles spectrum, the 31 keV X-ray, and the 164 keV gamma photon are clearly observed. In the electron singles spectrum, the 129 keV peak is observed. As for the 159 keV conversion electron, the peak is not observed because of the relatively poor energy resolution of the Stilbene cell compared to the PIPSBox but a feature can

be identified at about 150 keV which is representative of the peak from the second conversion electron. It is worth mentioning that this data was collected right after injection which resulted in a considerable amount of pileup events being recorded in the spectrum. These features can be identified in the energy range above 250 keV. SrI_2(Eu)-1 (dimmer) yielded an energy resolution of 28.4% and 11.48% FWHM for the X-ray and gamma photon. Analyzing the data from SrI_2(Eu)-2 (brighter) produced an energy resolution of 20.65% and 10.13% FWHM for the X-ray and gamma photon respectively. The energy resolution of the summed 31 keV X-ray and the 163 keV gamma photon was determined to be 23.33% and 10.76% FWHM respectively. The 129 keV conversion electron resolution is reported in the coincidence measurements section.

4.6.2.2 Coincidence Measurements

1 million coincidence events were recorded in this experiment. The 1-D coincidence spectrum from ^{131m}Xe is shown in Fig. 73a and Fig. 73b.

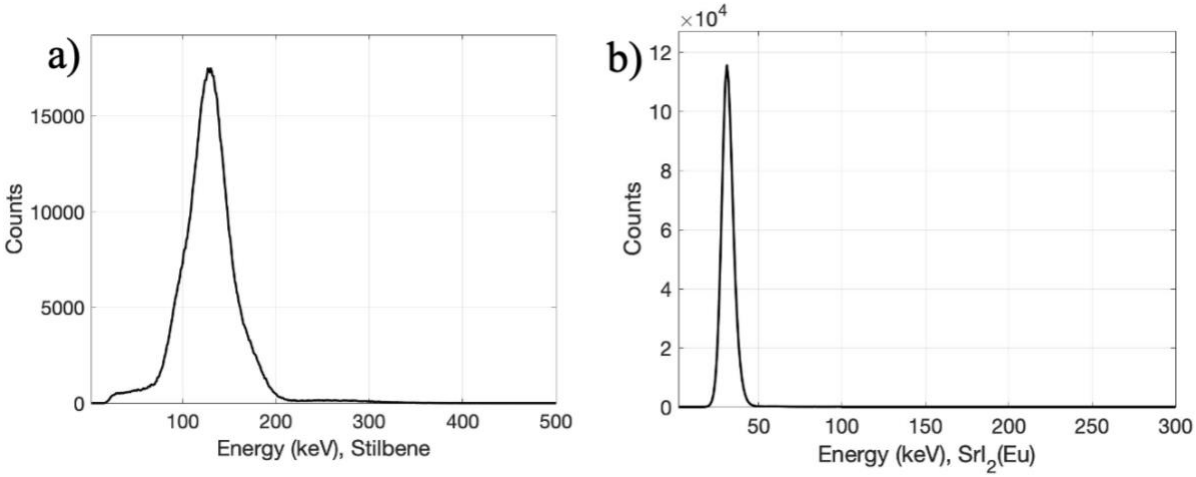

Fig. 73. The 1-D spectrum of a) Stilbene, and b) SrI_2(Eu) using the ^{131m}Xe gas source in coincidence mode

In the coincidence spectrum, the 30 keV X-ray, and the 129 keV conversion electron are clearly observed. The energy resolution of the conversion electron was determined to be 35.71% FWHM at 129 keV. The energy resolution of the summed 31 keV X-ray peak in coincidence was determined to be 23.64% FWHM. The absence of the 163 keV

gamma photon or the conversion electron at 159 keV goes on to show the functioning of the coincidence identification module. Fig. 74 shows the 2-D coincidence plot of the Stilbene-SrI_2(Eu) detection system using the ^{131m}Xe source.

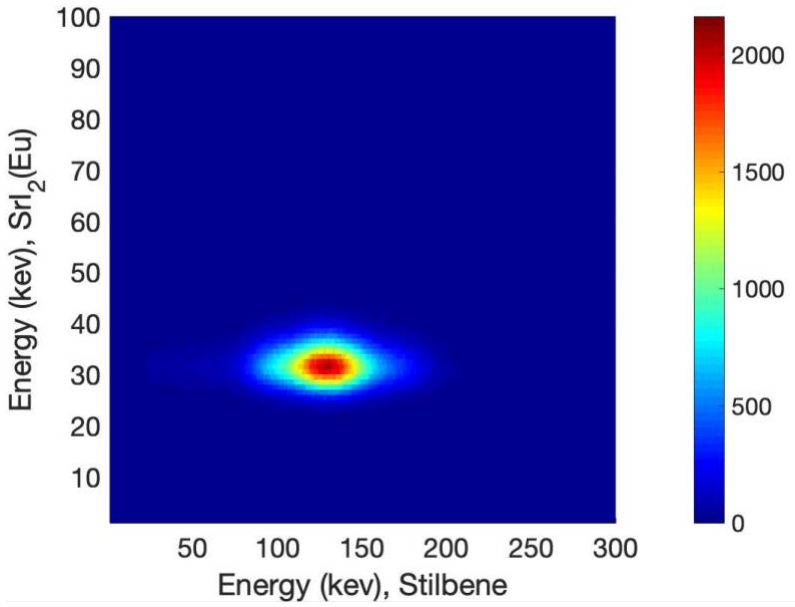

Fig. 74. The 2-D coincidence spectrum from the Stilbene-SrI_2(Eu) detection system using a ^{131m}Xe source

It is observed in the 2-D spectrum that all the counts are centered around a single region because of the monoenergetic emissions from both the electron and photon.

4.6.2.3 Absolute Efficiency

This section deals with the experimental absolute efficiency calculations based on the equations provided in chapter 3. For these equations to be implemented successfully, the number of counts under each peak is required to be determined precisely (129 and 159 keV). Since in the case of using a Stilbene detector, the energy resolution was not high enough to accurately determine the number of counts under each peak. This required the use of MCNP efficiencies and branching ratios from the literature to estimate the 30 keV X-ray efficiency. According to the MCNP simulations, the 129 and 159 keV conversion electron efficiencies are determined to be 96.8 and 97.2% respectively. Using this data and because no beta particles are released, the total activity

is calculated based on the beta singles count rate. Based on the total activity, photon branching ratios, and the X-ray singles count rate, the efficiency of the X-ray photon for the SrI_2(Eu) detection system was determined to be 10.4 ± 0.4 %. Table 8 shows the efficiencies of all the radiation of interest. The coincidence efficiency is simply calculated by multiplying the electron and photon efficiencies. Although the GEB parameters were used in MCNP it led to significant under estimation of the number of counts under the peak. This phenomenon is more pronounced for low-energy photons.

Table 8. Experimental and simulated efficiencies for the radiation of interest from ^{131m}Xe

Detector	Radiation (keV)	Absolute Efficiency (%)
Stilbene Gas Cell	129*	96.72 ± 0.01
	159*	97.17 ± 0.01
SrI_2(Eu)	31	10.4 ± 0.4
Coincidence Efficiencies (31 keV + 129 keV)		10.04 ± 0.38

* MCNP Simulation results

The error reported in MCNP is presented for 129 and 159 keV CE and error propagation was used to calculate the coincidence efficiency reported in the above table.

4.6.2.4 Memory Effect

Memory Effect is one of the prominent drawbacks which is plaguing several detection systems around the world, especially those employing a plastic gas cell. It was decided to evaluate the memory effect of the detection system using ^{131m}Xe because of its relatively long half-life which prevents any concerns of drastic changes in the activity while performing these measurements. The pump-and-flush technique was employed to perform the memory effect calculations. At the end of each run, the gas cell was connected to the roughing pump for 300 seconds to extract the gas sample in the cell. Pressures of about 2500 mTorr were achieved using the roughing pump. The initial count rate before applying the vacuum was found to be 90.07 ± 0.7 cps. After seven pump-and-flush rounds, the count rate saturated to about 0.063 ± 0.014 cps. Dividing

these two quantities yields a memory effect of 0.069 ± 0.015 %. This value is a little higher than the 0.045 ± 0.017% obtained using the Stilbene-CZT detection system but is within the prescribed error.

4.6.3 Radioxenon Measurements: $^{133/133m}$Xe

A 2.5 ml sample of ultrapure ^{132}Xe was drawn and irradiated in the thermal column of the TRIGA reactor at Oregon State University. In this process, both ^{133}Xe and ^{133m}Xe are produced. The metastable has a shorter half-life and upon release of the 199 keV conversion electron in coincidence with the 31 keV X-ray, it decays into ^{133}Xe. ^{133}Xe has a relatively complex decay structure because of two distinct coincidence decay chains. Post irradiation, the sample was cooled for a period of 16 hours before being injected into the detector. In this section, the singles spectrum, the coincidence spectrum, and the absolute efficiency calculations are discussed.

4.6.3.1 Singles Measurements

Singles measurements using the three detection bodies were collected right after the sample was injected into the Stilbene gas cell. A total of 2 x 10^6 single events were collected for the photon detector and 1 x 10^6 electron counts were collected using the stilbene channel. It is worth mentioning that when the sample is injected into the detector, the count rate is significantly high, about 35,000 to 40,000 cps were being detected. Fig. 75a and Fig. 75b shows the electron and photon singles spectra using $^{133m/133}$Xe.

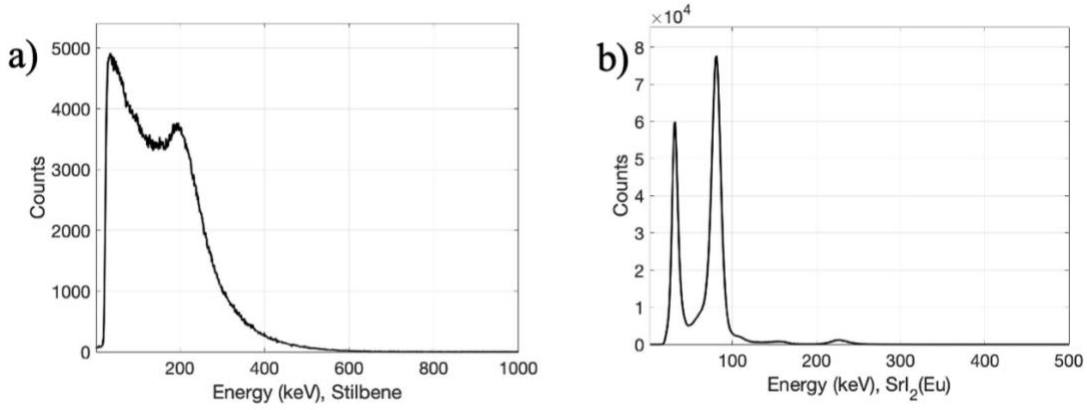

Fig. 75. The 1-D singles spectra of a) Stilbene, and b) SrI_2(Eu) using a $^{133m/133}$Xe source

In the singles spectrum from the electron and photon detector, a number of features are observed. On the electron front, the 199 keV conversion electron is clearly observed sitting on top of a beta continuum. Although the 45 keV conversion electron is not clearly visible, the X-ray gated coincidence spectrum collected a few days later shows the 45 keV conversion electron. Closely observing the energy spectrum from the electron, it can be seen that the number of counts does not drop to zero at about 400 keV. This is because of the extensive pileup that was observed because of the high activity of the sample.

On the photon front, the 30 keV X-ray and the 81 keV gamma photon are observed. Apart from that, some low probability gamma photons like the 160 and 233 keV are also identified in the singles spectrum. The number of counts under the 31 and 81 keV photons is also of some interest. The probability of the decay scheme involving the release of the X-ray is significantly higher compared to the gamma photon, this also holds true for ^{133}Xe. As for ^{133m}Xe, the release of the 31 keV X-ray is the only mechanism with significant photon yield identified. Therefore, the relatively low number of X-ray counts compared to the gamma counts can be attributed to the high attenuation/ low detection efficiency of low energy X-rays compared to the 81 keV gamma photon. The energy resolution of the X-ray, 81 keV gamma photon was determined to be 28.15, 17.07% FWHM using SrI_2(Eu)-1 (dimmer) respectively. On the other hand, the energy resolution of the X-ray, 81 keV gamma photon was determined to be 20.71, 13.13% FWHM using SrI_2(Eu)-2 (brighter) respectively. The spectra from both these detectors were summed to obtain a summed spectrum, this effort yielded an energy resolution of 23.93, 14.84% FWHM for the X-ray, gamma photon respectively.

4.6.3.2 Coincidence Measurements

In this section, the coincidence spectral features of $^{133m/133m}$Xe are discussed. It is worth mentioning that, after injecting the sample in the detector, it was decided to wait for about 96 hours before performing coincidence counting. This was done to allow enough

time to pass in an effort to reduce pileup events. Fig. 76a and Fig. 76b show the coincidence electron and photon spectra from the Stilbene and $SrI_2(Eu)$ detectors.

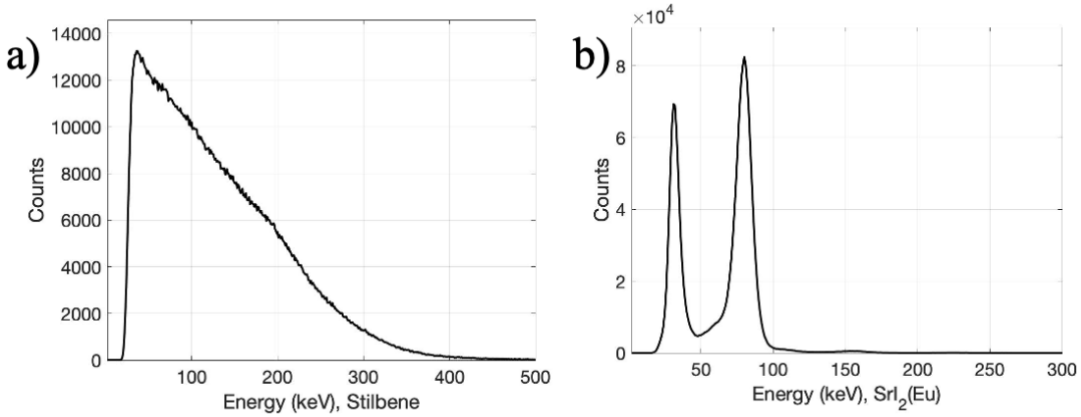

Fig. 76. The 1-D coincidence spectra of a) Stilbene, and b) $SrI_2(Eu)$ using the $^{133m/133}$Xe gas source

In the coincidence spectra as well, all the important features are clearly identified. A significant difference is observed in the Stilbene spectrum where the number of counts approaches zero at about 400 keV. This indicates that the pileup has considerably reduced after the 96-hour cooldown period. Although the 199 keV conversion electron peak is not prominent, a slight increase in counts is observed at about 200 keV. As for the photon spectra, two sharp peaks are observed at about 31 keV and 81 keV. Fig. 77 shows the 2-D coincidence spectrum for $^{133m/133}$Xe.

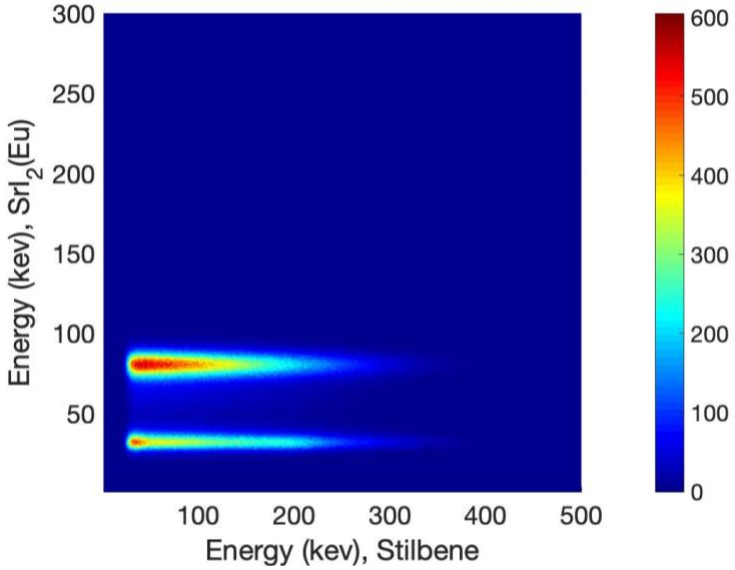

Fig. 77. The 2-D coincidence spectrum using a $^{133m/133}$Xe source

The X-ray gated and gamma gated electron spectra are shown in Fig. 78a and Fig. 78b respectively.

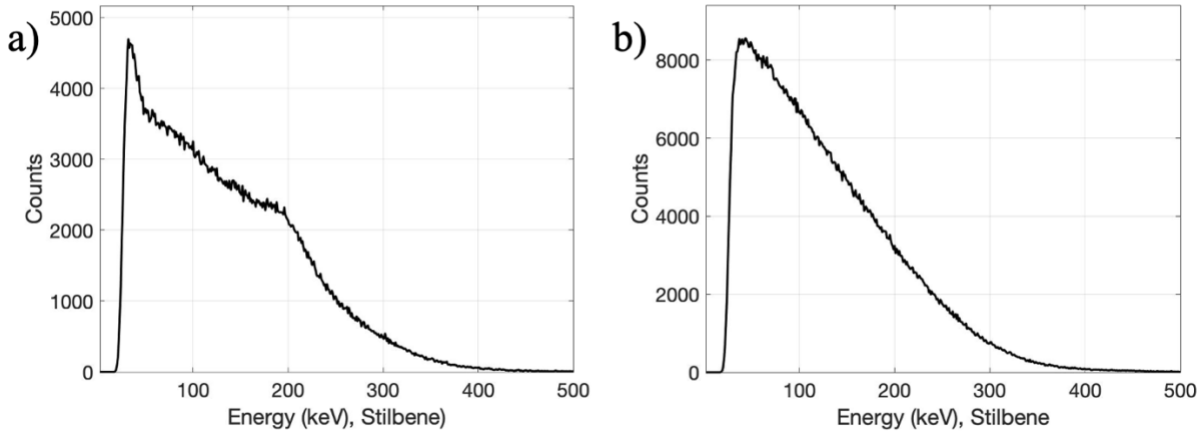

Fig. 78. The 1-D coincidence spectra from the Stilbene detector showing gating between a) the 31 keV X-ray, 45 keV Conversion Electron, and 346 keV β_{max}, b) the 81 keV gamma and 346 keV β_{max}

In the X-ray gated spectrum, the 199 keV feature is distinctly observed as compared to the summed stilbene spectrum. The energy resolution of the 199 keV peak couldn't be determined because of the lack of a distinct peak. In the X-ray gated spectrum, the 45 keV conversion electrons were also clearly identified. As for the gamma gated spectrum, a smooth beta continuum is observed.

4.6.3.3 Trigger Walking

For the purpose of triggering a detection system, triangular filters are extremely useful. Using these filters, the user defines a threshold over which the system is required to trigger. This methodology is called leading-edge triggering. This energy threshold-based triggering presents a problem when a wide range of energies are required to be processed in a coincidence counting environment. When a Charge-Sensitive Preamplifier (CSP) is used, the rising edge of the pulse is defined by the capacitance of the device. This means when the threshold is fixed, the low energy pulse takes a little longer to cross the threshold and trigger the detector compared to a high energy signal. This additional time for low-energy pulses to trigger the system is called trigger

walking. This phenomenon is illustrated in Fig. 79 where two different signals can be seen crossing the threshold at two different times.

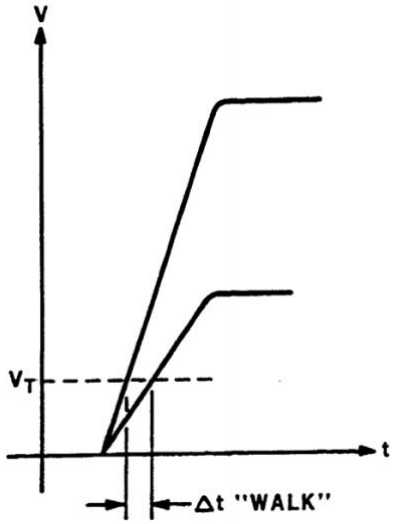

Fig. 79. Illustrating the process of trigger walking

This presents a serious problem while working with coincidence-based detection systems if the CTW elapses before the low energy pulse can even trigger the system. The CTW was reduced to 300 samples (2.4 µs) to observe the performance of the system. The gamma and 2-D coincidence spectrum from $^{133/133m}$Xe are shown in Fig. 80a and Fig. 80b respectively.

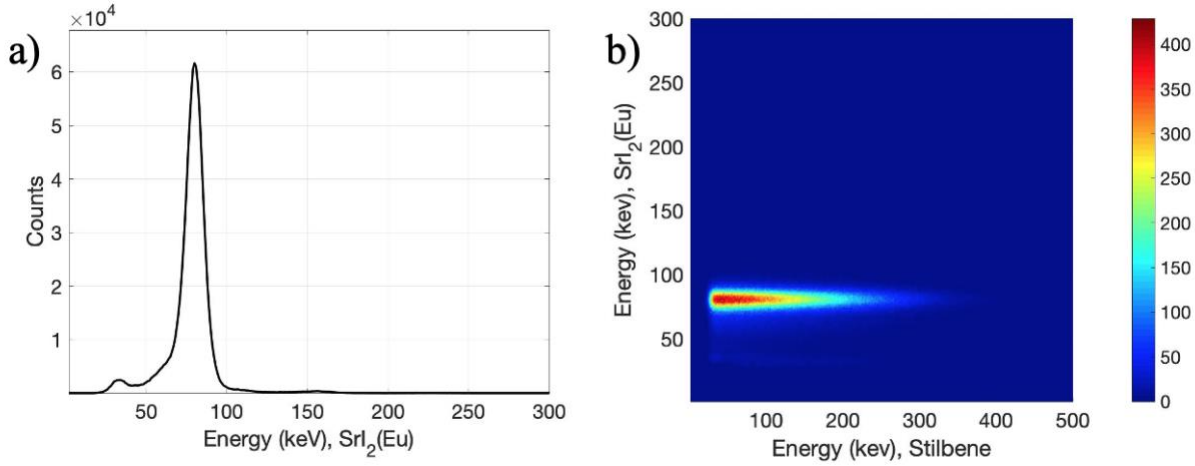

Fig. 80. a) 1-D coincidence photon spectra showing only the 80 keV peak, and b) the coincidence spectrum from $^{133m/133}$Xe at a CTW of 2.4 µs

In the coincidence spectra at reduced CTW, only the 81 keV photon triggered the system within the CTW and most of the X-ray events were lost because the photon detector did not trigger before the CTW elapsed. This forced the system to classify the electron triggers as singles events. This study demonstrated the experimental implications of trigger walking and CTW settings while working with relatively slow scintillators. Therefore, it is always recommended to maintain a CTW sufficiently long to account even for low energy triggers. This problem was not faced with the electron detector because no charge-sensitive preamplifier was used in the case of the Stilbene detector.

4.6.3.4 Absolute Efficiency

Like in the case of ^{131m}Xe, the absolute efficiency of $^{133/133m}$Xe is also required to be determined for accurate quantification of the detector's MDC. A number of simplifications have been made to facilitate the calculation of these efficiencies. The gas sample was allowed to decay for about 8 days to minimize the number of counts from ^{133m}Xe. This was done to assume the contribution of the 199 keV conversion electron to be zero. Since accurate quantification of the number of counts under this peak was not feasible, it was decided to allow significant decay of ^{133m}Xe. Some other simplifications were also made like using the MCNP efficiencies above 30 keV (Stilbene threshold) for the 45 keV conversion electron. Using this source, the efficiency of the 31 keV X-ray, 81 keV gamma, and the 346 keV β_{max} is required to be calculated.

Initially, the singles spectra (100,000 counts each) from both the photon detectors were collected. After this, the number of counts under the 81 keV was determined in both the detectors. Dividing the number of counts by the live time provides the count rate for the 81 keV photons from the detectors. The arithmetic mean of both these values was computed and multiplied by 2, since there are two detectors, this yielded a count rate of 351.1 ± 0.7 counts per second for the 81 keV photon. Similarly, the count rates from the Stilbene and SrI_2(Eu) detectors were determined for the 81 keV gamma in coincidence with the 346 keV β_{max}. This yielded a coincidence count rate (gamma) of

218.8 ± 0.9 counts per second. Using these two values, the beta efficiency can be computed by dividing the coincidence and the gamma singles count rate. This resulted in a 346 keV β_{max} efficiency to be 62.32 ± 0.27%. It is worth noting that the beta efficiency is within 3% of the simulated efficiencies using MCNP.

Using the value of the beta efficiency, the gamma efficiency is calculated taking into account the 45 keV conversion electron efficiency and branching ratio. Primarily, the electron singles counts are measured, this yielded a count rate of 2259 ± 7 cps. Using this value, the total activity in the sample was calculated to be 3229 ± 10 Bq. Using the branching ratio of 0.37 for the gamma photons and the gamma singles count of 351.1 ± 0.7 cps which was previously determined, the efficiency of the 81 keV gamma photon is determined to be 28.61 ± 0.10%.

The last efficiency to be calculated is that of the 31 keV X-ray, although this value was calculated for ^{131m}Xe, it was decided to calculate the value again for ^{133}Xe in the interest of data validation. The count rate for the 31 keV X-rays from the two-photon detectors was determined to be 175.0 ± 0.7 counts per second. Using an X-ray branching ratio of 0.488, the total activity of the sample, and the X-ray singles count rate, the efficiency of the 31 keV X-ray was determined to be 11.1 ± 0.3%. It is worth mentioning that the 31 keV efficiency for ^{133}Xe is within the error limit when compared to ^{131m}Xe. Table 9 shows all the individual and coincidence efficiencies for the three regions of interest.

Table 9. Experimental and simulated efficiencies for the radiation of interest from $^{133m/133}$Xe

Detector	Radiation (keV)	Absolute Efficiency (%)
Stilbene Gas Cell	45*	36.33 ± 0.07
	199*	97.21 ± 0.01
	346	62.32 ± 0.27
SrI_2(Eu)	31	11.1 ± 0.3
	81	28.6 ± 0.1

Coincidence Efficiencies (31 keV x 199 keV)	10.78 ± 0.33
Coincidence Efficiencies (81 keV x 346 keV)	17.82 ± 0.09
Coincidence Efficiencies [31 keV x (45 keV+ 346 keV)]	8.43 ± 0.24

* MCNP Simulation results

The error reported in the MCNP simulations was used for these results and error propagation was applied for all the calculations. It is interesting to note that the efficiency of the 81 keV photon was almost 5% higher than that reported for the PIPS-SrI_2(Eu) detection system even though the solid angle of the Stilbene-SrI_2(Eu) detector was 0.14π lower than the PIPS-SrI_2(Eu) system.

4.6.4 Radioxenon Measurements: ^{135}Xe

^{135}Xe is the last radioxenon of interest, this radionuclide prominently releases a 910 keV β_{max} in conjunction with a 250 keV gamma photon. Apart from that, about 5.7% of the time, ^{135}Xe also releases an X-ray in coincidence with a 214 keV conversion electron and a 910 keV β_{max}. This radionuclide also has the shortest half-life among all the radionuclides of interest of only 0.38 days. A 1.5 mL sample of ultra-pure ^{134}Xe was drawn in a syringe and irradiated in the TRIGA reactor for 7 hours after which it was cooled for about 16 hours. This was followed by injecting the gas sample in the Stilbene gas cell for data collection and analysis.

4.6.4.1 Singles Measurements

In the singles measurement, the performance of each detection body is studied. 1 x 10^6 counts were collected for each detection medium. Fig. 81a and Fig. 81b show the summed photon singles and the electron spectra respectively.

The spectra from both the photon detectors were summed together to obtain the summed photon spectrum. As can be seen in the photon spectrum, all the features are clearly identified. A sharp peak is observed at 250 keV and a Compton edge at about

140 keV. Also seen in the spectrum is the X-ray at about 30 keV. It must be pointed out that, although this mechanism is not prevalent, this feature was observed in both the singles and coincidence spectrum. As for the stilbene spectrum, a smooth beta continuum is observed from about 30 keV all the way to about 900 keV, which is also the maximum energy of the emitted beta.

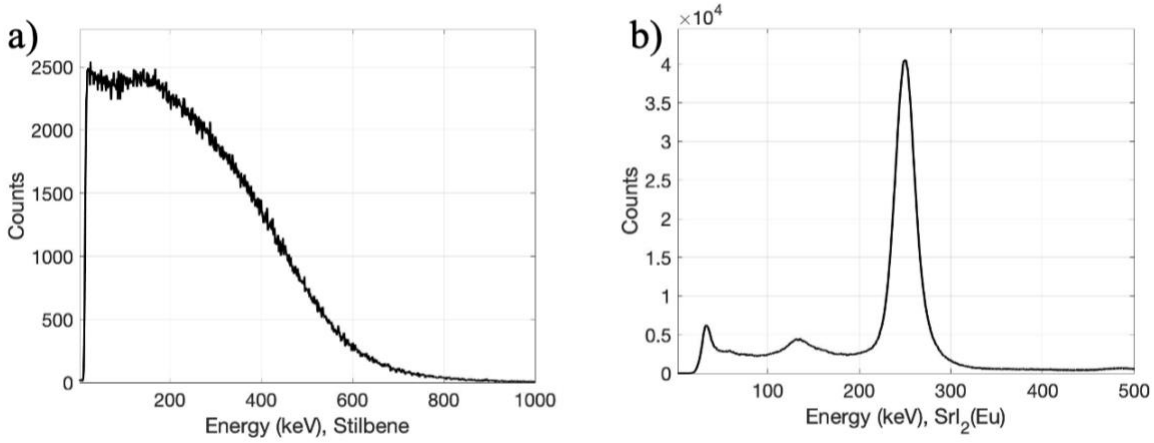

Fig. 81. The 1-D singles spectra of a) Stilbene, and b) SrI_2(Eu) using the ^{135}Xe gas source

The energy resolution of the 250 keV peak for SrI_2(Eu)-1 (dimmer) was determined to be 10.17% FWHM. As for the 250 keV resolution for SrI_2(Eu)-2 (brighter), the FWHM was calculated to be 9.01%. After both the spectra were summed, the sum 250 keV energy resolution of 9.72% FWHM was determined. A small X-ray peak was also observed in the spectrum with a resolution of about 24.68%.

4.6.4.2 Coincidence Measurements

4 million coincidence counts were collected to produce the 2-D coincidence spectrum. Fig. 82a and Fig. 82b show the 1-D coincidence spectrum from the electron and photon detector.

In the electron spectrum, the beta continuum is clearly observed, and the number of counts drops to almost 0 at about 900 keV. In the photon spectrum, the X-ray, Compton edge, and the full energy peak are clearly observed. It is worth mentioning that features

observed in the singles spectrum and the coincidence spectrum are almost the same. Fig. 83 shows the 2-D coincidence spectrum from ^{135}Xe. As expected, most of the counts are concentrated around the 250 keV gamma peak, a small fraction of coincidence counts is also observed in the X-ray and 214 CE/ beta region.

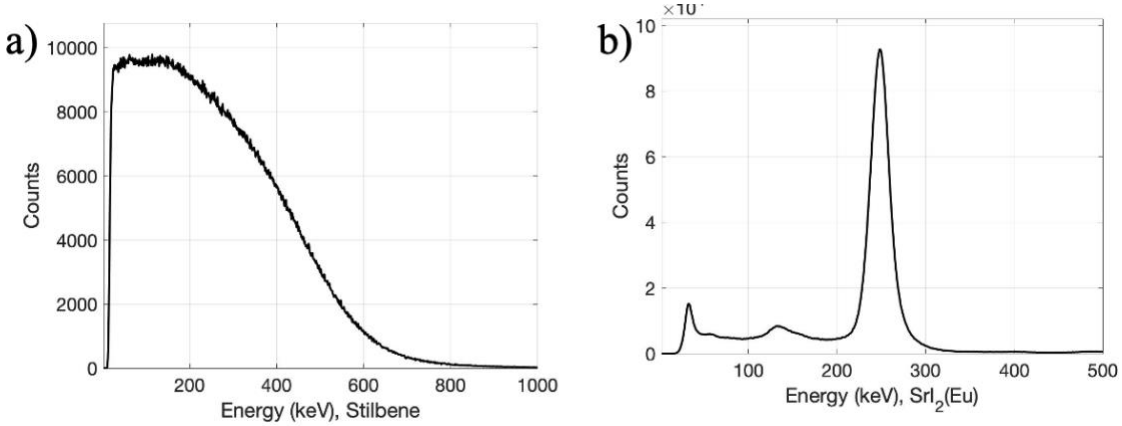

Fig. 82. The 1-D coincidence spectra of a) Stilbene, and b) SrI_2(Eu) using the ^{135}Xe gas source

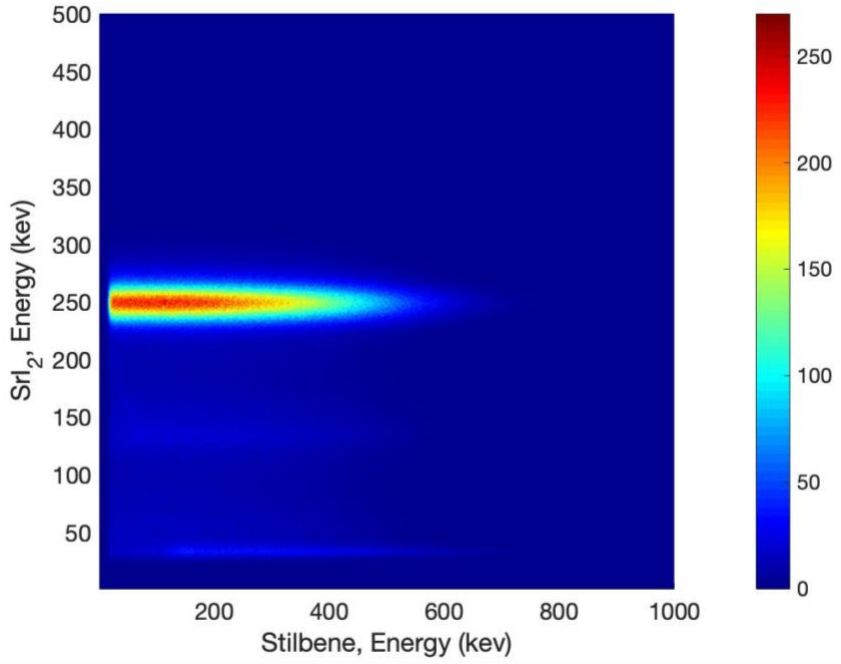

Fig. 83. The 2-D coincidence spectrum using a ^{135}Xe source

4.6.4.3 Absolute Efficiency

The absolute efficiency is important to calculate since these values are extremely useful in the MDC calculations. It is worth mentioning that only the counts under the peak are accounted for in these calculations. There are a couple of assumptions that were made for these calculations, the 214 keV conversion electron efficiency was calculated using MCNP simulations. The branching ratio of the 214 keV CE in conjunction with the X-ray and 910 keV beta was taken to be 5.7% from literature. The beta efficiency was initially calculated using the ratio of the number of coincident counts and gamma singles. This value in conjunction with the conversion electron efficiency and branching ratio was then used to calculate the total activity in the gas cell. Once the total activity was determined, the efficiency of the gamma photon and the X-ray were determined. It is worth mentioning while calculating the MDC of ^{135}Xe, there is no dedicated region of interest for the X-ray/ 214 keV conversion electron because of its small branching ratio. Table 10 shows all the individual and coincidence efficiencies for ^{135}Xe.

Table 10. Experimental and simulated efficiencies for the radiation of interest from ^{135}Xe

Detector	Radiation (keV)	Absolute Efficiency (%)
Stilbene Gas Cell	214*	97.20 ± 0.01
	910	80.37 ± 0.74
$SrI_2(Eu)$	31	8.94 ± 0.38
	250	17.53 ± 0.21
Coincidence Efficiencies (250 keV x 910 keV β_{max})		14.08 ± 0.21
Coincidence Efficiencies [31 keV x (214 keV+ 910 keV)]		8.87 ± 0.56

* MCNP Simulation results

It is worth noting that although the efficiency of the 31 keV is about 2% lower than that calculated in previous experiments, it should be pointed out that this value is within the

error range when the 31 keV efficiency was determined for ^{135}Xe using the PIPS-SrI_2(Eu) detection system in the past. Analyzing the simulation and experimental results it can be pointed out that despite using the Gaussian Energy Broadening feature in MCNP the Compton continuum is slightly underestimated in simulations when compared to experimental results.

4.6.5 Background and Minimum Detectable Concentration

Background measurements play an essential part in the characterization of a detection system. This allows the estimation of the MDC of a detection system, an essential characterization parameter for radioxenon detection systems. Therefore, for this study, it was decided to collect the coincidence background for about 48 hours. Fig. 84 shows the collected 2-D coincidence background for 48 hours. It is worth mentioning that while recording the background it was assumed that there was no significant change in the ambient temperature since a change in temperature results in variable SiPM gain.

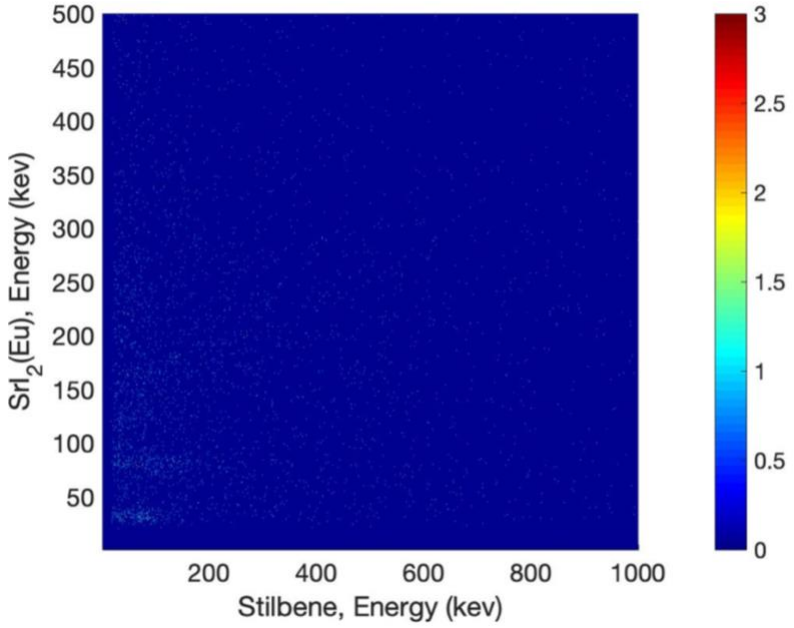

Fig. 84. A 48-hour background using the Stilbene-SrI_2(Eu) detection system

After this, ROIs were defined, for monoenergetic emissions (electrons and photons) a 3σ full-width window was defined centered around the peak. This data stems from the resolution measurements that were carried out for each monoenergetic peak. For the 199 keV peak from ^{133m}Xe, it was decided to appropriately scale the resolution

according to the data from the Stilbene-CZT detection system, since the scarce number of counts under the peak made it challenging to determine the energy resolution. For the beta emissions, the ROI is defined from 1 to β_{max}. The background coincidence count rate was determined to be 0.0174 ± 0.0003 counts per second. The background rejection percentage was determined to be about 98.89 ± 0.02%. It is worth mentioning that for these calculations an energy range of 1000 and 500 keV was considered for the electron and photon detectors respectively.

For the MDC calculations, a few modifications were made to the basic MDC as explained in section 2.3.1. Based on these assumptions, the interference counts, and memory effect counts are considered to be zero. The error in the counts is assumed to be Poisson. This means the σ_{BckCnt} term is simply the square root of the background. MDC values are reported using both the ARSA, and Xenon International gas processing parameters. Two sets of results are again reported based on experimental and simulated efficiencies for the electrons and photons of interest. Table 11 shows the MDC results obtained using the Stilbene-SrI_2(Eu) detection system.

Table 11. Simulated and experimental MDC values for the four radioxenon of interest using the ARSA and Xenon International gas processing parameters

Isotope	MDC - ARSA Gas Processing (mBq/m^3)		MDC - Xenon International Gas Processing (mBq/m^3)	
	Simulated	Experimental	Simulated	Experimental
^{131m}Xe	0.0820 ± 0.0003	0.28 ± 0.03	0.0454 ± 0.0001	0.15 ± 0.02
^{133m}Xe	0.0626 ± 0.0003	0.21 ± 0.03	0.0343 ± 0.0001	0.12 ± 0.02
^{133}Xe	0.2262 ± 0.0017	0.54 ± 0.05	0.1250 ± 0.0009	0.30 ± 0.03
^{135}Xe	0.9598 ± 0.0256	1.44 ± 0.15	0.4976 ± 0.0132	0.74 ± 0.08

It can be observed from the MDC results that all the four radioxenons of interest have achieved an MDC below the 1mBq/m^3 as prescribed by the CTBTO. Using the ARSA gas processing parameters resulted in a higher MDC because of the low air sample processing volume compared to the Xenon International. Simulated MDC results are also higher than the experimental result because MCNP over-estimated the detection efficiency, especially for photons. It is also worth mentioning that the background measurements are also heavily dependent on the location where these measurements are being carried out and as such are subject to considerable variation.

5. CONCLUSION AND FUTURE WORK

A prototype radioxenon detection system using two $SrI_2(Eu)$ detectors and a Stilbene gas cell were conceptualized, designed, developed, and tested at Oregon State University. Since scintillator elements were used for both the electron and photon detector, SiPMs were employed for the optical photon readout. The $SrI_2(Eu)$ detectors were initially characterized using various lab check sources and a variable energy X-ray source. This was followed by the characterization of the Stilbene cell using the Compton edge from the 662 keV peak. After this, the entire detection system was characterized, this included testing the coincidence detection module under multiple conditions followed by experimentally detecting the backscatter coincidence feature using a ^{137}Cs source. Stable xenon samples were then irradiated in the Oregon State University TRIGA reactor and tested using the Stilbene-$SrI_2(Eu)$ detection system. All the features from the four radioxenon of interest were uniquely identified. The use of high energy resolution materials like $SrI_2(Eu)$ enabled defining a smaller ROI which has a direct effect on the MDC of the system. It is worth mentioning that the MDC for all four radioxenon of interest was calculated to be below $1mBq/m^3$ as stipulated by the CTBTO. Memory effect was evaluated and compared to the state-of-the-art detection systems on the IMS network which predominantly use plastic scintillators. This work yielded a memory effect of about $0.069 \pm 0.015\%$ which is almost a 70x improvement compared to plastic scintillators. Some future work that is readily identified using this detection system include:

- the testing of the detection system using TRIGA generated mixed radioxenon sources
- the use of temperature sensitive microcontroller for SiPM gain adjustments
- the study of a constant fraction discriminator in real-time to eliminate trigger walking
- using a radon generator to evaluate the MDC taking into account the interference in the ROI
- testing the detection system using an ARSA/ Xenon International gas processing system to detect actual atmospheric samples

Apart from the experimentation work that was carried out using the Stilbene-SrI_2(Eu) detection system, a significant effort has also been put into the optical transport simulations using both Geant4 and DETECT2000. Although initial results indicate that the use of either of these simulation toolkits yields the same results, it is brought to the reader's attention that Geant4 is positioned better compared to DETECT2000 taking into account the ionization depth-dependent optical photon generation process. Further improvements to the detection system can also be achieved using the Stilbene gas cell in conjunction with a thru-hole photon detection system (similar to the $CeBr_3$ detector previously discussed). This design is aimed at further improving the detector performance in terms of efficiency which is directly correlated to the MDC of the system. From a detection standpoint, it is recommended for future detectors to explore options involving maintaining a high electron and photon detection efficiency or new electron/ photon detection materials with improvements in energy resolution.

Bibliography

1. “The Treaty: Comprehensive Nuclear-Test-Ban Treaty Organization Preparatory Commission.” [Online]. Available: https://www.ctbto.org/the-treaty/. [Accessed: 02/21/2021]

2. “Verification Regime: Comprehensive Nuclear-Test-Ban Treaty Organization Preparatory Commission.” [Online]. Available: https://www.ctbto.org/verification-regime/. [Accessed: 02/21/2021]

3. “World Map: Comprehensive Nuclear-Test-Ban Treaty Organization Preparatory Commission.” [Online]. Available: https://www.ctbto.org/map/. [Accessed: 10/09/2019]

4. R. Perkins and L. Casey, “Radioxenons: Their role in monitoring a Comprehensive Test Ban Treaty,” DOE/RL--96-51, PNNL-SA--27750, 266641, Jun. 1996. doi: 10.2172/266641.

5. M. B. Kalinowski and C. Pistner, “Isotopic signature of atmospheric xenon released from light water reactors,” Journal of Environmental Radioactivity, vol. 88, no. 3, pp. 215–235, Jan. 2006, doi: 10.1016/j.jenvrad.2006.02.003.

6. M. B. Kalinowski and M. P. Tuma, “Global radioxenon emission inventory based on nuclear power reactor reports,” Journal of Environmental Radioactivity, vol. 100, no. 1, pp. 58–70, Jan. 2009, doi: 10.1016/j.jenvrad.2008.10.015.

7. M. B. Kalinowski et al., “Discrimination of Nuclear Explosions against Civilian Sources Based on Atmospheric Xenon Isotopic Activity Ratios,” Pure Appl. Geophys., vol. 167, no. 4–5, pp. 517–539, May 2010, doi: 10.1007/s00024-009-0032-1.

8. K. B. Olsen et al., “Noble gas migration experiment to support the detection of underground nuclear explosions,” J Radioanal Nucl Chem, vol. 307, no. 3, pp. 2603–2610, Mar. 2016, doi: 10.1007/s10967-015-4639-7.

9. I. Hoffman et al., “Changes in radioxenon observations in Canada and Europe during medical isotope production facility shut down in 2008,” Journal of Radioanalytical and Nuclear Chemistry, vol. 282, no. 3, pp. 767–772, Dec. 2009, doi: 10.1007/s10967-009-0235-z.

10. P. W. Eslinger, J. I. Friese, J. D. Lowrey, J. I. McIntyre, H. S. Miley, and B. T. Schrom, “Estimates of radioxenon released from Southern Hemisphere medical isotope production facilities using measured air concentrations and atmospheric transport modeling,” Journal of Environmental Radioactivity, vol. 135, pp. 94–99, Sep. 2014, doi: 10.1016/j.jenvrad.2014.04.006.

11. P. R. J. Saey, T. W. Bowyer, and A. Ringbom, “Isotopic noble gas signatures released from medical isotope production facilities—Simulations and measurements,” Applied Radiation and Isotopes, vol. 68, no. 9, pp. 1846–1854, Sep. 2010, doi: 10.1016/j.apradiso.2010.04.014.

12. T. W. Bowyer, R. Kephart, P. W. Eslinger, J. I. Friese, H. S. Miley, and P. R. J. Saey, “Maximum reasonable radioxenon releases from medical isotope production facilities and their effect on monitoring nuclear explosions,” Journal of Environmental Radioactivity, vol. 115, pp. 192–200, Jan. 2013, doi: 10.1016/j.jenvrad.2012.07.018.

13. C. Johnson, J. Lowrey, S. Biegalski, and D. Haas, “Regional transport of radioxenon released from the Chalk River Laboratories medical isotope facility,” Journal of Radioanalytical and Nuclear Chemistry, vol. 305, no. 1, pp. 207–212, Jul. 2015, doi: 10.1007/s10967-015-4077-6.

14. P. R. J. Saey et al., “The influence on the radioxenon background during the temporary suspension of operations of three major medical isotope production facilities in the Northern Hemisphere and during the start-up of another facility in the Southern Hemisphere,” Journal of Environmental Radioactivity, vol. 101, no. 9, pp. 730–738, Sep. 2010, doi: 10.1016/j.jenvrad.2010.04.016.

15. M. Auer, T. Kumberg, H. Sartorius, B. Wernsperger, and C. Schlosser, “Ten Years of Development of Equipment for Measurement of Atmospheric Radioactive Xenon for the Verification of the CTBT,” Pure and Applied Geophysics, vol. 167, no. 4–5, pp. 471–486, May 2010, doi: 10.1007/s00024-009-0027-y.

16. C. B. Sivels, J. I. McIntyre, T. W. Bowyer, M. B. Kalinowski, and S. A. Pozzi, “A review of the developments of radioxenon detectors for nuclear explosion monitoring,” Journal of Radioanalytical and Nuclear Chemistry, vol. 314, no. 2, pp. 829–841, Nov. 2017, doi: 10.1007/s10967-017-5489-2.

17. A. Ringbom, T. Larson, A. Axelsson, K. Elmgren, and C. Johansson, “SAUNA—a system for automatic sampling, processing, and analysis of radioactive xenon,” Nuclear Instruments and Methods in Physics Research Section A: Accelerators, Spectrometers, Detectors and Associated Equipment, vol. 508, no. 3, pp. 542–553, Aug. 2003, doi: 10.1016/S0168-9002(03)01657-7.

18. Yu. V. Dubasov et al., “The АРИКС-01 Automatic Facility for Measuring Concentrations of Radioactive Xenon Isotopes in the Atmosphere,” Instruments and Experimental Techniques, vol. 48, no. 3, pp. 373–379, May 2005, doi: 10.1007/s10786-005-0065-3.

19. V. V. Prelovskii, N. M. Kazarinov, A. Yu. Donets, V. Yu. Popov, I. Yu. Popov, and N. V. Skirda, “The ARIX-03F mobile semiautomatic facility for measuring low concentrations of radioactive xenon isotopes in air and subsoil gas,” Instruments and Experimental Techniques, vol. 50, no. 3, pp. 393–397, May 2007, doi: 10.1134/S0020441207030165.

20. J. I. McIntyre et al., “Measurements of ambient radioxenon levels using the automated radioxenon sampler/analyzer (ARSA),” Journal of Radioanalytical and Nuclear Chemistry, vol. 248, no. 3, pp. 629–635, 2001.

21. J. C. Hayes, “Requirements for Xenon International: Revision 1,” Pacific Northwest National Laboratory (PNNL), Richland, WA (US), PNNL-22227 (Rev 1), Dec. 2015.

22. J. C. Hayes et al., “Requirements for Xenon International (Rev. 2),” PNNL--22227-Rev.2, 1545382, Aug. 2018. doi: 10.2172/1545382.

23. J. C. Hayes, W. Harper, M. Panisko, and M. W. Cooper, “Xenon International Overview,” PNNL--27660, 1472068, Jun. 2018. doi: 10.2172/1472068.

24. J.-P. Fontaine, F. Pointurier, X. Blanchard, and T. Taffary, “Atmospheric xenon radioactive isotope monitoring,” Journal of Environmental Radioactivity, vol. 72, no. 1–2, pp. 129–135, Jan. 2004, doi: 10.1016/S0265-931X(03)00194-2.

25. L. Ranjbar, A. T. Farsoni, and E. M. Becker, “135 Xe measurements with a two-element CZT-based radioxenon detector for nuclear explosion monitoring,” Journal of Environmental Radioactivity, vol. 169–170, pp. 221–228, Apr. 2017, doi: 10.1016/j.jenvrad.2016.12.003.

26. A. T. Farsoni, B. Alemayehu, A. Alhawsawi, and E. M. Becker, “A compton-suppressed phoswich detector for gamma spectroscopy,” Journal of Radioanalytical and Nuclear Chemistry, vol. 296, no. 1, pp. 63–68, Apr. 2013, doi: 10.1007/s10967-012-2009-2.

27. L. Ranjbar, A. T. Farsoni, and E. M. Becker, “A CZT-based radioxenon detection system in support of the Comprehensive Nuclear-Test-Ban Treaty,” Journal of Radioanalytical and Nuclear Chemistry, vol. 310, no. 3, pp. 969–978, Dec. 2016, doi: 10.1007/s10967-016-4872-8.

28. A. T. Farsoni, B. Alemayehu, A. Alhawsawi, and E. M. Becker, “A Phoswich Detector With Compton Suppression Capability for Radioxenon Measurements,” IEEE Transactions on Nuclear Science, vol. 60, no. 1, pp. 456–464, Feb. 2013, doi: 10.1109/TNS.2012.2226606.

29. S. A. Czyz, A. T. Farsoni, and L. Ranjbar, “A prototype detection system for atmospheric monitoring of xenon radioisotopes,” Nuclear Instruments and Methods in Physics Research Section A: Accelerators, Spectrometers, Detectors and Associated Equipment, vol. 884, pp. 64–69, Mar. 2018, doi: 10.1016/j.nima.2017.10.044.

30. S. A. Czyz and A. T. Farsoni, “A radioxenon detection system using CdZnTe, an array of SiPMs, and a plastic scintillator,” Journal of Radioanalytical and Nuclear Chemistry, vol. 313, no. 1, pp. 131–140, Jul. 2017, doi: 10.1007/s10967-017-5287-x.

31. S. A. Czyz et al., “A radioxenon detection system using PIPS and CZT,” Journal of Radioanalytical and Nuclear Chemistry, Dec. 2018, doi: 10.1007/s10967-018-6367-2.

32. H. R. Gadey, A. T. Farsoni, S. A. Czyz, and K. D. McGee, “A stilbene - CdZnTe based radioxenon detection system,” Journal of Environmental Radioactivity, vol. 204, pp. 117–124, Aug. 2019, doi: 10.1016/j.jenvrad.2019.03.027.

33. A. T. Farsoni and D. M. Hamby, “A system for simultaneous beta and gamma spectroscopy,” Nuclear Instruments and Methods in Physics Research Section A: Accelerators, Spectrometers, Detectors and Associated Equipment, vol. 578, no. 3, pp. 528–536, Aug. 2007, doi: 10.1016/j.nima.2007.06.020.

34. B. Alemayehu, A. T. Farsoni, L. Ranjbar, and E. M. Becker, “A well-type phoswich detector for nuclear explosion monitoring,” Journal of Radioanalytical and Nuclear Chemistry, vol. 301, no. 2, pp. 323–332, Aug. 2014, doi: 10.1007/s10967-014-3182-2.

35. E. Becker, M. Mannino, A. Farsoni, and C.-S. Lee, “Eight-Channel Digital Spectrometer for Coincidence Measurements in Multi-element Detectors,” p. 1, 2016.

36. S. A. Czyz, A. T. Farsoni, and H. R. Gadey, “Evaluation of a semiconductor-based atmospheric radioxenon detection system,” Nuclear Instruments and

Methods in Physics Research Section A: Accelerators, Spectrometers, Detectors and Associated Equipment, vol. 945, p. 162614, Nov. 2019, doi: 10.1016/j.nima.2019.162614.

37. H. R. Gadey, Abi T. Farsoni, and S. A. Czyz, “Preliminary results from a Stilbene-CdZnTe based Radioxenon Detection System,” 2018, doi: 10.13140/RG.2.2.12612.88963.

38. A. T. Farsoni, B. Alemayehu, A. Alhawsawi, and E. M. Becker, “Real-time pulse-shape discrimination and beta–gamma coincidence detection in field-programmable gate array,” Nuclear Instruments and Methods in Physics Research Section A: Accelerators, Spectrometers, Detectors and Associated Equipment, vol. 712, pp. 75–82, Jun. 2013, doi: 10.1016/j.nima.2013.02.003.

39. M. Mannino and D. E. Becker, “Real-Time Temporal Gamma Spectroscopy in a Field-Programmable Gate Array,” p. 22, 2017.

40. “J-SERIES SIPM: ON Semiconductor” [Online]. Available: https://www.onsemi.com/products/sensors/silicon-photomultipliers-sipm/j-series-sipm. [Accessed: 07/29/2020]

41. M. B. Kalinowski, “Characterisation of prompt and delayed atmospheric radioactivity releases from underground nuclear tests at Nevada as a function of release time,” Journal of Environmental Radioactivity, vol. 102, no. 9, pp. 824–836, Sep. 2011, doi: 10.1016/j.jenvrad.2011.05.006.

42. C. R. Carrigan and Y. Sun, “Detection of Noble Gas Radionuclides from an Underground Nuclear Explosion During a CTBT On-Site Inspection,” Pure and Applied Geophysics, vol. 171, no. 3–5, pp. 717–734, Mar. 2014, doi: 10.1007/s00024-012-0563-8.

43. M. B. Kalinowski and Y.-Y. Liao, “Isotopic Characterization of Radioiodine and Radioxenon in Releases from Underground Nuclear Explosions with Various Degrees of Fractionation,” Pure and Applied Geophysics, vol. 171, no. 3–5, pp. 677–692, Mar. 2014, doi: 10.1007/s00024-012-0580-7.

44. B. Bjurman et al., “The detection of radioactive material from a venting underground nuclear explosion,” Journal of Environmental Radioactivity, vol. 11, no. 1, pp. 1–14, Jan. 1990, doi: 10.1016/0265-931X(90)90040-3.

45. K. B. Olsen et al., “Noble gas migration experiment to support the detection of underground nuclear explosions,” J Radioanal Nucl Chem, vol. 307, no. 3, pp. 2603–2610, Mar. 2016, doi: 10.1007/s10967-015-4639-7.

46. P. Gaebler et al., “A multi-technology analysis of the 2017 North Korean nuclear test,” Solid Earth, vol. 10, no. 1, pp. 59–78, Jan. 2019, doi: 10.5194/se-10-59-2019.

47. A. Becker, G. Wotawa, A. Ringbom, and P. R. J. Saey, “Backtracking of Noble Gas Measurements Taken in the Aftermath of the Announced October 2006 Event in North Korea by Means of PTS Methods in Nuclear Source Estimation and Reconstruction,” Pure and Applied Geophysics, vol. 167, no. 4–5, pp. 581–599, May 2010, doi: 10.1007/s00024-009-0025-0.

48. C. M. Wright, “Low-Yield Nuclear Testing by North Korea in May 2010: Assessing the Evidence with Atmospheric Transport Models and Xenon Activity Calculations,” Science & Global Security, vol. 21, no. 1, pp. 3–52, Jan. 2013, doi: 10.1080/08929882.2013.754310.

49. A. Ringbom et al., “Measurements of radioxenon in ground level air in South Korea following the claimed nuclear test in North Korea on October 9, 2006,” Journal of Radioanalytical and Nuclear Chemistry, vol. 282, no. 3, pp. 773–779, Dec. 2009, doi: 10.1007/s10967-009-0271-8.

50. A. Ringbom et al., “Radioxenon detections in the CTBT international monitoring system likely related to the announced nuclear test in North Korea on February 12, 2013,” Journal of Environmental Radioactivity, vol. 128, pp. 47–63, Feb. 2014, doi: 10.1016/j.jenvrad.2013.10.027.

51. P. R. J. Saey et al., “A long-distance measurement of radioxenon in Yellowknife, Canada, in late October 2006,” Geophysical Research Letters, vol. 34, no. 20, Oct. 2007, doi: 10.1029/2007GL030611.

52. L. E. Sinclair et al., “Aerial measurement of radioxenon concentration off the west coast of Vancouver Island following the Fukushima reactor accident,” Journal of Environmental Radioactivity, vol. 102, no. 11, pp. 1018–1023, Nov. 2011, doi: 10.1016/j.jenvrad.2011.06.008.

53. B. Orr, M. Schöppner, R. Tinker, and W. Plastino, “Detection of radioxenon in Darwin, Australia following the Fukushima Dai-ichi nuclear power plant accident,” Journal of Environmental Radioactivity, vol. 126, pp. 40–44, Dec. 2013, doi: 10.1016/j.jenvrad.2013.07.002.

54. F. Xie et al., “Development of a radioxenon measurement system and its application in monitoring Fukushima nuclear accident,” Radiation Physics and Chemistry, vol. 97, pp. 85–89, Apr. 2014, doi: 10.1016/j.radphyschem.2013.11.011.

55. T. W. Bowyer et al., “Elevated radioxenon detected remotely following the Fukushima nuclear accident,” Journal of Environmental Radioactivity, vol. 102, no. 7, pp. 681–687, Jul. 2011, doi: 10.1016/j.jenvrad.2011.04.009.

56. W. Shilian et al., “Radioxenon monitoring in Beijing following the Fukushima Daiichi NPP accident,” Applied Radiation and Isotopes, vol. 81, pp. 344–347, Nov. 2013, doi: 10.1016/j.apradiso.2013.03.049.

57. P. W. Eslinger et al., “Source term estimation of radioxenon released from the Fukushima Dai-ichi nuclear reactors using measured air concentrations and atmospheric transport modeling,” Journal of Environmental Radioactivity, vol. 127, pp. 127–132, Jan. 2014, doi: 10.1016/j.jenvrad.2013.10.013.

58. A. Stohl, P. Seibert, and G. Wotawa, “The total release of xenon-133 from the Fukushima Dai-ichi nuclear power plant accident,” Journal of Environmental

Radioactivity, vol. 112, pp. 155–159, Oct. 2012, doi: 10.1016/j.jenvrad.2012.06.001.

59. “JAEA: Graph of Fission Product Yields” [Online]. Available: https://wwwndc.jaea.go.jp/cgi-bin/FPYfig. [Accessed: 09/14/2020]

60. “IAEA: C-3. Cumulative Fission Yields” [Online]. Available: https://www-nds.iaea.org/sgnucdat/c3.htm. [Accessed: 09/14/2020]

61. M. Schoeppner and A. Glaser, “Present and future potential of krypton-85 for the detection of clandestine reprocessing plants for treaty verification,” Journal of Environmental Radioactivity, vol. 162–163, pp. 300–309, Oct. 2016, doi: 10.1016/j.jenvrad.2016.06.001.

62. “CTBTO: Verification Science” [Online]. Available: https://www.ctbto.org/fileadmin/content/reference/outreach/spectrum_issues_singles/ctbto_spectrum_8/p22_23.pdf. [Accessed: 09/14/2020]

63. J. I. McIntyre et al., “Measurements of Argon-39 at the U20az underground nuclear explosion site,” Journal of Environmental Radioactivity, vol. 178–179, pp. 28–35, Nov. 2017, doi: 10.1016/j.jenvrad.2017.07.013.

64. “CTBTO: CONFERENCES TRAINING & WORKSHOPS” [Online]. Available: https://ctnw.ctbto.org/ctnw/abstract/32949. [Accessed: 09/14/2020]

65. “CTBTO: Verification Science” [Online]. Available: https://www.ctbto.org/fileadmin/content/reference/outreach/spectrum_issues_singles/ctbto_spectrum_8/p22_23.pdf. [Accessed: 09/14/2020]

66. C. E. Aalseth et al., “Measurement of 37Ar to support technology for On-Site Inspection under the Comprehensive Nuclear-Test-BanTreaty,” Nuclear Instruments and Methods in Physics Research Section A: Accelerators, Spectrometers, Detectors and Associated Equipment, vol. 652, no. 1, pp. 58–61, Oct. 2011, doi: 10.1016/j.nima.2010.09.135.

67. T. R. Alexander et al., “Characterization of a low background proportional counter for a high throughput Argon-37 collection and measurement system,” Nuclear Instruments and Methods in Physics Research Section A: Accelerators, Spectrometers, Detectors and Associated Equipment, vol. 954, p. 161794, Feb. 2020, doi: 10.1016/j.nima.2019.01.021.

68. P. L. Reeder and T. W. Bowyer, “Xe isotope detection and discrimination using beta spectroscopy with coincident gamma spectroscopy,” Nuclear Instruments and Methods in Physics Research Section A: Accelerators, Spectrometers, Detectors and Associated Equipment, vol. 408, no. 2–3, pp. 582–590, May 1998, doi: 10.1016/S0168-9002(98)00212-5.

69. G. Le Petit et al., “Contribution to the development of atmospheric radioxenon monitoring,” Journal of Radioanalytical and Nuclear Chemistry, vol. 276, no. 2, pp. 391–398, May 2008, doi: 10.1007/s10967-008-0517-x.

70. F. J. Klingberg, S. R. Biegalski, A. Prinke, D. A. Haas, and J. D. Lowrey, “Analysis of 125Xe electron–photon coincidence decay,” Journal of Radioanalytical and Nuclear Chemistry, vol. 307, no. 3, pp. 1933–1939, Mar. 2016, doi: 10.1007/s10967-015-4519-1.

71. F. J. Klingberg, S. R. Biegalski, D. Haas, and A. Prinke, “127Xe coincidence decay analysis in support of CTBT verification,” J Radioanal Nucl Chem, vol. 305, no. 1, pp. 225–232, Jul. 2015, doi: 10.1007/s10967-014-3871-x.

72. C. R. Carrigan, Y. Sun, and M. D. Simpson, “The characteristic release of noble gases from an underground nuclear explosion,” Journal of Environmental Radioactivity, vol. 196, pp. 91–97, Jan. 2019, doi: 10.1016/j.jenvrad.2018.10.015.

73. J. L. Burnett and A. V. Davies, “On-site inspection for the radionuclide observables of an underground nuclear explosion,” J Radioanal Nucl Chem, Nov. 2014, doi: 10.1007/s10967-014-3739-0.

74. “Hyperphysics.” [Online]. Available: http://hyperphysics.phy-astr.gsu.edu/hbase/quantum/xrayc.html. [Accessed: 02/21/2021]

75. K. S. Krane and D. Halliday, Introductory nuclear physics. New York: Wiley, 1987.

76. “Spectrum Techniques” [Online]. Available: http://www.spectrumtechniques.com/wp-content/uploads/2016/12/Cs-137-Decay-Scheme-500x291.jpg. [Accessed: 07/29/2020]

77. A. Cagniant et al., “SPALAX NG: A breakthrough in radioxenon field measurement,” Applied Radiation and Isotopes, vol. 134, pp. 461–465, Apr. 2018, doi: 10.1016/j.apradiso.2017.06.042.t/uploads/2016/12/Cs-137-Decay-Scheme-500x291.jpg

78. G. Le Petit et al., “Spalax™ new generation: A sensitive and selective noble gas system for nuclear explosion monitoring,” Applied Radiation and Isotopes, vol. 103, pp. 102–114, Sep. 2015, doi: 10.1016/j.apradiso.2015.05.019.

79. G. Le Petit et al., “Innovative concept for a major breakthrough in atmospheric radioactive xenon detection for nuclear explosion monitoring,” J Radioanal Nucl Chem, vol. 298, no. 2, pp. 1159–1169, Nov. 2013, doi: 10.1007/s10967-013-2525-8.

80. A. T. Farsoni, “Scintillation Detectors,” Oregon State University, 2016.

81. J. B. Birks, The theory and practice of scintillation counting. 1967.

82. F. D. Brooks, “Development of organic scintillators,” Nuclear Instruments and Methods, vol. 162, no. 1–3, pp. 477–505, Jun. 1979, doi: 10.1016/0029-554X(79)90729-8.

83. R. C. Sangster and J. W. Irvine, “Study of Organic Scintillators,” The Journal of Chemical Physics, vol. 24, no. 4, pp. 670–715, Apr. 1956, doi: 10.1063/1.1742595.

84. N. Zaitseva et al., “Scintillation properties of solution-grown trans-stilbene single crystals,” Nuclear Instruments and Methods in Physics Research Section A:

Accelerators, Spectrometers, Detectors and Associated Equipment, vol. 789, pp. 8–15, Jul. 2015, doi: 10.1016/j.nima.2015.03.090.

85. M. L. Ruch, M. Flaska, and S. A. Pozzi, “Pulse shape discrimination performance of stilbene coupled to low-noise silicon photomultipliers,” Nuclear Instruments and Methods in Physics Research Section A: Accelerators, Spectrometers, Detectors and Associated Equipment, vol. 793, pp. 1–5, Sep. 2015, doi: 10.1016/j.nima.2015.04.053.

86. M. J. Cieślak, K. A. A. Gamage, and R. Glover, “Pulse shape discrimination characteristics of stilbene crystal, pure and 6Li loaded plastic scintillators for a high resolution coded-aperture neutron imager,” J. Inst., vol. 12, no. 07, pp. P07023–P07023, Jul. 2017, doi: 10.1088/1748-0221/12/07/P07023.

87. J. A. Brown et al., “Relative light yield and temporal response of a stilbene-doped bibenzyl organic scintillator for neutron detection,” Journal of Applied Physics, vol. 115, no. 19, p. 193504, May 2014, doi: 10.1063/1.4878238.

88. C. Kim, J.-Y. Yeom, and G. Kim, “Digital n-γ Pulse Shape Discrimination in Organic Scintillators with a High-Speed Digitizer,” J Radiat Prot Res, vol. 44, no. 2, pp. 53–63, Jun. 2019, doi: 10.14407/jrpr.2019.44.2.53.

89. M. J. Weber, “Inorganic scintillators: today and tomorrow,” Journal of Luminescence, vol. 100, no. 1–4, pp. 35–45, Dec. 2002, doi: 10.1016/S0022-2313(02)00423-4.

90. C. W. E. van Eijk, “Development of inorganic scintillators,” Nuclear Instruments and Methods in Physics Research Section A: Accelerators, Spectrometers, Detectors and Associated Equipment, vol. 392, no. 1–3, pp. 285–290, Jun. 1997, doi: 10.1016/S0168-9002(97)00239-8.

91. S. E. Derenzo, M. J. Weber, E. Bourret-Courchesne, and M. K. Klintenberg, “The quest for the ideal inorganic scintillator,” Nuclear Instruments and Methods in Physics Research Section A: Accelerators, Spectrometers, Detectors and

Associated Equipment, vol. 505, no. 1–2, pp. 111–117, Jun. 2003, doi: 10.1016/S0168-9002(03)01031-3.

92. C. Dujardin et al., “Needs, Trends, and Advances in Inorganic Scintillators,” IEEE Trans. Nucl. Sci., vol. 65, no. 8, pp. 1977–1997, Aug. 2018, doi: 10.1109/TNS.2018.2840160.

93. G. F. Knoll, Radiation detection and measurement, 3rd ed. New York: Wiley, 2000.

94. “Edinburgh Instruments” [Online]. Available: https://www.edinst.com/blog/photoluminescence-differences/. [Accessed: 02/21/2021]

95. “Niels Bohr Institute: Scintillation detectors.” [Online]. Available: https://www.nbi.dk/~xella/lecture_16Feb2009.pdf. [Accessed: 02/21/2021]

96. D. P. Wells et al., “Photon Activation Analysis at the Idaho Accelerator Center,” Santiago (Chile), 2010, pp. 379–386, doi: 10.1063/1.3480205.

97. S. R. Cherry, J. A. Sorenson, and M. E. Phelps, Physics in nuclear medicine, 4th ed. Philadelphia: Elsevier/Saunders, 2012.

98. S. Aldawood et al., “Comparative Characterization Study of a LaBr3(Ce) Scintillation Crystal in Two Surface Wrapping Scenarios: Absorptive and Reflective,” Front. Oncol., vol. 5, Dec. 2015, doi: 10.3389/fonc.2015.00270.

99. “Saint-Gobain Crystals: $LaBr_3$.” [Online]. Available: https://www.crystals.saint-gobain.com/products/standard-and-enhanced-lanthanum-bromide. [Accessed: 02/21/2021]

100. “CapeSym: ScintiClear™ SiPM Detectors.” [Online]. Available: https://www.capesym.com/docs/SiPMdetect.pdf. [Accessed: 02/21/2021]

101. “Advatech: SrI2(Eu) - Strontium Iodide (Eu).” [Online]. Available: https://www.advatech-uk.co.uk/sri2_eu.html. [Accessed: 02/21/2021]

102. “Xtallized Intelligence: Enhanced CsI.”, Private Communication

103. “Berkeley Nucleonics Corp: Cerium Bromide.” [Online]. Available: https://www.berkeleynucleonics.com/cerium-bromide. [Accessed: 02/21/2021]

104. “Inrad Optics: Scintinel™ Stilbene.” [Online]. Available: https://www.inradoptics.com/scintinel-stilbene. [Accessed: 02/21/2021]

105. K. S. Shah et al., “CeBr/sub 3/ scintillators for gamma-ray spectroscopy,” in IEEE Symposium Conference Record Nuclear Science 2004., Rome, Italy, 2004, vol. 7, pp. 4278–4281, doi: 10.1109/NSSMIC.2004.1466835.

106. W. M. Higgins, A. Churilov, E. van Loef, J. Glodo, M. Squillante, and K. Shah, “Crystal growth of large diameter LaBr3:Ce and CeBr3,” Journal of Crystal Growth, vol. 310, no. 7–9, pp. 2085–2089, Apr. 2008, doi: 10.1016/j.jcrysgro.2007.12.041.

107. P. Guss, M. Reed, D. Yuan, A. Reed, and S. Mukhopadhyay, “CeBr3 as a room-temperature, high-resolution gamma-ray detector,” Nuclear Instruments and Methods in Physics Research Section A: Accelerators, Spectrometers, Detectors and Associated Equipment, vol. 608, no. 2, pp. 297–304, Sep. 2009, doi: 10.1016/j.nima.2009.06.096.

108. R. Billnert, S. Oberstedt, E. Andreotti, M. Hult, G. Marissens, and A. Oberstedt, “New information on the characteristics of 1in.×1in. cerium bromide scintillation detectors,” Nuclear Instruments and Methods in Physics Research Section A: Accelerators, Spectrometers, Detectors and Associated Equipment, vol. 647, no. 1, pp. 94–99, Aug. 2011, doi: 10.1016/j.nima.2011.05.034.

109. F. G. A. Quarati et al., “Scintillation and detection characteristics of high-sensitivity CeBr3 gamma-ray spectrometers,” Nuclear Instruments and Methods in Physics Research Section A: Accelerators, Spectrometers, Detectors and Associated Equipment, vol. 729, pp. 596–604, Nov. 2013, doi: 10.1016/j.nima.2013.08.005.

110. P. Kessler, B. Behnke, H. Dombrowski, and S. Neumaier, “Characterization of detector-systems based on CeBr 3 , LaBr 3 , SrI 2 and CdZnTe for the use as dosemeters,” Radiation Physics and Chemistry, vol. 140, pp. 309–313, Nov. 2017, doi: 10.1016/j.radphyschem.2016.12.015.

111. V. Peyres, T. Crespo, M. Mejuto, and E. García-Toraño, “Measurement of NORM samples with CeBr 3 detectors,” Applied Radiation and Isotopes, vol. 126, pp. 307–310, Aug. 2017, doi: 10.1016/j.apradiso.2017.02.012.

112. N. J. Cherepy et al., “Strontium and barium iodide high light yield scintillators,” Appl. Phys. Lett., vol. 92, no. 8, p. 083508, Feb. 2008, doi: 10.1063/1.2885728.

113. N. J. Cherepy et al., “Instrument Development and Gamma Spectroscopy With Strontium Iodide,” IEEE Trans. Nucl. Sci., vol. 60, no. 2, pp. 955–958, Apr. 2013, doi: 10.1109/TNS.2012.2227796.

114. N. Cherepy et al., “Prospects for High Energy Resolution Gamma Ray Spectroscopy with Europium-Doped Strontium Iodide,” MRS Proc., vol. 1164, pp. 1164-L11-04, 2009, doi: 10.1557/PROC-1164-L11-04.

115. E. V. van Loef et al., “Crystal Growth and Scintillation Properties of Strontium Iodide Scintillators,” IEEE Trans. Nucl. Sci., vol. 56, no. 3, pp. 869–872, Jun. 2009, doi: 10.1109/TNS.2009.2013947.

116. C. M. Wilson et al., “Strontium iodide scintillators for high energy resolution gamma ray spectroscopy,” San Diego, California, USA, Aug. 2008, p. 707917, doi: 10.1117/12.806291.

117. K. Shimazoe, A. Koyama, H. Takahashi, S. Sakuragi, and Y. Yamasaki, “Fabrication and characterization of cubic SrI2(Eu) scintillators for use in array detectors,” Nuclear Instruments and Methods in Physics Research Section A: Accelerators, Spectrometers, Detectors and Associated Equipment, vol. 810, pp. 59–62, Feb. 2016, doi: 10.1016/j.nima.2015.11.140.

118. K. Shimazoe, A. Koyama, H. Takahashi, S. Sakuragi, and Y. Yamasaki, "Fabrication and characterization of rectangular strontium iodide scintillator coupled to TSV-MPPC array," Nuclear Instruments and Methods in Physics Research Section A: Accelerators, Spectrometers, Detectors and Associated Equipment, vol. 845, pp. 503–506, Feb. 2017, doi: 10.1016/j.nima.2016.06.077.

119. M. S. Alekhin, J. T. M. de Haas, K. W. Kramer, and P. Dorenbos, "Scintillation Properties of and Self Absorption in SrI2:Eu2+," IEEE Trans. Nucl. Sci., vol. 58, no. 5, pp. 2519–2527, Oct. 2011, doi: 10.1109/TNS.2011.2163642.

120. R. S. Perea et al., "Scintillation properties of strontium iodide doped with europium for high-energy astrophysical detectors: nonproportionality as a function of temperature and at high gamma-ray energies," J. Astron. Telesc. Instrum. Syst, vol. 1, no. 1, p. 016002, Oct. 2014, doi: 10.1117/1.JATIS.1.1.016002.

121. "University of Zurich: Characterization of silicon photomultiplier arrays in liquid xenon and development of dedicated read-out electronics." [Online]. Available: https://www.physik.uzh.ch/groups/groupbaudis/darkmatter/theses/xenon/master_damato.pdf. [Accessed: 02/21/2021]

122. "KETEK: SiPM WORKING PRINCIPLE." [Online]. Available: https://www.ketek.net/sipm/technology/working-principle/. [Accessed: 02/21/2021]

123. "APPEC: The Silicon Photomultiplier (SiPM) Concept and Design Development." [Online]. Available: https://www.appec.org/news/the-silicon-photomultiplier-sipm-concept-and-design-development. [Accessed: 02/21/2021]

124. "Xilinx: Field Programmable Gate Array (FPGA)." [Online]. Available: https://www.xilinx.com/products/silicon-devices/fpga/what-is-an-fpga.html. [Accessed: 02/21/2021]

125. “Intel: Intel® FPGAs.” [Online]. Available: https://www.intel.com/content/www/us/en/products/programmable/fpga.html. [Accessed: 02/21/2021]

126. A. T. Farsoni, “Digital Filters in Radiation Detection and Spectroscopy,” Oregon State University, 2016

127. “Columbia University: THE DOE AUTOMATED RADIOXENON SAMPLER-ANALYZER (ARSA) BETA-GAMMA COINCIDENCE SPECTROMETER DATA ANALYZER.” [Online]. Available: https://www.ldeo.columbia.edu/res/pi/Monitoring/Doc/Srr_2000/6-Radionuclide/06_01.pdf. [Accessed: 02/21/2021]

128. L. A. Currie, “Limits for qualitative detection and quantitative determination. Application to radiochemistry,” Anal. Chem., vol. 40, no. 3, pp. 586–593, Mar. 1968, doi: 10.1021/ac60259a007.

129. J. I. McIntyre, T. W. Bowyer, and P. L. Reeder, “Calculation of Minimum-Detectable-Concentration Levels of Radioxenon Isotopes Using the PNNL ARSA System,” PNNL-13102, 888707, Mar. 2006. doi: 10.2172/888707.

130. “Cremat Inc: Charge sensitive preamplifiers explained.” [Online]. Available: https://www.cremat.com/why-use-csps/. [Accessed: 02/21/2021]

131. “ORTEC ®: Preamplifier Introduction.” [Online]. Available: https://www.ortec-online.com/-/media/ametekortec/other/preamplifier-introduction.pdf?la=en. [Accessed: 02/21/2021]

132. “Xilinx: KINTEX7.” [Online]. Available: https://www.xilinx.com/products/silicon-devices/fpga/kintex-7.html. [Accessed: 02/21/2021]

133. F. Cayouette, D. Laurendeau, and C. Moisan, “DETECT2000: an improved Monte-Carlo simulator for the computer aided design of photon sensing devices,” Quebec City, Canada, Feb. 2003, p. 69, doi: 10.1117/12.474315.

134. J. Allison et al., “Recent developments in Geant4,” Nuclear Instruments and Methods in Physics Research Section A: Accelerators, Spectrometers, Detectors and Associated Equipment, vol. 835, pp. 186–225, Nov. 2016, doi: 10.1016/j.nima.2016.06.125.

135. J. Allison et al., “Geant4 developments and applications,” IEEE Trans. Nucl. Sci., vol. 53, no. 1, pp. 270–278, Feb. 2006, doi: 10.1109/TNS.2006.869826.

136. S. Agostinelli et al., “Geant4—a simulation toolkit,” Nuclear Instruments and Methods in Physics Research Section A: Accelerators, Spectrometers, Detectors and Associated Equipment, vol. 506, no. 3, pp. 250–303, Jul. 2003, doi: 10.1016/S0168-9002(03)01368-8.

137. S. Incerti et al., “THE GEANT4-DNA PROJECT,” International Journal of Modeling, Simulation, and Scientific Computing, vol. 01, no. 02, pp. 157–178, Jun. 2010, doi: 10.1142/S1793962310000122.

138. J. Park and G. N. DeSouza, “3-D Modeling of Real-World Objects Using Range and Intensity Images,” in Machine Learning and Robot Perception, vol. 7, B. Apolloni, A. Ghosh, F. Alpaslan, L. C. Jain, and S. Patnaik, Eds. Berlin, Heidelberg: Springer Berlin Heidelberg, 2005, pp. 203–264.

139. T. W. Bowyer et al., “Automated separation and measurement of radioxenon for the Comprehensive Test Ban Treaty,” J Radioanal Nucl Chem, vol. 235, no. 1–2, pp. 77–82, Sep. 1998, doi: 10.1007/BF02385941.

140. C. E. Cox et al., “A 24-element Silicon PIN diode detector for high resolution radioxenon measurements using simultaneous X-ray and electron spectroscopy,” in 2013 IEEE Nuclear Science Symposium and Medical Imaging Conference (2013 NSS/MIC), Seoul, Korea (South), Oct. 2013, pp. 1–7, doi: 10.1109/NSSMIC.2013.6829481.

141. V. Thomas, O. Delaune, G. Le Petit, and J. P. Fontaine, “The Mobile Analyzer of Radioactive Gases OuTflows (MARGOT): A promising

environmental xenon radionuclides detection system," Applied Radiation and Isotopes, vol. 153, p. 108820, Nov. 2019, doi: 10.1016/j.apradiso.2019.108820.

142. V. Thomas, O. Delaune, A. Cagniant, G. Le Petit, and J.-P. Fontaine, "Introducing the MARGOT prototype: An ultra-compact and mobile gas detection system for nuclear explosion monitoring," Applied Radiation and Isotopes, vol. 152, pp. 91–100, Oct. 2019, doi: 10.1016/j.apradiso.2019.06.032.

143. M. W. Cooper et al., "Redesigned β–γ radioxenon detector," Nuclear Instruments and Methods in Physics Research Section A: Accelerators, Spectrometers, Detectors and Associated Equipment, vol. 579, no. 1, pp. 426–430, Aug. 2007, doi: 10.1016/j.nima.2007.04.092.

144. "Teledyne Brown Engineering: XENON INTERNATIONAL." [Online]. Available: https://tbe.com/energy/xenon-international. [Accessed: 02/21/2021]

145. L. Bläckberg et al., "Investigations of surface coatings to reduce memory effect in plastic scintillator detectors used for radioxenon detection," Nuclear Instruments and Methods in Physics Research Section A: Accelerators, Spectrometers, Detectors and Associated Equipment, vol. 656, no. 1, pp. 84–91, Nov. 2011, doi: 10.1016/j.nima.2011.07.038.

146. L. Bläckberg et al., "Memory effect, resolution, and efficiency measurements of an Al2O3 coated plastic scintillator used for radioxenon detection," Nuclear Instruments and Methods in Physics Research Section A: Accelerators, Spectrometers, Detectors and Associated Equipment, vol. 714, pp. 128–135, Jun. 2013, doi: 10.1016/j.nima.2013.02.045.

147. "CTBTO: CONFERENCES TRAINING & WORKSHOPS" [Online]. Available: https://ctnw.ctbto.org/ctnw/abstract/21838. [Accessed: 09/14/2020]

148. "CTBTO: CONFERENCES TRAINING & WORKSHOPS" [Online]. Available: https://ctnw.ctbto.org/ctnw/abstract/21821. [Accessed: 09/14/2020]

149. “Scienta Sensor Systems: SAUNA-III Datasheet.” [Online]. Available: https://www.sensorsystems.se/13/downloads. [Accessed: 02/21/2021]

150. “Scienta Sensor Systems: SAUNA-TXL Datasheet.” [Online]. Available: https://www.sensorsystems.se/13/downloads. [Accessed: 02/21/2021]

151. Yu. S. Popov, N. M. Kazarinov, V. Yu. Popov, Yu. M. Rykov, and N. V. Skirda, “Measuring Low Activities of Fission-Product Xenon Isotopes Using the β-γ Coincidence Method,” Instrum Exp Tech, vol. 48, no. 3, pp. 380–386, May 2005, doi: 10.1007/s10786-005-0066-2.

152. A. Cagniant, G. Le Petit, P. Gross, G. Douysset, H. Richard-Bressand, and J.-P. Fontaine, “Improvements of low-level radioxenon detection sensitivity by a state-of-the art coincidence setup,” Applied Radiation and Isotopes, vol. 87, pp. 48–52, May 2014, doi: 10.1016/j.apradiso.2013.11.078.

153. G. Le Petit, C. Jutier, P. Gross, and V. Greiner, “Low-level activity measurement of 131Xem, 133Xem, 135Xe and 133Xe in atmospheric air samples using high-resolution dual X–γ spectrometry,” Applied Radiation and Isotopes, vol. 64, no. 10–11, pp. 1307–1312, Oct. 2006, doi: 10.1016/j.apradiso.2006.02.094.

154. J. A. M. Lopes, R. E. Morgado, and C. A. N. Conde, “A metastable xenon isotope detector for treaty verification,” Nuclear Instruments and Methods in Physics Research Section A: Accelerators, Spectrometers, Detectors and Associated Equipment, vol. 501, no. 2–3, pp. 623–629, Apr. 2003, doi: 10.1016/S0168-9002(03)00621-1.

155. W. R. Schell, J. Vives-Batlle, S. R. Yoon, and M. J. Tobin, “High-pressure plastic scintillation detector for measuring radiogenic gases in flow systems,” Nuclear Instruments and Methods in Physics Research Section A: Accelerators, Spectrometers, Detectors and Associated Equipment, vol. 421, no. 3, pp. 591–600, Feb. 1999, doi: 10.1016/S0168-9002(98)01217-0.

156. F. Xie, W. Jiang, X. Li, X. He, J. Zhang, and G. Yu, “Single channel beta–gamma coincidence system for radioxenon measurement using well-type HPGe and plastic scintillator detectors,” Nuclear Instruments and Methods in Physics Research Section A: Accelerators, Spectrometers, Detectors and Associated Equipment, vol. 729, pp. 900–904, Nov. 2013, doi: 10.1016/j.nima.2013.08.070.

157. J. H. Ely, C. E. Aalseth, and J. I. McIntyre, “Novel beta-gamma coincidence measurements using phoswich detectors,” Journal of Radioanalytical and Nuclear Chemistry, vol. 263, no. 1, pp. 245–250, Jan. 2005, doi: 10.1007/s10967-005-0044-y.

158. W. Hennig et al., “Development of a phoswich detector system for radioxenon monitoring,” Journal of Radioanalytical and Nuclear Chemistry, vol. 282, no. 3, pp. 681–685, Dec. 2009, doi: 10.1007/s10967-009-0181-9.

159. W. Hennig et al., “Development of a phoswich detector system for radioxenon monitoring,” Journal of Radioanalytical and Nuclear Chemistry, vol. 282, no. 3, pp. 681–685, Dec. 2009, doi: 10.1007/s10967-009-0181-9.

160. V. Doost-Mohammadi, H. Afarideh, G. R. Etaati, M. J. Safari, and H. Rouhi, “INGAS: Iranian Noble Gas Analyzing System for radioxenon measurement,” Radiation Physics and Chemistry, vol. 120, pp. 26–32, Mar. 2016, doi: 10.1016/j.radphyschem.2015.10.020.

161. C. B. Sivels et al., “Stilbene cell development to improve radioxenon detection,” Nuclear Instruments and Methods in Physics Research Section A: Accelerators, Spectrometers, Detectors and Associated Equipment, vol. 923, pp. 72–78, Apr. 2019, doi: 10.1016/j.nima.2019.01.022.

162. “Oregon State University: Graduate Thesis Or Dissertation.” [Online]. Available: https://ir.library.oregonstate.edu/concern/graduate_thesis_or_dissertations/fn1075224?locale=en. [Accessed: 02/21/2021]

163. M. Janecek, “Reflectivity Spectra for Commonly Used Reflectors,” IEEE Trans. Nucl. Sci., vol. 59, no. 3, pp. 490–497, Jun. 2012, doi: 10.1109/TNS.2012.2183385.

164. “3M: 3M™ Enhanced Specular Reflector” [Online]. Available: https://www.3m.com/3M/en_US/company-us/all-3m-products/~/3M-Enhanced-Specular-Reflector-3M-ESR-/?N=5002385+3293061534&rt=rud. [Accessed: 09/14/2020]

165. A. Ulyanov et al., “Using the SIPHRA ASIC with an SiPM array and scintillators for gamma spectroscopy,” in 2017 IEEE Nuclear Science Symposium and Medical Imaging Conference (NSS/MIC), Atlanta, GA, Oct. 2017, pp. 1–3, doi: 10.1109/NSSMIC.2017.8532845.

166. A. Kryemadhi, L. Barner, A. Grove, J. Mohler, C. Sisson, and A. Roth, “Performance of LYSO and CeBr3 crystals readout by silicon photomultiplier arrays as compact detectors for space based applications,” J. Inst., vol. 12, no. 02, pp. C02013–C02013, Feb. 2017, doi: 10.1088/1748-0221/12/02/C02013.

167. A. Ulyanov et al., “Localisation of gamma-ray interaction points in thick monolithic CeBr 3 and LaBr 3 :Ce scintillators,” Nuclear Instruments and Methods in Physics Research Section A: Accelerators, Spectrometers, Detectors and Associated Equipment, vol. 844, pp. 81–89, Feb. 2017, doi: 10.1016/j.nima.2016.11.025.

168. “Analog Devices: LT8410/LT8410-1” [Online]. Available: https://www.analog.com/media/en/technical-documentation/data-sheets/84101fc.pdf. [Accessed: 09/14/2020]

169. “Opal Kelly: Featured Products” [Online]. Available: https://opalkelly.com/. [Accessed: 09/14/2020]

170. “MathWorks: Downloads” [Online]. Available: https://www.mathworks.com/downloads/web_downloads/download_release?release=R2014. [Accessed: 09/14/2020]

171. “Ultimaker: Ultimaker S3” [Online]. Available: https://ultimaker.com/3d-printers/ultimaker-s3. [Accessed: 09/14/2020]

172. “LANL: A General Monte Carlo N-Particle (MCNP) Transport Code” [Online]. Available: https://mcnp.lanl.gov/. [Accessed: 09/14/2020]

173. M. W. Cooper et al., “Absolute Efficiency Calibration of a Beta-Gamma Detector,” IEEE Trans. Nucl. Sci., vol. 60, no. 2, pp. 676–680, Apr. 2013, doi: 10.1109/TNS.2013.2243165.